Experimental study on turbulent pipe flow

by

Marco Ferro

September 2012
Technical Reports from
Royal Institute of Technology
KTH Mechanics
SE-100 44 Stockholm, Sweden

Marco Ferro 2012, **Experimental study on turbulent pipe flow**
Linné Flow Centre
KTH Mechanics
SE–100 44 Stockholm, Sweden

Abstract

abstract

Descriptors:

Contents

CHAPTER 1

Introduction

1.1. Instability and Turbulence

> *"Nota il moto del vello dell'acqua, il quale fa a uso de' capelli, che hanno due moti, de' quali l'uno attende al peso del vello, l'altro al liniamento delle sue volte; così l'acqua ha le sue volte revertiginose, delle quali una parte attende a l'impeto del corso principale, l'altra attende al moto incidente e refresso."*
>
> Leonardo da Vinci (1452 - 1519)

[Observe the motion of the surface of the water which resembles that of hairs, and has two motions, of which one goes on with the flow of the surface, the other forms the lines of the eddies; thus the water forms eddying whirlpools one part of which are due to the impetus of the principal current and the other to the incidental motion and return flow.] (English translation from: Richter 1883).

Leonardo wrote this phrase as a comment to his drawing in Figure 1.1, and what he describes there is the chaotic and swirling motion typical of turbulence, by far the most common flow regime in nature. In addition to the fascinating anatomical similarity, it seems possible to catch from this sentence a glimpse of the same idea of Reynolds decomposition.
A turbulent flow is a chaotic and unsteady motion with a high level of vorticity distributed along different sizes of eddies, characterized by a high diffusivity between fluid particles and by the dissipation of energy into heat. The first systematic work about turbulence was carried out by Reynolds (1883): observing the behaviour of a streak of coloured water inside pipes of different dimensions in which it was driven water at different velocities and temperatures, he noticed that when the parameter

$$\rho \frac{UD}{\mu} \tag{1.1}$$

FIGURE 1.1. Leonardo Da Vinci: *An Old Man Seated in Right Profile* and *Water studies* (ca. 1508-10). Windsor, Royal Library, 12579r, $(15.2 \times 21.3\,\mathrm{cm})$.

exceed a certain value, the flow became irregular (U and D are the characteristic velocity and dimension of the study case respectively, while ρ and μ are the fluid density and the dynamic viscosity). This dimensionless number was later named *Reynolds number* (Re) by Sommerfeld, and proved to be both the stability and the dynamic similarity parameter for viscous flows. When the transition to turbulence occurs, the main flow characteristics (symmetry or planarity for instance), are preserved just from the mean of the flow variables and not from their instantaneous values, suggesting the decomposition of the quantities in a mean and a fluctuating part. This was introduced by Reynolds (1895), who succeed in averaging the Navier-Stokes equations, obtaining what is now known as Reynolds Average Navier-Stokes equations (RANS). It was already stated that turbulence is characterized by the coexistence of several scales of eddies, but it was not emphasized that the eddies are related one to the other. Richardson (1922) realized that the large eddies extract kinetic energy from the flow and transfer it by an inviscid (i.e. conservative) process to smaller eddies, until the velocity gradient are high enough to let the viscosity dissipate this energy into heat. This idea of a *energy cascade* is at the heart of our present understanding of turbulent flows.

CHAPTER 2

Theoretical background

2.1. Statistical principles.

Although Navier-Stokes equations show a classical deterministic approach to the description of the fluid motion and can apply to laminar as well turbulent flows, turbulence is usually described as a *chaotic* or *random* process. Due to the enormous quantity of information included in the Navier-Stokes equation and the acute sensitivity that turbulent flow fields display to perturbations in the boundary conditions and in the initial values, turbulence does not only appear as chaotic but it is also more easily treated as a random process, i.e. using a statistical description.
In the following sections the main mathematical principles useful for the statistical analysis will be introduced, following mainly the text books by Pope (2000), Kundu & Cohen (2007) and Tropea *et al.* (2007).

2.1.1. *Distribution functions of random variables*

For a random variable $u = [u_1; u_2; u_3; ...]$ it is possible to define the *cumulative distribution function* (CDF) as

$$F(V) \equiv P\{u < V\} \,, \tag{2.1}$$

where $P\{A\}$ represents the probability of the event A to occur. From the definition it follows immediately that $F(-\infty) = 0$ and $F(+\infty) = 1$, and $F(V) > F(W)$ if $V > W$. From the CDF it is then possible to define the *probability density function* (PDF) as

$$f(V) \equiv \frac{\mathrm{d}F(V)}{\mathrm{d}V} \,. \tag{2.2}$$

The basic properties of the PDF, immediately following from the definition, are:

$$f(V) \geq 0 \tag{2.3}$$

and

$$\int_{-\infty}^{+\infty} f(V)\,\mathrm{d}V = 1\ . \tag{2.4}$$

The PDF, or equivalently the CDF, define completely a random variable, hence two or more random variables which have the same PDF, or CDF, are *statistically identical*.

2.1.2. *Statistical moments.*

The *mean* or first moment of a random variable u is defined as

$$U \equiv \langle u \rangle \equiv \int_{-\infty}^{+\infty} u f(u)\,\mathrm{d}u \tag{2.5}$$

From the definition of mean we can define the fluctuation u' as

$$u' \equiv u - U \tag{2.6}$$

and *variance* or second moment as the mean-square fluctuation, i.e.

$$\langle u'^2 \rangle \equiv \int_{-\infty}^{+\infty} (u-U)^2 f(u)\,\mathrm{d}u \tag{2.7}$$

The square-root of the variance is the *standard deviation* or *root mean square*, $u_{rms} = \sqrt{\langle u'^2 \rangle}$. The n^{th} central moment is defined to be

$$\langle u'^n \rangle \equiv \int_{-\infty}^{+\infty} (u-U)^n f(u)\,\mathrm{d}u\ . \tag{2.8}$$

Special interest have the third and fourth statistical moment, normalized with the proper power of the standard deviation, called respectively *skewness*

$$S \equiv \frac{\langle u'^3 \rangle}{u_{rms}^3} \tag{2.9}$$

and *flatness* or *kurtosis*

$$F \equiv \frac{\langle u'^4 \rangle}{u_{rms}^4}\ . \tag{2.10}$$

The skewness is a measure of the asymmetry of the PDF: it is equal to zero for a symmetric distribution, e.g. the Gaussian distribution, while it has a positive value if the PDF is shifted toward values greater than the mean and viceversa.

The flatness is instead a measure of the "peakedness" of the PDF and it is equal to 3 for a Gaussian distribution.

2.1.3. *Ensemble average and time average*

Statistics is based on *ensemble* averages, i.e. the set of samples is obtained from different realization of the experiment that we want to describe. For instance, if we want to characterize completely the velocity in one point in space and time $u(\vec{x_0}, t_0)$, we should repeat several experiments with the same boundary conditions and measure just one sample in the desired location at the same time from the experiment's start. What we usually do in practice is instead to measure the time series of the signal $u(\vec{x_0}, t)$ at the desired location during one single experiment. It can be proved that if the process is *statistically stationary*, i.e. if the statistics of the variable are constant in time, the ensemble average is equal to the time average (identified in the following with an overbar). E.g. , for the first moment we obtain:

$$\langle u(\vec{x}, t) \rangle = \overline{u(\vec{x}, t)} \,, \tag{2.11}$$

where

$$\overline{u(\vec{x}, t)} \equiv \frac{1}{T} \int_0^T u(\vec{x}, t) \, \mathrm{d}t \,. \tag{2.12}$$

A process with this characteristic is said to be ergodic. When dealing with non-stationary process, ergodicity is not fulfilled, but sometimes the average are still defined with eq. (2.12), choosing a sampling time T small compared to the time during which the average properties change significantly. To be more rigorous, we should observe that to describe completely the whole random process, i.e. the behaviour of the time-dependent random variable, we should acquire the complete time series of several experiments and obtain for each point in space $\vec{x}$ and for all possible choice of the set of times $\{t_1, t_2, ...t_n\}$ the n-time joint CDF defined by

$$\begin{aligned} F_n(\vec{x}, V_1, t_1; V_2, t_2; ...; V_n, t_n) \equiv P\{u(\vec{x}, t_1) < V_1 \wedge u(\vec{x}, t_2) < V_2 \\ \wedge u(\vec{x}, t_n) < V_n\} \end{aligned} \tag{2.13}$$

This means that in the case of a random process, the PDFs obtained from the ensembles of time-series at a specified point in time t, are not sufficient to describe completely the variable, because they do not contain any information about the correlation in time.
In this chapter we will consider always ensemble averages, but when in chapter 5 the results of the experiments will be shown, all the statistics will be based on time averages.

2.1.4. *Correlations*

The *autocovariance* of a the velocity field $u(\vec{x},t)$ is defined as:

$$R(\vec{x},t_1,t_2) \equiv \langle u'(\vec{x},t_1)u'(\vec{x},t_2)\rangle \ . \tag{2.14}$$

In a statistically stationary process all the statistics are independent of time shift, we can thus write $R(t_1,t_2) = R(t_1+T,t_2+T)$. It follows that the only important parameter for the determination of the autocovariance function is the time lag between t_1 and t_2. We can thus define the autocovariance function

$$R(\vec{x},\tau) \equiv \langle u'(\vec{x},t)u'(\vec{x},t+\tau)\rangle \ . \tag{2.15}$$

From the independence from a time shift it follows that the autocovariance is an even function

$$R(\vec{x},\tau) = \langle u'(\vec{x},t)u'(\vec{x},t+\tau)\rangle = \langle u'(\vec{x},t-\tau)u'(\vec{x},t)\rangle = R(-\tau) \ . \tag{2.16}$$

The autocovariance function is usually normalized with the variance of the signal, obtaining the *autocorrelation function*

$$\rho(\vec{x},\tau) \equiv \frac{\langle u'(\vec{x},t)u'(\vec{x},t+\tau)\rangle}{\langle u'^2(\vec{x})\rangle} \ . \tag{2.17}$$

From the definition it follows that

$$\rho(0) = 1 \ , \tag{2.18}$$

while

$$|\rho(\tau)| \leq 1 \tag{2.19}$$

for the Cauchy-Schwarz inequality. Figure 2.1 show the streamwise velocity autocorrelation function for current measurements of turbulent pipe flow in a near-wall location.
To investigate the spatial structures of a turbulent flow it is possible to define also the *spatial autocorrelation*

$$\rho_{uu}(\vec{x},\vec{r}) \equiv \frac{\langle u'(\vec{x},t)u'(\vec{x}+\vec{r},t)\rangle}{\langle u_{rms}(\vec{x})u_{rms}(\vec{x}+\vec{r})\rangle} \ . \tag{2.20}$$

The spatial autocorrelation it is said to be *longitudinal* if $\vec{r}$ is parallel to $\vec{u}$, while it is said to be *transverse* if it is perpendicular. In case of homogeneous turbulence, i.e. statistically invariant under translations of the reference frame,

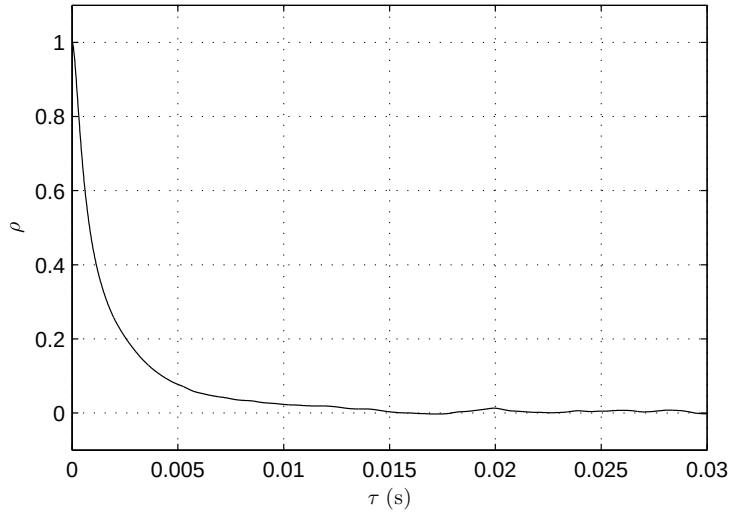

FIGURE 2.1. Autocorrelation function for current measurements of turbulent pipe flow. $Re = 34\,900$ and $r/R = 0.983$

the spatial autocorrelation is more simply

$$\rho_{uu}(\vec{r}) = \frac{\langle u'(\vec{x},t)u'(\vec{x}+\vec{r},t)\rangle}{\langle u'^2\rangle} \,. \tag{2.21}$$

2.1.5. *Power Spectral Density (PSD)*

In the analysis of a random variable we might be interested in how the power of the signal u'^2 is distributed in the frequency space. Since the Fourier transform of u'^2 does not converge, we define the power spectral density as

$$S_{uu}(f) = \lim_{T\to\infty} \langle |\mathcal{F}(f,T)|^2 \rangle \,, \tag{2.22}$$

where

$$\mathcal{F}(f,T) = \frac{1}{\sqrt{T}} \int_0^T u'(t) e^{-i2\pi f t} \,\mathrm{d}t \tag{2.23}$$

is the truncated Fourier transform of the velocity fluctuation. Moreover it holds the *Wiener-Khinchin theorem*, which states that the power spectral density of

a statistically stationary random process is the Fourier transform of the corresponding autocovariance function:

$$S_{uu}(f) = \lim_{T\to\infty} \langle |\mathcal{F}(f,T)|^2 \rangle = \int_{-\infty}^{+\infty} R(\tau) e^{-i2\pi f\tau} \, \mathrm{d}\tau \, . \tag{2.24}$$

It follows

$$R(\tau) = \int_{-\infty}^{+\infty} S_{uu}(f) e^{i2\pi f\tau} \, \mathrm{d}f \, . \tag{2.25}$$

Since $u'(t)$ and $R(\tau)$ are real-valued functions, their Fourier transform is an even function. In the following it will be considered just one-sided PSD P_{uu}, defined as

$$P_{uu}(f) = \begin{cases} 2S_{uu}(f) & 0 \le f < +\infty \\ 0 & \text{otherwise} \, . \end{cases} \tag{2.26}$$

For $\tau = 0$ eq. (2.25) and (2.26) give

$$R(0) = \langle u'^2 \rangle = \int_{0}^{+\infty} P_{uu}(f) \, \mathrm{d}f \, , \tag{2.27}$$

which relates the velocity variance to the power spectral density.

2.1.5a. *Spectral estimate from finite time records.* A real measurement is of course finite in time, it is then necessary to have a reliable method to estimate the power spectral density from the finite-length time series. For the current experiments *Welch's method* (Welch 1967) has been used. It consists in dividing the time series in sections of desired length, each with 50% overlap, and calculate the power spectral density of $u(t)w(t)$, where $w(t)$ is a window function chosen to mitigate the spectral leakage (e.g. the Hamming window function). The individual power spectral density estimates are then averaged, obtaining a better estimate of the power spectral density of the time series. Splitting the time series in several sections decreases the frequency resolution of the power spectral density estimate, but increases its accuracy. Figure 2.2 illustrates the power spectral density estimate obtained with Welch's method of the streamwise velocity fluctuations for current measurements in turbulent pipe flow. It is common to illustrate the power spectral density in premultiplied form in a semi-logarithmic plot, as shown in Figure 2.3, because as will be explained in §5.6, the area under the premultiplied power spectra is directly related to the streamwise velocity variance.

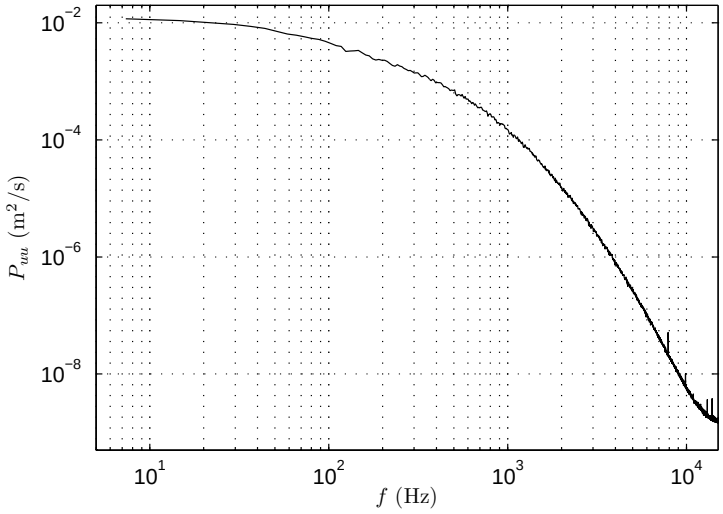

FIGURE 2.2. Power Spectral Density estimate of streamwise velocity fluctuation in turbulent pipe flow obtained from current measurements with the Welch's method. $Re = 34\,900$ and $r/R = 0.983$

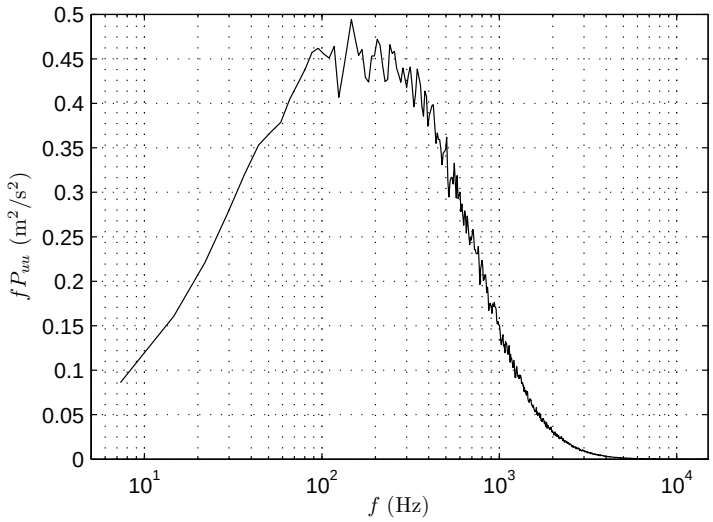

FIGURE 2.3. Premultiplied Power Spectral Density estimate for same case of Fig. 2.2

2.1.6. *Length and time scales of turbulent flows*

In fluid mechanics the concept of similarity is of extreme importance in the description and analysis of flows. Moreover, due to the complex nature of turbulence most of the results are based on scaling law and dimensional arguments; it is thus important to define the length, velocity and time scales of the turbulence processes.
The most obvious scales are the ones related to the macroscopic characteristic of the flow, e.g. a characteristic length scale for a plate is the boundary layer thickness or for a pipe is its radius. In the following with the notation *outer scaling* it will be meant the use of R as length scale, the bulk velocity U_b as velocity scale and R/U_b as time scale (turnover time).
In a fundamental work Kolmogorov (1941) proposed that at sufficiently high Reynolds number, the small-scales turbulent motions are statistically isotropic and have a universal form that is uniquely determined by the dynamic viscosity ν and the turbulent dissipation ε (i.e. the rate at which energy is dissipated into heat by viscosity). On dimensional argument Kolmogorov derived the scales of the turbulent eddies as

$$\eta \equiv \left(\frac{\nu^3}{\varepsilon}\right)^{1/4} , \tag{2.28}$$

$$t_\eta \equiv \left(\frac{\nu}{\varepsilon}\right)^{1/2} , \tag{2.29}$$

$$u_\eta \equiv (\varepsilon\nu)^{1/4} , \tag{2.30}$$

that are now known as Kolmogorov's length scale, time scale and velocity scale. From these definitions it follows the identity

$$Re_\eta = \frac{\eta u_\eta}{\nu} = 1 , \tag{2.31}$$

which evidence that the Kolmogorov scales effectively characterize the dissipative eddies in which the viscous forces dominate.
From the autocorrelation functions defined in eq. (2.17), we can define the *integral time scale* as

$$\Lambda_t = \int_0^{+\infty} \rho(\tau)\, \mathrm{d}\tau , \tag{2.32}$$

which can be seen as the time scale over which the signal retains some significant correlation with itself. From the autocorrelation function also the Taylor microscale (Taylor 1935) can be defined as

$$\lambda_t = \left[-\frac{1}{2}\rho''(\tau)\right]^{-1/2} . \tag{2.33}$$

Considering the Taylor expansion of $\rho(\tau)$ around $\tau = 0$, we can prove that the Taylor microscale is the value of τ where the osculating parabola of $\rho(\tau)$ intercepts the τ axis. Giving a physical interpretation of the Taylor microscale is not straightforward, but we can consider it as the scale over which the signal is strongly correlated. In complete analogy with the integral and Taylor time scales, the longitudinal or transverse integral and Taylor length scales are defined from the spatial autocorrelation function (eq. 2.20).

2.2. Turbulent pipe flow

2.2.1. *Governing equations and wall shear stress*

To analyse the turbulent pipe flow is convenient to use to define a cylindrical reference frame, with the axial coordinate x aligned with the mean streamwise direction of the flow, the radial direction r, normal to the pipe wall and originating in the centre of the pipe and with θ as the angular coordinate. The velocity component are respectively u, v and w. In the following we will indicate with R the pipe radius. The pipe flow is statistically axisymmetrical, for such flows it holds

$$W = \langle uw \rangle = \langle vw \rangle = \frac{\partial}{\partial \theta} = 0 \tag{2.34}$$

and the RANS equation in cylindrical coordinates reduce to

$$\frac{\partial U}{\partial x} + \frac{1}{r}\frac{\partial}{\partial r}(rV) = 0 \tag{2.35}$$

$$\frac{\partial U}{\partial t} + U\frac{\partial U}{\partial x} + V\frac{\partial U}{\partial r} = -\frac{1}{\rho}\frac{\partial P}{\partial x} - \frac{\partial}{\partial x}\langle u'^2 \rangle - \frac{1}{r}\frac{\partial}{\partial r}(r\langle uv \rangle) + \nu\nabla^2 U \tag{2.36}$$

$$\begin{aligned}\frac{\partial V}{\partial t} + U\frac{\partial V}{\partial x} + V\frac{\partial V}{\partial r} = &-\frac{1}{\rho}\frac{\partial P}{\partial r} - \frac{\partial}{\partial x}\langle u'v' \rangle - \frac{1}{r}\frac{\partial}{\partial r}(r\langle v'^2 \rangle) + \\ &+ \frac{\langle w'^2 \rangle}{r} + \nu\left(\nabla^2 V - \frac{V}{r^2}\right)\end{aligned} \tag{2.37}$$

where

$$\nabla^2 f = \frac{\partial^2 f}{\partial x^2} + \frac{1}{r}\frac{\partial}{\partial r}(r\frac{\partial f}{\partial r}) + \frac{1}{r^2}\frac{\partial^2 f}{\partial \theta^2} \tag{2.38}$$

We will focus the attention of this study on statistically stationary pipe flow in

the *fully developed* region, in which the flow is satistically independent on the axial direction x. We hence have:

$$\frac{\partial}{\partial t} = 0 \tag{2.39}$$

$$\frac{\partial U}{\partial x} = \frac{\partial \langle u'^2 \rangle}{\partial x} = \frac{\partial \langle v'^2 \rangle}{\partial x} = 0 \tag{2.40}$$

From the continuity equation (eq. 2.35), the hypothesis of fully developed flow (eq. 2.40) and the boundary conditions $V|_w = V_{cl} = 0$ (where the subscripts w and cl represents the wall and centerline position respectively), we obtain

$$V = 0 \, . \tag{2.41}$$

Substituting eq. (2.39), (2.40) and (2.41) in the r-moment equation (eq. 2.37) we obtain

$$\frac{1}{\rho}\frac{\partial P}{\partial r} + \frac{\partial}{\partial r}\langle v'^2 \rangle = \frac{\langle w'^2 \rangle}{r} - \frac{\langle v'^2 \rangle}{r} \, , \tag{2.42}$$

which integrated between the generic radial coordinate r and the pipe radius R gives

$$\frac{1}{\rho}(P_w - P) - \langle v'^2 \rangle = \int_r^R \frac{\langle w'^2 \rangle}{r} - \frac{\langle v'^2 \rangle}{r} \, \mathrm{d}r \, . \tag{2.43}$$

Taking the derivative of eq. (2.43) along the x direction and applying the fully developed flow hypothesis we obtain

$$\frac{\partial P}{\partial x} = \frac{\mathrm{d}P_w}{\mathrm{d}x} \, , \tag{2.44}$$

which states that the mean axial pressure gradient is uniform along the pipe radius. Substituting eq. (2.39), (2.40), (2.41) and (2.44) in the x-momentum equation (eq. 2.36) we have

$$\frac{1}{\rho}\frac{\mathrm{d}P_w}{\mathrm{d}x} = -\frac{1}{r}\frac{\mathrm{d}}{\mathrm{d}r}(r\langle u'v' \rangle) + \frac{\nu}{r}\frac{\mathrm{d}}{\mathrm{d}r}\left(r\frac{\mathrm{d}U}{\mathrm{d}r}\right) \, . \tag{2.45}$$

Considering that the total shear stress $\tau(r)$ is

$$\tau = \mu\frac{\mathrm{d}U}{\mathrm{d}r} - \rho\langle u'v' \rangle \, , \tag{2.46}$$

eq. (2.45) can be written as

$$\frac{\mathrm{d}P_w}{\mathrm{d}x} = \frac{1}{r}\frac{\mathrm{d}}{\mathrm{d}r}(r\tau) \,. \tag{2.47}$$

Integrating eq. (2.47) from the pipe centerline to the pipe radius gives

$$\tau(R) = \frac{R}{2}\frac{\mathrm{d}P_w}{\mathrm{d}x} \tag{2.48}$$

which relates the pressure drop with the shear stress. Integrating eq. (2.47) from the generic radial coordinate r to the pipe radius and making use of eq. (2.48) we obtain

$$\tau(r) = \frac{r}{2}\frac{\mathrm{d}P_w}{\mathrm{d}x} \,, \tag{2.49}$$

which is usually rewritten as

$$\tau = -\tau_w\left(1 - \frac{y}{R}\right) \,, \tag{2.50}$$

where $\tau_w = -\tau(R)$ is the shear stress *on* the wall and $y = R - r$ is the wall-normal distance. Profiles of Reynolds and viscous shear stress are shown in Figure 2.4, from which is apparent that viscous stresses dominates at the wall, while viscous stresses dominates in the outer part.
The shear stress in pipe flow is traditionally expressed in terms of friction factor

$$f \equiv -\frac{\mathrm{d}P}{\mathrm{d}x}\frac{D}{\frac{1}{2}\rho U_b^2} \,, \tag{2.51}$$

where U_b is the bulk velocity in the pipe. From eq. (2.51) and (2.48) we obtain

$$f = 8\frac{\tau_w}{\rho U_b^2} \,. \tag{2.52}$$

In an influential set of experiments Nikuradse (1933) measured the friction factor in smooth pipes and for pipes with varying amount of roughness. For fully developed laminar flow it is possible to obtain the analytical relation

$$f = \frac{64}{Re} \,, \tag{2.53}$$

while for turbulent regime Prandtl proposed for smooth pipes the implicit equation

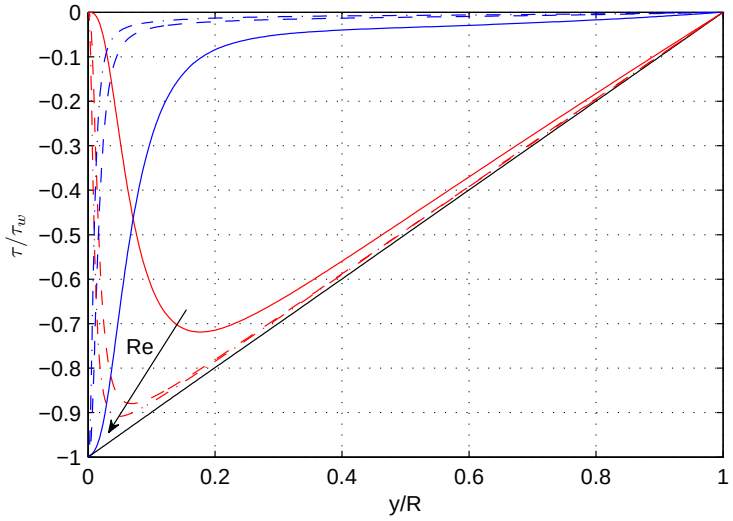

FIGURE 2.4. Reynolds stresses $-\rho\langle' u' v'\rangle$ (*red*) and viscous stresses $\mu\frac{\partial U}{\partial r}$ (*blue*) normalized with the wall shear stress vs. the normalized wall distance. *Solid*, *dashed* and *dash-dotted* lines represents Re = 5 000, Re = 24 000 and Re = 44 000 respectively, *black solid* line is the total shear stress. Data from DNS by Wu & Moin (2008).

$$\frac{1}{\sqrt{f}} = 2.0\log_{10}(\sqrt{f}Re) - 0.8\,. \tag{2.54}$$

A more general relation which consider also the wall-roughness was proposed by Colebrook (1939):

$$\frac{1}{\sqrt{f}} = -2\log_{10}\left(\frac{1}{3.7}\frac{e}{D} + \frac{2.51}{\sqrt{f}Re}\right)\,, \tag{2.55}$$

where e/D is the roughness height normalized with the pipe diameter. *Moody's chart* (Moody 1944), shown in Figure 2.5, represents all the aforementioned relations and is thus of common use in engineering.

2.2.2. *Viscous scales and mean velocity profile*

Close to the wall the main parameters in the description of the flow are the wall shear stress τ_w and the cinematic viscosity $\nu = \mu/\rho$, we thus expect the flow to scale on properly defined normalization parameters (*viscous scales*) based on those quantity. We define the *friction velocity*

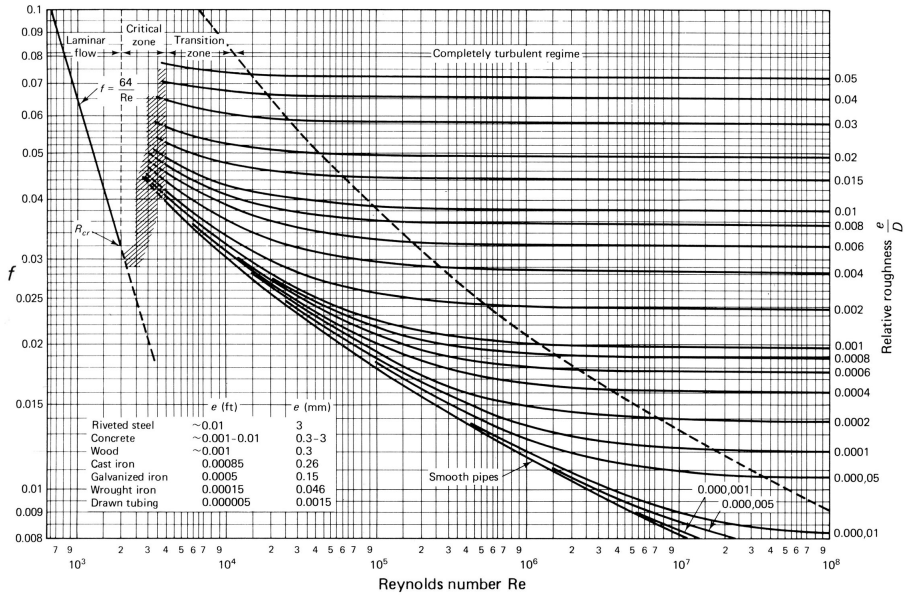

FIGURE 2.5. Moody's diagram depicting the friction factor in function of Reynolds number.

$$u_\tau \equiv \sqrt{\frac{\tau_w}{\rho}} \tag{2.56}$$

and the *viscous length scale*

$$\ell_* \equiv \frac{\nu}{u_\tau} \, . \tag{2.57}$$

From those two quantities it follows the *viscous timescale*

$$t_* = \frac{l_*}{u_\tau} = \frac{\nu}{u_\tau} \, . \tag{2.58}$$

A *friction Reynolds number* is also defined as

$$Re_\tau = R^+ = \frac{R}{\ell_*} \, , \tag{2.59}$$

i.e. the ratio of the outer and viscous length scales. In the following the superscript $^+$ will mean a quantity normalized with the viscous scales. In particular we define the viscous scaled velocity

$$U^+ \equiv \frac{U}{u_\tau} \tag{2.60}$$

and the viscous scaled wall distance or *wall units* denoted by

$$y^+ \equiv \frac{y}{l_*} = \frac{u_\tau y}{\nu} \,, \tag{2.61}$$

which resemble a local Reynolds number and its magnitude can be interpreted as the relative importance of the turbulent and viscous process.
In a fundamental work Prandtl (1925) postulated that at high Reynolds number exist close to the wall a region in which the normalized velocity is function just of the normalized wall distance, i.e.

$$U^+ = \Phi(y^+) \,. \tag{2.62}$$

This region is called *inner layer* and is usually defined as $y^+ < 0.1R^+$. The expression in eq. (2.62) is called *law of the wall*, and in the classical theory and textbooks is presented as universal for all wall-bounded flows on smooth surfaces. Extremely close to the wall ($y^+ < 5$) we identify a *viscous sublayer*, where Reynolds stress are negligible and in consequence to the choice of the normalization, a Taylor expansion of Φ around $y^+ = 0$ gives

$$U^+ = y^+ + o(y^+) \,. \tag{2.63}$$

For zero pressure-gradient flow the next non-zero term of the expansion is of order $(y^+)^4$, while in presence of pressure gradient the second order term exist and is inversely proportional to R^+ (see §4.3), hence for $R^+ \to \infty$ the similarity between the different flow cases can be considered valid in this region. Further from the wall, the viscous stresses become small compared to the turbulent stresses, we thus expect that in the *outer layer*, commonly defined as $y^+ > 50$, the velocity field for $R^+ \to +\infty$ is independent of ν and is function of y/R only. In this region it holds the *velocity-defect* law, proposed by von Kármán (1930)

$$\frac{U_{cl} - U}{u_\tau} = \Psi(\frac{y}{R}) \,. \tag{2.64}$$

Von Kármán proposed a logarithmic behaviour of Ψ based on Prandtl's mixing length hypothesis. Even with a different notation and normalization he has found what now is known as the *log-law*

$$U^+ = \frac{1}{\kappa} \ln y^+ B \,, \tag{2.65}$$

where κ and B are constant (κ is called the von Kármán constant). The logarithmic description is expected to hold in a portion of the *overlap region*, i.e. where the inner and outer layer overlap. Another possible derivation of the log-law was proposed by Millikan (1938), matching the derivatives of the formulation in eq. (2.62) and (2.64).
The region of validity of the log-law is an open issue and in literature different values for its bounds has been proposed: the lower ones is especially debated, with values spanning more than one order of magnitude from $y^+ > 30$ (Pope 2000, among others) $y^+ > 200$ (Nagib *et al.* 2007; Österlund *et al.* 2000) or $y^+ > 600$ (McKeon *et al.* 2004). More accordance is found on the higher bound, with almost all the authors proposing $y/\delta < 0.1 - 0.2$. The values of the log-law constants is another debated problem, related also to the choice of the bounds, and their universality has been objected. The issue is fairly complicated and is out of the purpose of this report, also because, as will be pointed out in §4.4, the absence of a direct measure of τ_w in the current experimental apparatus does not allow the use of the collected data for the determination of the log-law constants. For a pleasant review on the subject the reader is referred to (Örlü 2009, §3.2-3.5).
Before the conclusion it is necessary to define the *buffer layer* as the region between the end of the viscous sublayer and the beginning of the log-law region, where neither the viscous stress nor the turbulent stress are negligible.

As we have seen the linear or logarithmic profile are valid just in limited portion of the profile. To overcome this limitation several composite profiles has been proposed. One of the first description was given by Coles (1956) for the boundary layer and is based on the idea that the velocity profile can be represented by the superposition of the law of the wall and an additive function representing the outer part of the profile

$$U^+ = U^+_{\text{inner}}(y^+) + \frac{2\Pi}{\kappa}\mathcal{W}\left(\frac{y^+}{R^+}\right), \tag{2.66}$$

where Π and $\mathcal{W}$ are known as wake parameter and wake function respectively. Nagib & Chauhan (2008) proposed a composite profile of the kind of eq. (2.66). For the inner region they modified the Musker (1979) profile, which agrees with the linear law of the wall close to the wall and develops into the logarithmic profile at higher y^+. The main shortcomings of the Musker profile are that, since it was developed for boundary layer flow, it does not take into consideration the second order term in the Taylor expansion of U^+ at the wall (which is zero in absence of pressure gradient) and it fails to reproduce an "overshoot" above the logarithmic profile that DNS data show for $y^+ \approx 50$. Both the effects are taken into consideration in the modified version by Nagib & Chauhan (2008), who proposed

$$
\begin{aligned}
U^+_{\text{inner}} = & \frac{1}{\kappa}\ln\left(\frac{y^+ - a}{-a}\right) + \frac{R^2}{a(4\alpha - a)}\left\{(4\alpha + a)\ln\left(-\frac{a}{R}\frac{\sqrt{(y^+ - \alpha)^2 + \beta^2}}{y^+ - a}\right) + \right. \\
& \left. + \frac{\alpha}{\beta}(4\alpha + 5a)\left[\arctan\left(\frac{y^+ - \alpha}{\beta}\right) + \arctan\left(\frac{\alpha}{\beta}\right)\right]\right\} + \\
& + \frac{1}{aR^2R^+}\left[\frac{a}{(a-\alpha)^2 + \beta^2}\ln\left(\frac{y^+ - a}{\sqrt{(y^+ - \alpha)^2 + \beta^2}}\right) + \right. \\
& \left. + \left(1 + \frac{a - \alpha}{\beta[(a-\alpha)^2 + \beta^2]}\right)\arctan\left(\frac{y^+ - \alpha}{\beta}\right)\right] + \frac{1}{2.47}\exp\left[-\frac{\ln^2(y^+/30)}{0.835}\right],
\end{aligned}
\tag{2.67}
$$

where

$$
\alpha = -\frac{1}{2(\kappa - a)}\,, \quad \beta = \sqrt{(-2a\alpha - \alpha^2)}\,, \quad R = \sqrt{\alpha^2 + \beta^2}\,, \quad s = -aR^2\,.
$$

For the outer part of the profile, they proposed an empirical fitting with an exponential function. As already stated, in this region the description must be flow dependent because the effects of geometry are important. For pipe flow they obtained

$$
\mathcal{W}_{\text{pipe}} = \left(1 - \frac{\ln(\eta)}{2\Pi}\right)\frac{1 - \exp\{\eta^3\left[p_2(\eta - \frac{4}{3}) + p_3(\eta^3 - 2) + p_4(\eta^4 - \frac{7}{3})\right]\}}{1 - \exp\left[-(p_2 + 3p_3 + 4p_4)/3\right]} \tag{2.68}
$$

with $\eta = y/R$, $p_2 = 4.075$, $p_3 = -6.911$ and $p_4 = 4.876$ and wake parameter $\Pi = 0.21$.

CHAPTER 3

Experimental Setup

3.1. Experimental apparatus

3.1.1. *Rotating pipe flow facility*

The turbulent pipe flow measurements were performed in the rotating pipe apparatus located at the *Fluid Physics Laboratory* of the *Linné Flow centre* at *KTH Mechanics*. The facility was designed, built and taken into operation in connection to the work of Facciolo (2006), then slightly modified in order to be used also for the works by Örlü (2009) and Sattarzadeh (2011). The schematic of the facility is shown in Figure 3.1. Air at ambient temperature and pressure is provided to a centrifugal fan (B), after going through a throttle valve (A) for flow rate control. Since the regulation range provided by this valve was not wide enough, a bypass (C) regulated by another throttle valve is inserted after the fan. A distribution chamber (E) is mounted after the fan in order to reduce the transmission of vibration. An electrical heater (D) for eventually heating the air stream lies inside the distribution chamber. The flow is then distributed in three different spiral pipes that fed axisimmetrically the air into a cylindrical stagnation chamber (G) with one end covered with an elastic membrane, in order to further reduce the pressure fluctuations. Once in the stagnation chamber the air first go through a honeycomb (F) to reduce lateral velocity component and then is fed into a 1 m long stationary pipe through a bell mouth shaped entrance, to provide an axisimmetrical flow. This first pipe is connected to the six meter long axially rotating pipe (L) through a sealed rotating coupling (H). In the first section of the rotating pipe a 12 cm long honeycomb is mounted, made of 5 mm diameter drinking straws, which, if the pipe is swirling, brings the flow into a more or less solid body rotation. The rotating pipe is made of seamless steel, has a wall thickness of 5 mm and an inner diameter of 60 mm. The inner surface is honed and the surface roughness is less than 5 µm, according to the manufacturer's specifications. The pipe is mounted inside a rigid triangular shaped framework with five ball bearing supports (K). The rotation is obtained via a feedback controlled DC motor (J) capable to run the pipe to rotational speeds up to 2000 rpm. Anyway, for the present experimental investigation only fully developed non-swirling turbulent pipe flow has been investigated. The air stream is ejected at 1.1 m

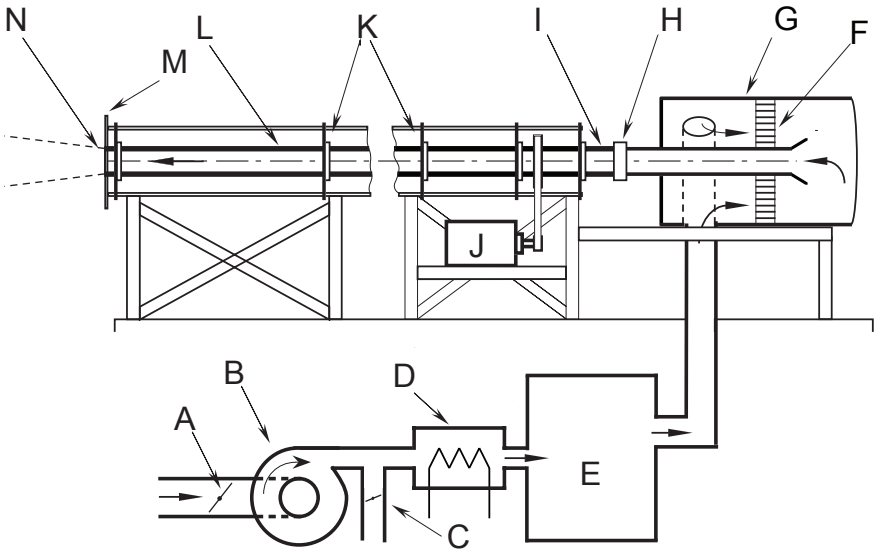

FIGURE 3.1. Schematic of the rotating pipe facility. A) Throttle valve, B) Centrifugal fan, C) Valve regulated bypass, D) Electrical heater, E) Distribution chamber, F) Honeycomb, G) Stagnation chamber, H) Coupling between stationary and rotating pipe, I) Honeycomb J) DC motor, K) Ball bearings, L) Rotating pipe, M) Circular and plate, N) Pipe outlet

from the floor as a free jet (N) into the ambient air at rest. By placing the apparatus in a large laboratory with a large ventilation opening more than 60 pipe diameters downstream of the pipe outlet it is ensured that the jet can develop far away from any physical boundaries. At the pipe outlet it is possible to mount a circular end plate of different size (M), to reduce the entrainment at the pipe outlet for jet flow studies, but during the current measurements none was mounted. The L/D ratio equal to 100 ensures the fully developed turbulent flow condition both for swirling and non-swirling case: this was experimentally proven for this apparatus by Facciolo (see Facciolo 2006, §5.1). Moreover, a recent work from Doherty *et al.* (2007) showed that to obtain higher order statistics (up to flatness) invariance a $L/D = 80$ was required. For the present work a new and more powerful centrifugal fan has been installed in order to extend the maximum Reynolds number (based on bulk velocity) up to 110 000, while in the previous studies it was limited to 30 000. The use of this bigger fan has also the effect to heat the flow up to 12 K above room temperature; to have a stable condition during the measurements, it is then necessary to wait until the equilibrium condition is reached. Figure 3.2 shows the velocity and temperature

evolution during the starting up of the fan at the centerline position. For the profile measurements performed in the present investigation the measurements took between 45 min and 90 min depending on the Re number, i.e. the higher the Re the shorter the total sampling time, due to the shorter integral time scale. During this time the velocity and temperature at the pipe exit can safely be assumed to be steady, if one wait long enough (about one hour) before starting the measurements. As a double check the data were acquired twice in some positions, one time at the beginning of the profile measurement and another time at its end, to ensure that the results were consistent.

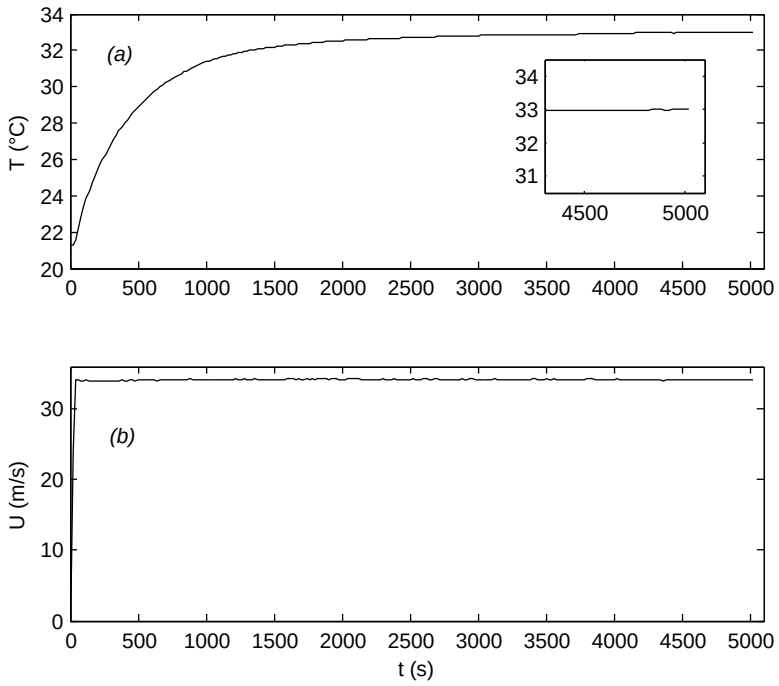

FIGURE 3.2. Centerline temperature *(a)* and velocity *(b)* evolution during the starting up of the fan.

3.1.2. *Traversing system*

At first a fully automatic traversing system (*traversing A* in the following) was adapted for the use with the pipe flow facility. However, pointing a laser distancemeter on the probe's prongs it was discovered that when exposed at the highest operating velocity (~ 35 m/s), the probe was oscillating around the

FIGURE 3.3. Inlet section of the pipe flow facility

static position with a semi-amplitude of 0.1 mm. Since the reduction of these vibrations appeared to be a critical task, it was decided to use a stiffer traversing system (*traversing B* in the following) designed and constructed by Österlund (1999). This traversing system was tested with the distancemeter and showed much smaller oscillations (between 3 µm and 20 µm depending on the probe-holder/probe configuration) at the highest operating velocity. These values are of the order of $(0.4 \div 2)\ell_*$ for the highest Re number case, so this traversing system was considered accurate enough and was the one used for the measurements. In the following further details and the results of the vibrational analysis for both the traversing systems are shown.

3.1.2a. *Description and vibrational analysis of the traverse A.* The traverse A is showed in Figure 3.4. It is made up of an airfoil-shaped supporting arm which slides on a small rail and a positioning screw. A 30 cm long probe holder is connected to the supporting arm, the probe (not shown in the figure) is inserted inside the probe holder and fastened with a small screw. The whole system can move forward and backward sliding on two rails. It is worth noting that with this configuration we obtain a horizontal traversing, in opposition to the traverse B, where the traversing occurs along the vertical direction.
To check the behaviour of the traversing system under flow condition the laser beam of a MicroEpsilon ILD 1700 distancemeter, with a nominal accuracy of 0.5 µm and a frequency resolution of 2.5 kHz, was pointed directly on the prongs (as shown in Figure 3.6) and close to the juncture between the probe holder and the supporting arm (point A in Figure 3.4). To have some clues

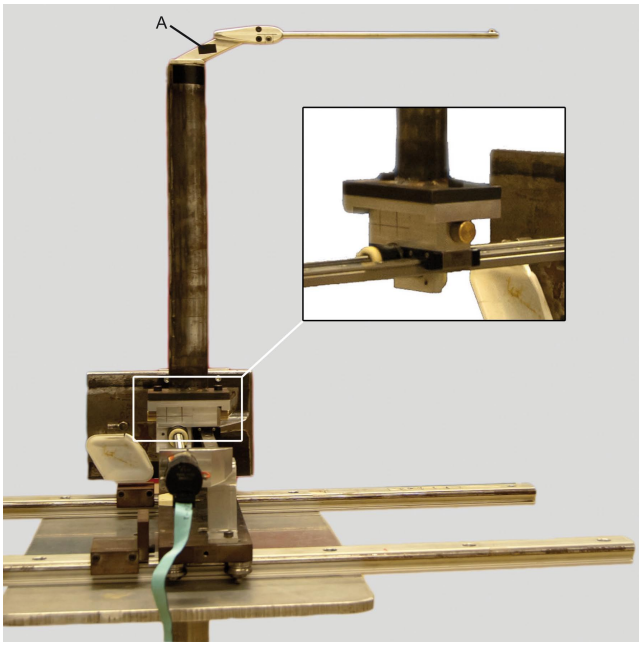

FIGURE 3.4. Traversing A, with a detailed view of the juncture between the positioning screw and the airfoil-shaped arm

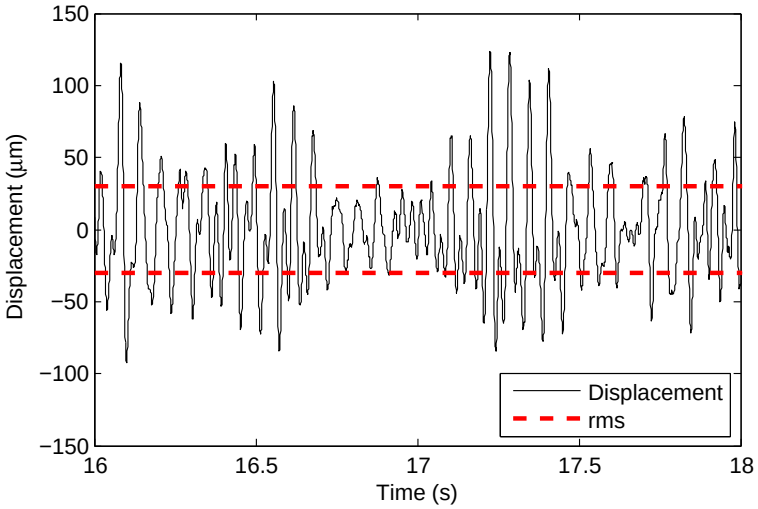

FIGURE 3.5. Prongs displacement for Traversing A at ~ 35 m/s in measurement position (red: standard deviation)

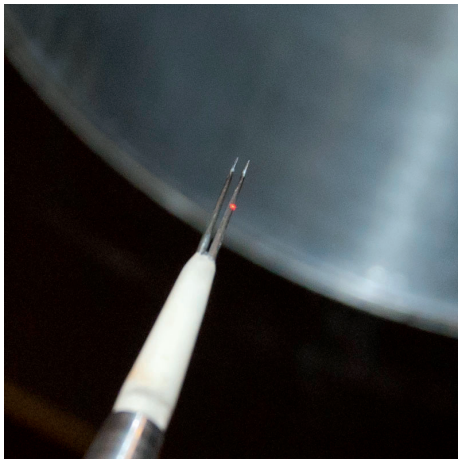

FIGURE 3.6. Laser beam pointed on one of the prongs.

on the understanding of the vibrational mechanism, the measurements were taken at different flow speeds and with the traversing system in two different positions with respect to the pipe outlet: a *measurement position* with the prongs positioned just at the pipe outlet and a *inside position* with the entire probe holder inside the pipe, so that the support arm was not exposed to the emanating jet. In Table 3.1 the semi-amplitude of the vibration is reported for the different cases, while in figure 3.7 the vibration power spectra for the prongs and the support arm are shown. The conclusions that can be drawn from those data is that the most powerful vibrational modes are generated by the action of the jet on the support arm and then amplified along the long and slim rod of the probe holder.

	prongs displacement		point A displacement	
	peak	std	peak	std
measurement position	123 µm	30 µm	30 µm	8 µm
inside position	//	//	3 µm	1 µm

TABLE 3.1. Vibrational analysis results for traverse A

3.1.2b. *Description and vibrational analysis of traverse B.* Figure 3.8 shows the traverse B mounted on its supporting table. The entire traversing mechanism is hidden from the flow inside a metallic box covered with a circular plate.

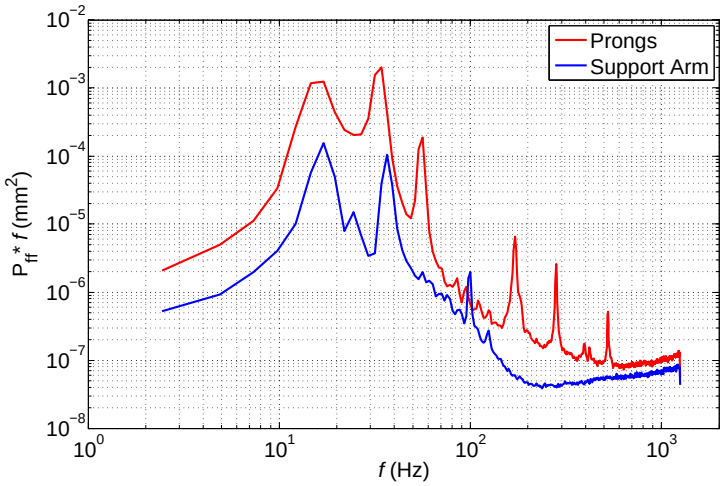

FIGURE 3.7. Vibration Power Spectra for Traverse A at maximum velocity in meausurement position

The traversing arm moves upward and downward inside two couples of wheels, which support it on its way, reducing vibrations. To be sure that the circular plate did not affect the free development of the jet, two cotton wires (so called *tufts*) were fixed on the plate, in order to visualize whether the flow hit the surface or not. The vertical range is 150 mm with a relative accuracy of ±1 µm. As shown in the figure the traverse was clamped tightly to an aluminium beam, screwed on a heavy and stable table.
In the choice of the probe/probe-holder combination there is the need to take into account two different phenomena: the aerodynamic disturbance induced by the probe-holder/probe configuration on the flow field and the effect of the inaccuracy on the determination on the probe position due to oscillations and elastic deformations induced by the flow. The choice of long and slender geometries is optimal when aerodynamic disturbances are concerned, but these shapes can easily amplify vibrations.
To have a deeper insight on the effect of the flow on the system it was then decided to perform a vibrational analysis on the different probe-holder/probe configuration shown in Figure 3.9. The measurements were taken with the probe located at the centre of the pipe and 2 cm downstream the pipe outlet. After tightening all the stopping screws that keep the probe holder and the probe in their place the fan was turned on and let run for a while in order that the probe and probe holder's position adjust under flow condition, then the fan was turned off. Once the velocity decayed, the distancemeter was nulled, i.e. set to zero, and the fan was turned on again and the actual measurement

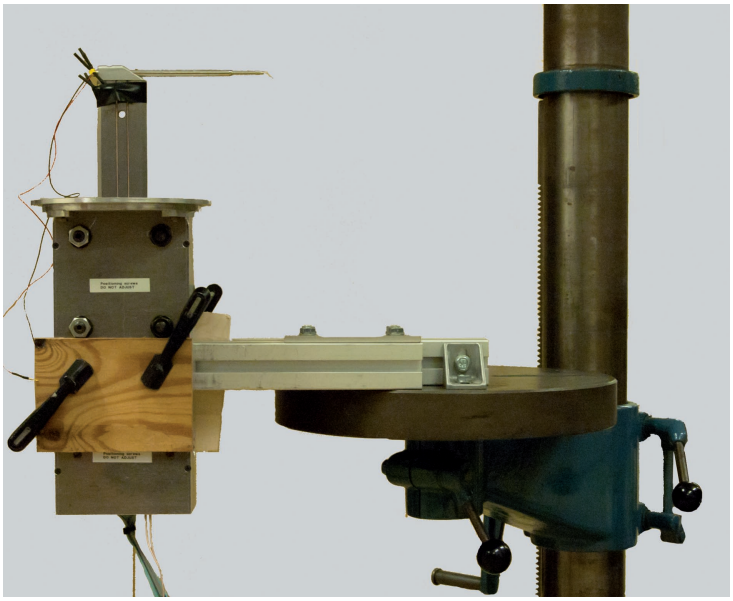

FIGURE 3.8. Traversing system B and its supporting table.

started. This procedure ensured that also the mean position deviation is measured correctly. The results are reported in Table 3.2.
It appears clearly that the most stable configuration is configuration (b) (straight probe holder and straight probe), but this configuration cannot be used for boundary layer measurements, because the aerodynamic blockage would effect deeply the flow inside the boundary layer. It was therefore decided to use configuration (c). For the highest Re case, the standard deviation is less then one third of the viscous scale ($\ell_* \approx 12\,\mu\text{m}$), while the mean deviation is negligible.

	bent probe holder	straight probe holder	
	b.l. probe (a)	straight probe (b)	b.l. probe (c)
displacement semiamplitude	28 µm	4 µm	14 µm
displacement mean	2 µm	0 µm	−2 µm
displacement std	6 µm	1 µm	4 µm

TABLE 3.2. Vibrational analysis results for traverse B

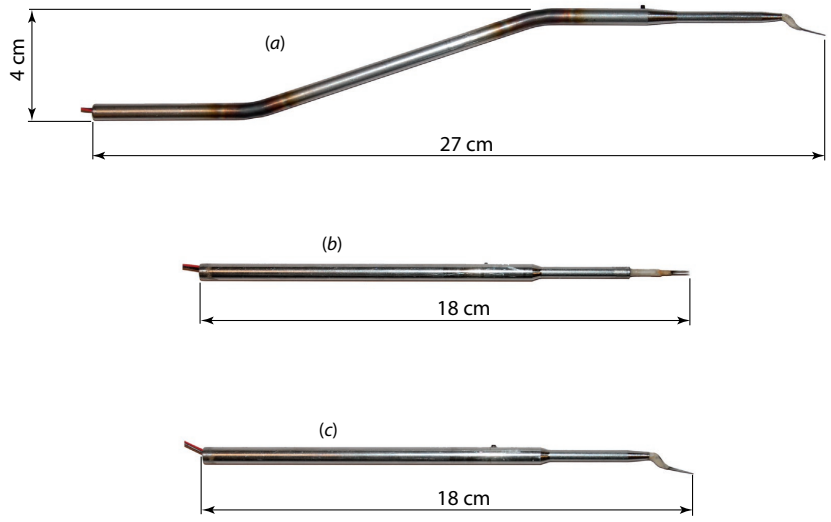

FIGURE 3.9. Different probe and probe holder configurations. *a*) Bent probe holder with boundary layer probe, *b*) Straight probe holder with straight probe *c*) Straight probe holder with boundary layer probe

3.1.3. *Hot-wire calibration nozzle and pressure transducers*

The hot-wire probes were calibrated with the conventional technique of the calibration nozzle. The equipment used was a TSI Model 1127. The stagnation chamber of the nozzle is fed with air coming from a compressor, and is kept at constant pressure through a pressure regulator. We can then derive the velocity at the nozzle outlet from Bernoulli's equation as:

$$u = \sqrt{\frac{2\Delta P}{\rho}}, \tag{3.1}$$

where ΔP denotes the mean pressure difference between stagnation chamber and the outlet and ρ the density. The total pressure (relative to the ambient) and the temperature inside the stagnation chamber are measured with a pressure transducer and a thermocouple. Since an accurate description of the boundary layer requires an accurate calibration at low speeds, a highly accurate pressure transducer is needed. These instruments have a small range of measurement, so it was not possible to use just one pressure transducer for the whole calibration. For the range $0 \div 130\,\mathrm{Pa}$ (which correspond approximately to $0 \div 14\,\mathrm{m/s}$), a pressure transducer of type MKS 120A Baratron with a relative accuracy of $\pm 0.05\%$ (full scale) was used, while for the higher pressures

range another transducer with the range $0 \div 1400\,\mathrm{Pa}$ was used. For pressure differences lower than 130 Pa the signals of both the two pressure transducer were acquired, in order to check whether their results were comparable, so that no discontinuity on the data could appear when switching from one pressure transducer to the other. In Figure 3.10 the square root of pressure ($\propto U$) measured with both the pressure transducers is plotted against the signal of the hot-wire probe ($\propto U^n$, where n is a King's law parameter [see eq. 3.8] determined after calibration), we notice that the values of the two pressure transducers are always comparable, but not for very low pressure differences (less than 4 Pa) where just the MKS transducer has a smooth, i.e. unscattered, behaviour.

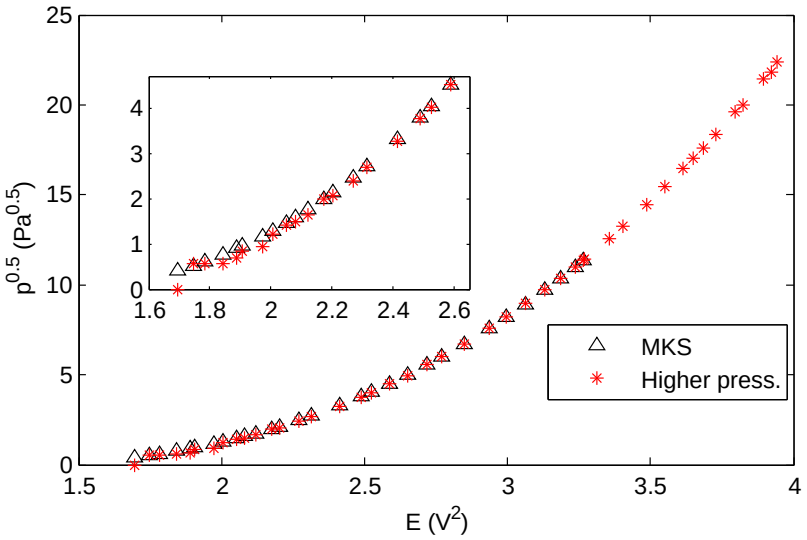

FIGURE 3.10. Comparison of the values of the two pressure transducers in the range $p = 0 - 130\,\mathrm{Pa}$. This images shows how the two pressure transducers give comparable results over most of the common range ($p = 0 - 130\,\mathrm{Pa}$), but not at low pressures (inset).

The ambient absolute pressure and the temperature are measured during the calibration in order to calculate the air density from the ideal gas law. Regulating the total pressure inside the stagnation chamber we obtain different known velocities at the nozzle outlet, where the hot-wire probe is mounted, and is then possible to calibrate the hot-wire probe.

3.1.4. *Hot-wire anemometer system and data acquisition system*

The hot-wire anemometer system used in the experiments was a Dantec StreamLine 90N10 frame in conjuction with a 90C10 constant temperature anemometer module for velocity measurement and a 90C20 temperature module for cold wire temperature measurement. In order to reduce the temperature effects on the signal, the overheat resistance ratio (see eq. 3.12) for all the measurements was set to 110%, a part from one measurement taken with overheat set to 80%. A gain and offset were applied to the bridge signal in order to use all the data acquisition card range, which was a 16-bit analog to digital converter of type NI PCI-6014.

3.2. Hot-Wire Anemometry

3.2.1. *Introduction and physical background*

3.2.1a. *General introduction on hot-wire anemometry.* The idea lying beneath hot-wire anemometry is that a body exposed to a fluid stream will be cooled by the flow in a way related to the flow velocity. The first hot-wire anemometers were used in the beginning of the 20^{th} century and consisted of about 10 cm long wires with a diameter of few tenths of millimetre. Nowadays, the sensitive element of a commercially available hot-wire probe is a wire with a diameter of 5 µm and a length of about 1 mm, typically made of tungsten or platinum, attached on the tip of two supporting needles (*prongs*) and heated by an electric current. When the probe is exposed to a fluid stream it will be cooled by the flow, with a cooling effect which can be related to the flow velocity. To allow velocity measurements in liquid, different type of sensor, called hot film, are used, but a description of those is out of the purpose of this report. There are four different ways of operating a hot-wire probe: the Constant Temperature Anemometry (CTA), the Constant Current Anemometry (CCA), the Constant Voltage Anemometry (CVA) and the pulsed wire anemometry. The most common is Constant Temperature Anemometry, which supply a sensor heating, i.e. a current, which is variable with the fluid velocity in order to keep constant the resistance, and thus the temperature, of the wire. This is obtained inserting the probe in a Wheatstone bridge with an adjustable resistance and connecting one side of the bridge to a differential amplifier, as shown in Figure 3.11. On one side of the amplifier an offset voltage is imposed which, amplified, gives a constant current through the bridge, bringing the wire under no flow condition to a temperature dependent on the value of the variable resistance of the bridge (R_3 in Fig. 3.11). When the flow cool down the wire, the amplifier senses the bridge unbalance and increases the current in order to restore the balance, keeping the resistance of the probe constant. Measuring the voltage at the top of the bridge we know the instantaneous current, thus the instantaneous heating power, which can be related to the flow velocity. In Constant Current Anemometry the probe is inserted in a Wheatstone bridge as before,

but now the current going through the bridge is kept constant (see Fig. 3.12). Measuring the voltage between the two sides of the bridge is possible to know the instantaneous value of the probe resistance, which can directly be related to the flow velocity. In Constant Voltage Anemometry the electronic circuit is designed in order to have a constant voltage drop on the probe (see Fig. 3.13): the output signal E is dependent on wire resistance and thus on flow velocity. In pulsed wire anemometry two hot-wires are used: one of them heat momentarily the fluid around itself, this spot of heated flow is then convected downstream to the second wire which act as a temperature sensor. The time of flight of this spot is related to the fluid velocity. This section cannot describe all the issues related to hot-wire anemometry, but the literature on the subject is huge and the reader is referred to classical textbooks as the ones by Perry (1982), Lomas (1985) and Bruun (1995).

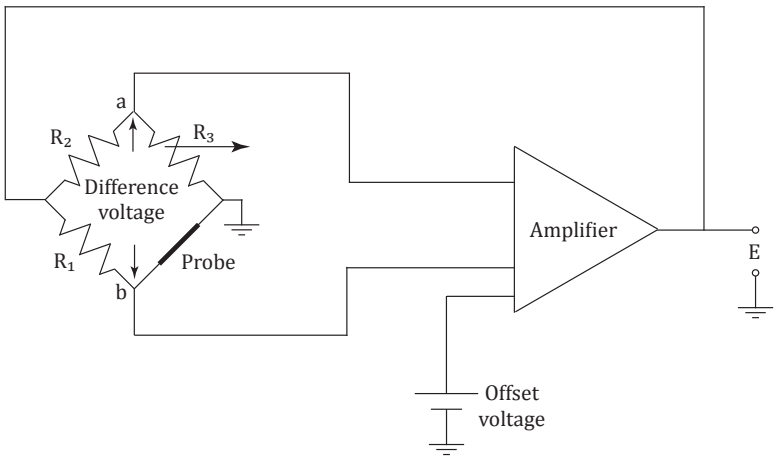

FIGURE 3.11. Schematic of a constant temperature anemometer (CTA).

3.2.1b. *Heat transfer from a heated cylinder.* To understand how the signal from the anemometer is related to the flow velocity, is good to start from the analysis of the behaviour of a heated wire in a stream of fluid. In his pioneering experimental and theoretical work, King (1914), starting from the theoretical analysis by Wilson (1904) about the temperature profile at any point of a 2D flowfield due to a line source of given strength, has derived a solution for the behaviour of a heated wire in a fluid stream, with the hypothesis of constant

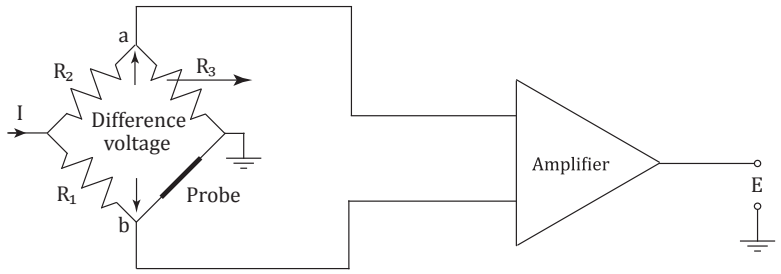

FIGURE 3.12. Schematic of a constant temperature anemometer (CCA).

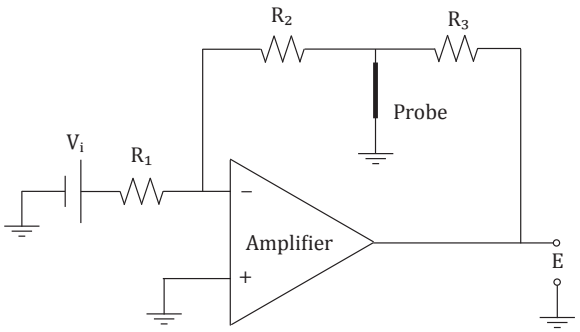

FIGURE 3.13. Schematic of a constant voltage anemometer (CVA).

temperature on all the wire's surface. For the case of negligible natural convection, i.e. high velocity, he found:

$$\frac{W_f}{L(T_w - T_a)} = \kappa + \sqrt{2\pi\kappa c_p \rho D V} \tag{3.2}$$

where $W_f, L, T_w, D, T_a, \kappa, c_p, \rho, V$ are respectively the heat loss due to forced

convection, the wire's length, temperature and diameter, the fluid's temperature, thermal conductivity, specific heat, density and velocity. It is possible to express the heat loss due to forced convection by means of the heat transfer coefficient h as:

$$W_f = h\pi DL(T_w - T_a). \tag{3.3}$$

These relations can also be written using the nondimensional Nusselt, Prandtl and Reynolds numbers relative to the wire

$$Nu = \frac{hD}{\kappa}\,, \qquad Pr = \frac{c_p\mu}{\kappa}\,, \qquad Re_w = \frac{\rho DV}{\mu}\,,$$

obtaining

$$Nu = \frac{1}{\pi} + \sqrt{\frac{2}{\pi} Pr Re_w}\,, \tag{3.4}$$

which is known as *King's Law*.

3.2.2. *Calibration*

3.2.2a. *Conventional hot-wire calibration.* A hot-wire probe is of course different from a infinitely long cylinder: the wire has a finite length and is soldered on two prongs connected to the stem of the probe. Aerodynamic disturbances due to the probe structure, heat conduction from the wire towards the prongs and natural convection phenomena make vain the attempts to find a general law to relate the hot-wire signal to the flow velocity. Therefore, each probe has to be calibrated exposing it to a set of known velocities and measuring the voltage response. The analysis presented in the previous paragraph can nevertheless give some clues on the general shape of the relation between velocity and hot-wire signal. In steady conditions all the heat generated on the wire by Joule's heating is transferred to the surrounding by means of natural convection (W_n), forced convection (W_f), conduction (W_c) and radiative heat transfer (W_r):

$$\frac{E_w^2}{R_w} = W_n + W_f + W_c + W_r\,, \tag{3.5}$$

where R_w is the probe resistance and E_w is the voltage difference across the wire, proportional to the top of the bridge voltage, which is the measured signal E. Starting from equation (3.3), we can write the forced convection term as function of the Nusselt number as:

$$W_f = L\pi\kappa Nu(T_w - T_a)\,. \tag{3.6}$$

In constant temperature anemometry the probe resistance is kept constant, we can thus write:

$$E^2 \propto \frac{E_w^2}{R_w} \approx W_f \propto Nu(T_w - T_a) \,, \tag{3.7}$$

where the influence of the ambient temperature has to be taken into consideration just when the temperature changes during a measurement or between the calibration and the measurement (see §3.2.2b). King's law can then be written as

$$E^2 = A + BU^n \,, \tag{3.8}$$

where A, B and n are constants determined fitting the calibration data to this expression. According to equation (3.8), A is equal to the square root of the voltage at zero velocity, but the best fit of calibration data is found for smaller values due to the effects of free convection. At the same time, the exponent n should have, according to the original expression of King's law, i.e eq. (3.4), the value $n = 0.5$, but the fitting of calibration data suggests usually a smaller value. A modified version of King's law was proposed by Johansson & Alfredsson (1982) to take into account the natural convection phenomena, not negligible at low velocities:

$$U = k_1(E^2 - E_0^2)^{1/n} + k_2(E - E_0)^{0.5} \,. \tag{3.9}$$

When a high number of calibration points is available over the entire velocity range, also a simple polynomial of the form

$$U = C_0 + C_1 E + C_2 E^2 + C_3 E^3 + ... \tag{3.10}$$

can be used to fit the calibration data (see George *et al.* 1989).
In Figure 3.14 a comparison of different fitting laws of the calibration data is shown. A high order polynomial fitting follows better the calibration data than the modified King's law throughout the entire range, especially at low speed, but we can notice in Figure 3.14(b) that the modified King's law is the only one which has a continuous behaviour between the point at zero velocity (E_0) and the calibration point at the lowest speed. A check of the Probability Density Function of the hot-wire signal showed that for all the measurement points the hot-wire signal was always in the calibration range: it was hence decided to use a 10^{th} order polynomial fit as a calibration law. Despite the high order of the polynomial no wiggles occurred, because of the high number of calibration points available.

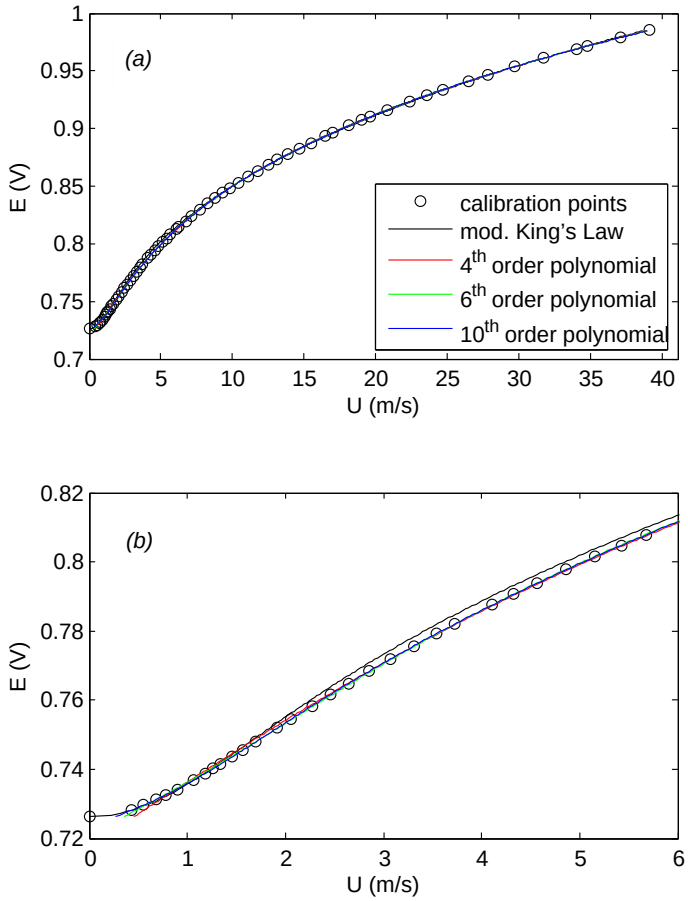

FIGURE 3.14. Calibration of the hot-wire probe: different fitting laws of the calibration data on the entire velocity range (a) and a detail of the low speed range (b).

3.2.2b. *Temperature compensation of the hot-wire signal.* Since a hot-wire anemometer measures the velocity from the cooling effect on a wire, a dependence on the flow temperature can be easily expected, and is shown in equation (3.7). Looking at equation (3.4), we see that Nu is mainly independent on temperature, we can thus write that at the same flow velocity:

$$E(T_{ref})^2 = E(T)^2 \frac{T_h - T_{ref}}{T_w - T} \ , \tag{3.11}$$

where T_h is the fixed hot-wire operating temperature, T is the ambient temperature at which the measurement was taken and T_{ref} is a reference temperature, usually the average of the temperature during calibration. With the aid of equation (3.11), we can hence compensate the temperature effect, obtaining the bridge voltage that we would have had if we had measured at temperature T_{ref}. The only uncertainty is the value of T_w, which is not known *a priori*: a constant temperature anemometer is operated at a certain *overheat ratio*, a_R, defined as:

$$a_R = \frac{R(T_h) - R(T_{ref})}{R(T_{ref})} \ . \tag{3.12}$$

For small temperature changes a linear dependence of resistance on temperature can be assumed, leading to the expression

$$R(T_h) = R(T_{ref})[1 + \alpha_{el}(T_h - T_{ref})] \ , \tag{3.13}$$

where α_{el} is the temperature coefficient of electrical resistivity. We can thus express the overheat ratio as:

$$a_R = \alpha_{el}(T_h - T_{ref}) \ . \tag{3.14}$$

Substituting this expression in equation (3.11), after some algebraic passages we obtain:

$$E(T_{ref})^2 = E(T)^2 \left(1 - \frac{T - T_{ref}}{a_R/\alpha_{el}}\right)^{-1} \ . \tag{3.15}$$

The temperature coefficient of electrical resistivity is provided in the manufacturers' data-sheet or found tabulated in literature, see for instance Bruun (1995), but some authors (van Dijk & Nieuwstadt 2004; Örlü 2009) has noted differences between the tabulated value and the one observed during experiments. These discrepancies might be due to small impurities in the Platinum crystal-structure (Bradbury & Castro 1972) or caused by the tormenting process during the production of the wire, or during the assemblage on the prongs. For these reasons the parameter α_{el} can be considered a characteristic of every single probe, and an iterative approach to determine its value was performed on every probe used during the experiments. At first a set of many calibration points (about 70) was taken at ambient temperature spanning the entire velocity range expected in the experiments with a prevalence in the low speed range,

then a smaller set of calibration points (about 15) was taken at higher temperature, heating the flow entering in the calibration unit. For every calibration point the temperature is measured inside the stagnation chamber and not at the nozzle exit, in order that the temperature probe would not disturb the flow used for calibrating the hot-wire. This means that the acquired temperature is a total temperature (T^0), different from the static temperature the flow has at the nozzle exit. Lomas (1985), Fingerson & Freymuth (1996), Sandborn (1972) among others have reported that the temperature sensed by a hot-wire probe is not the static temperature, but the recovery temperature T_r defined as:

$$\frac{T_r}{T^0} = \frac{1 + r\frac{\gamma-1}{\gamma}M^2}{1 + \frac{\gamma-1}{\gamma}M^2} \,, \tag{3.16}$$

where $r = \sqrt{Pr}$ (in the case of air at the temperature range of our interest $r = 0.84$). For a velocity of 35 m/s and a temperature of 305 K, the difference between total and recovery temperature is around 0.1 K, hence can safely be neglected and the temperature of the thermocouple used as temperature T in equation (3.15). To determine the calibration law of the probe, we want to correct the temperature effect on each point of the first set, but to use equation (3.11) we need to know α_{el}. An iterative procedure in two steps was used, using as a starting point for α_{el} the value found in literature ($\alpha_{el} = 0.0038\,\mathrm{K}^{-1}$): first we obtain the probe's calibration law at a temperature equal to the average of the static temperatures of the first set of data, correcting the temperature effect with equation (3.11). The second step is to use equation (3.11) to fit the calibration points taken at higher temperature on the calibration law obtained at the first step, determining a value for α_{el}. The procedure is then repeated using the α_{el} value found in the second step until convergence is reached.

3.2.3. *Probe manufacturing and L/d choice*

Even if it is possible to buy already made hot-wire probes from several manufacturers, the sizes and geometries of them might not fit the needs of the user, especially when the study of the small scales of turbulence is concerned: for having a long life expectancy, commercially available probes are made of a welded tungsten wire with a length of at least 1 mm and a diameter of 5 µm, which can be too large for some applications. Moreover, when using a "off the shelf" probe, delivering and repairing time can become an issue. In the *Fluid Physics Laboratory* of the *Linné Flow Centre* at *KTH Mechanics*, a "hot-wire corner" to build and repair hot-wire probes inhouse was established since the mid 80ies. All the probes used for the measurements in this report have been built there, following the guidelines from Alfredsson & Tillmark (2005) and the "oral tradition" of my revisors and of the other researchers of the department. In the following a description of the procedure followed for building the probes is reported.

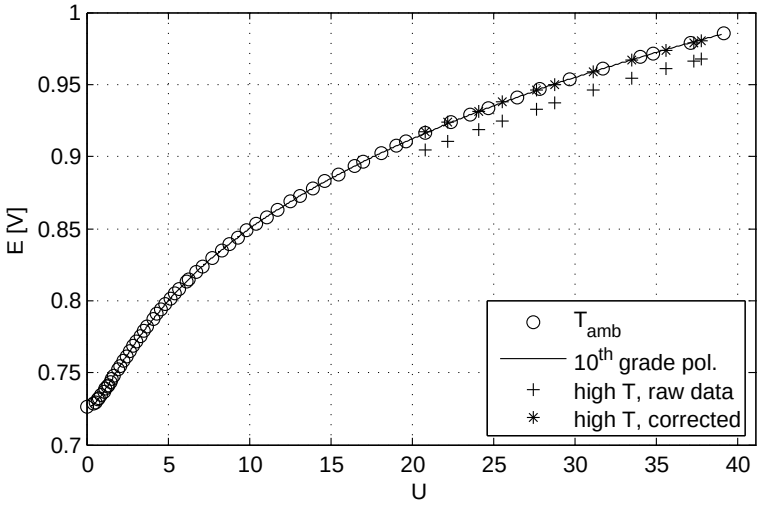

FIGURE 3.15. Calibration of the probe. *Open circles*: calibration point at ambient temperature, *solid line*: calibration law at ambient temperature, *plus symbols*: calibration points at higher temperature, *star symbols*: calibration points taken at higher temperature, with temperature effect correction

The main components of a hot-wire probe are two small cylinders called *prongs* with the function of supporting the wire in the desired position and guaranteeing electrical connection, a rigid frame with structural functions and the wire itself. The prongs were obtained from steel piano wires with a diameter of $0.3 - 0.5\,\mathrm{mm}$, cut to the desired length (about $8\,\mathrm{cm}$) and made pointy by electro-etching with nitric acid with a concentration of $65\%(\frac{m}{m})$. The choice of the diameter has been made in order to fulfil mainly three constrains: the lower limit is set by the flexural rigidity and the condition that the temperature of the prongs be nearly equal to that of the ambient air, whereas the upper limit is set by the requirement that the prongs do not (or to the least) distort the flow in the vicinity of the sensing elements (van der Hegge Zijnen 1951). To speed up the reaction a voltage difference was applied between the wires and the acid, and to obtain the pointy shape the two prongs were moved periodically in and out the acid in order that the foremost part would stay a longer time in the acid. To reduce the aerodynamic blockage of the probe in the near wall measurement the prongs were bent toward the wall. For doing this operation the device shown in figure 3.16 has been designed and built, in order to have a repeatable shape of the prongs. The two steel wires were then inserted in a ceramic tube with two holes, of the type used to insulate thermocouples, to provide electrical insulation and flexural rigidity. When the

desired spacing between the prongs is obtained, they are glued with epoxy to the ceramic tube. On the side of the prongs opposite to where the wire will be soldered, electrical cables ending with golden connector are soldered, in order to connect the probe to the anemometer's cable. Figure 3.17 shows a hot-wire probe together with its components. Once the probe support is assembled, the

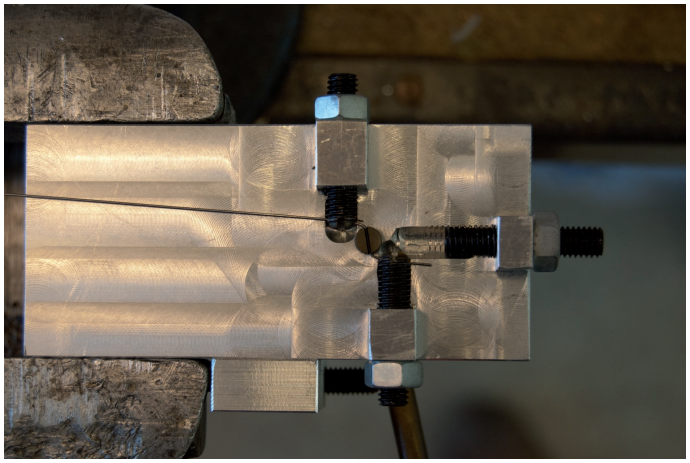

FIGURE 3.16. Bending device used to have a repeatable shape of the prongs.

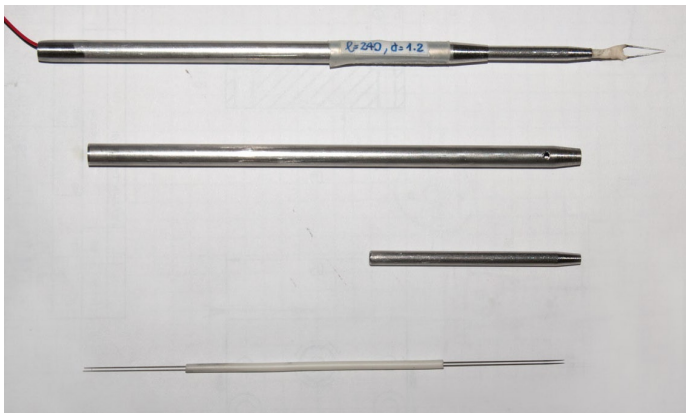

FIGURE 3.17. Probe's components together with a finished probe *(top)*.

sensing element (i.e. the wire) has to be fixed on the prongs' tips. The wire of commercially available probes are usually tungsten wire welded on the prongs,

but to manufacture the probe on your own it is easier to use platinum wires, which can be soldered. Moreover, tungsten wires with diameter smaller than 2.5 µm are not available, therefore the choice of platinum wires is mandatory to build small hot-wire probes. The work has to be done under a microscope and it is necessary to use two micromanipulators, one for the wire and one for the soldering iron. The platinum wires used as a sensing elements are usually available as Wollastone wire, i.e. fine platinum wire clad in a silver coating, thus they have to be immersed for some minutes in the acid in order to etch away the silver. The procedure starts with cutting a small piece of Wollastone wire (about 2 cm), clamping it into a crocodile clamp and immersing the desired length of wire in a beacker containing nitric acid. When the silver is etched away and the platinum wire exposed, the clamp can be mounted on the micromanipulator. The prongs have to be prepared for the soldering, cleaning them with an antioxidant product and covering them with a thin layer of soldering tin (operation made with the aid of a soldering iron). When the prongs are ready, they are covered again with soldering liquid: this will help to keep the wire still for capillarity effect. The wire can now be positioned on the outermost part of the prongs, perpendicular to them. When the wire is in position, a small soldering iron mounted on a micromanipulator is made to touch one prong, in order to solder the wire on it (see Fig. 3.18). The same operation is repeated with the other prongs. After checking if the resistance value is around the expected one for the wire length and diameter, the wire excess is broken by bending it moving back and forth the micromanipulator. Figure 3.19 shows one of the hot-wire probes built and used for the experiments.

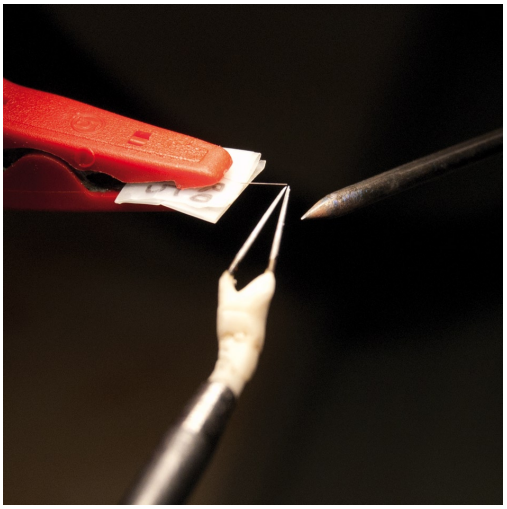

FIGURE 3.18. Close-up figure of the soldering process for a 0.25 mm long boundary layer probe.

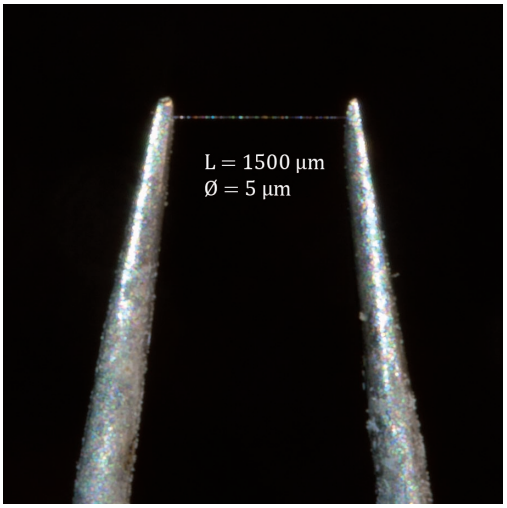

FIGURE 3.19. Close-up figure of a hot-wire probe built for the experiments.

The geometrical parameter L/d, where L is the hot-wire length and d is its diameter, has a leading important in the dynamic behaviour of the hot-wire probe. When the probe is operated, since the Joule heating on the prongs is negligible for their low resistance, they have almost the same temperature of the stream and thus act as heat sinks. A temperature profile $T(x,t)$ (with x the distance measured from the centre of the wire) generates along the wire, governed by the differential equation (Lord 1981):

$$-\frac{\kappa_w \pi d^2}{4}\frac{\partial^2 T}{\partial x^2} + h\pi d(T - T_a) + mc\frac{\partial T}{\partial t} = \frac{I^2}{L}\left[R_{T_{ref}} + \alpha_{el}(T - T_{ref})\right], \quad (3.17)$$

where κ_w is the thermal conductivity of the wire material, h the heat transfer coefficient between wire and the flow, T_a the adiabatic temperature of the wire, m the mass of the wire per unit length, c the specific heat of the wire material, I the applied current, T_{ref} is a reference temperature and $R_{T_{ref}}$ is the resistance at that temperature. The first term in this equation represent the heat conduction along the wire, the second the convective heat transfer between the wire and the flow, the third one the unsteady heat storage in the wire and the last one the Joule hating considering the variation of resistance along the wire. Equation (3.17) can be split in two equations, one for the mean and one for the fluctuating quantity. Solving the mean quantity equation we get the mean temperature distribution, which has the form (Lord 1981):

$$\overline{T} = \overline{T}_a + \frac{a^2}{\alpha_{el} b^2}\overline{R}_a + \left(T_s - \overline{T}_a - \frac{a^2}{\alpha_{el} b^2}\overline{R}_a\right)\frac{\cosh(2bx/L)}{\cosh b}, \quad (3.18)$$

where $\overline{R}_a$ is the mean resistance at the adiabatic temperature, T_s is the temperature of the prongs and the parameters a and b are defined as:

$$a^2 = \frac{\alpha_{el}\overline{I}^2 L}{\pi d^2 \kappa_w} , \qquad b^2 = \frac{\overline{h} L^2}{d\kappa_w} - a^2 .$$

From equation (3.18), we can notice from the term $\cosh 2bx/L$ that low value of L/d mean a longer part of the wire affected by the heat conduction towards the prongs. Other formulations of the temperature profile along the wire are possible, see for instance Bruun (1995, p.24). The effect of the steady temperature profile along the wire is taken into account by the calibration procedure, even when a big portion of the wire is affected by the heat transfer towards the prongs, but conduction losses to the sensor support influence the dynamic behaviour, especially at low frequencies. It is possible to find in literature several criteria on the lower limit for L/d in order that the loss for conduction towards the prongs does not affect significantly the sensor response. Lingrani & Bradshaw (1987*b*), Willmarth & Sharma (1984), Blackwelder & Haritonidis (1983) among others have found as limiting value $L/d > 150 - 200$, when an optimal turbulence *intensity* measurement is concerned, while Künn & Dressler (1985) proposed $L/d > 300$ for optimal *spectrum* measurement. Lately, Hultmark *et al.* (2011) proposed a new parameter, Γ, to describe the significance of heat conduction towards the prongs, instead of the aforementioned L/d.

$$\Gamma = \left(\frac{L}{d}\right)\sqrt{4a_R\left(\frac{\kappa_f}{\kappa_w}Nu\right)} ,$$

where all the parameters were introduced before a part from κ_f which is the thermal conductivity of the fluid evaluated at the wire temperature. They found that $\Gamma > 14$ is required to avoid not-negligible end-conduction effects. Since this parameters is not probe-specific but is dependent on the operative condition in which the measurement is performed (i.e. local velocity and overheat ratio), its use as a criteria in probe manufacturing is not straightforward when a probe is meant to be used in various situations, but it can be helpful in the data analysis.
In Table 3.3 a list of the probes built and used for the measurements is presented. The high L/d value of probe A is due to the fact that the probe was used both as a hot-wire probe for velocity measurements and as a cold-wire probe for temperature measurements. The low value of L/d for probe C is due to the limitation on the resistance value that can be handled properly by the anemometer.

probe	L	d	L/d	α_{el}
A	0.24 mm	1.25 µm	200	$2.5 \cdot 10^{-3}\,\mathrm{K}^{-1}$
B	0.32 mm	2.50 µm	128	$3.7 \cdot 10^{-3}\,\mathrm{K}^{-1}$
C	0.80 mm	5.00 µm	160	$3.6 \cdot 10^{-3}\,\mathrm{K}^{-1}$
D	1.50 mm	2.50 µm	600	$3.3 \cdot 10^{-3}\,\mathrm{K}^{-1}$

TABLE 3.3. List of the characteristics of the probes used in the measurements

3.2.4. *Cold-wires for temperature measurements*

When a hot-wire probe is operated in constant current mode with a current low enough to make the Joule heating negligible, it is referred as *cold-wire* and can be used to measure the instantaneous temperature of a fluid stream. The unheated wire exposed to a fluid stream will have an instantaneous temperature equal to the one of the flow, its resistance will thus vary due to the temperature effect on resistance showed in equation (3.13), changing the voltage drop through it. The probe indicated with letter D in Table 3.3, was used also as a cold wire: a calibration a against thermistor thermocouple was performed and a linear relationship between the temperature and the signal from the constant current anemometer (CCA) was found to represent the calibration curves over the temperature range of interest.
For cold-wire temperature measurements, the frequency response of the probe is much lower than for a hot-wire velocity measurements with the same probe. As pointed out in Millon *et al.* (1978), the attenuation of the signal is due both to the thermal inertia of the wire and to the heat conduction towards the prongs. The attenuation due to heat conduction towards the prongs is mainly active in the low frequency range, while the thermal inertia of the wire attenuate mainly the high frequency range. The transfer function of the probe depends strongly on the geometry of the prongs and on how the wire is bonded at its end, as pointed out in Parantheon *et al.* (1982) and Dénos & Sieverding (1997). Tsuji *et al.* (1992) recommend an L/d ratio larger than 400 in order not to have unacceptable error in the measured temperature variance, but their results are relative to a probe in which the prongs are soldered to a un-etched portion of the Wollastone wire of length $L/2$ on each side (where L is the sensitive, i.e. etched, portion of the wire). Since this geometry, according to Parantheon *et al.* (1982), proved to reduce the heat loss to the prongs, an even larger L/d ratio was chosen. Since the cut-off frequency of the probe is mainly due to the thermal inertia of the wire, the end-conduction effect can be neglected in its determination: experimental data in Dénos & Sieverding (1997) suggest a cut-off frequency of around 900 Hz for a platinum wire with a diameter of 2.5 µm and a length of 1.5 mm operated at 20 m/s.

CHAPTER 4

Measurement matrix and preparations

4.1. Measurement matrix and acquisition procedure

The full range of experimental condition is given in Table 4.1, where the experiments are grouped according to the hot-wire probe used. The measurements have been taken with the probe located around two diameters upstream the outlet, in order to prevent the influence of the emanating jet on the results. Before starting the measurement, the probe was moved toward the wall with small steps and operated; when the influence on the statistics of the heat transfer toward the wall became evident (see §4.3), the position of the probe was considered to be the closest possible to prevent damages and the traverse system was nulled. The position offset y_w from the acquired position and the real one was calculated *a posteriori* from the velocity profiles, with a procedure which will be described in §4.4. The centerline velocities U_{cl} presented in Table 4.1 are the velocities measured at the position $y = R + y_w$, i.e. the centerline position for the traverse system, but, since with the procedure described y_w proved to be always less then 60 µm and the velocity profile is extremely flat around the centerline at the Reynolds numbers of interest, we can consider this value trustable. Re_D is the Reynolds number based on pipe diameter and bulk velocity, which was obtained by mean of a trapezoidal integration of the velocity along the measurement points, adding the no-slip condition fo $y = 0$.
In Table 4.1 R^+ is the already defined friction Reynolds number, ℓ_* is the viscous scale while the letters identifying the probe are the ones used in Table 3.3. L^+ is the hot-wire length in viscous unit and can be related to the spatial-resolution effect; the sampling time is given with respect to the viscous time unit as $\Delta t^+ = (f_{sampl} t_*)^{-1}$ which can be related to the time-filtering effects. Finally, the total sampling time T is given in outer scaling as TU_{cl}/R, which, according to Klewicki & Falco (1990), should exceed several thousands to obtain converged statistics for higher order moments. Since the measurements have been taken using two different fans, this was indicated in the column *fan*. As will be explained in §4.2 the two fans generate different temperature profiles in the pipe, so the correction scheme for temperature effects is different, but no relevance of this difference has been noticed in the results. The symbols in the last column are the one which will be used to identify the single experiment in

all the following images.

Case	U_{cl} (m/s)	Re_D	R^+	ℓ_* (μm)	probe	fan	L^+	Δt^+	TU_{cl}/R	sym.
A_1	6.30	19 750	566	53	A	s	5	0.09	15 700	$\triangledown$
A_2	12.45	39 420	1 038	29	A	s	8	0.30	20 800	$\square$
A_3	13.75	41 480	1 079	28	A	b	9	0.35	22 900	$\circ$
A_4	20.11	63 920	1 568	19	A	s	13	0.70	26 800	$\triangle$
A_5	23.60	71 480	1 721	17	A	b	14	0.88	31 500	$\lozenge$
A_6	32.14	95 780	2 224	13	A	b	18	1.51	32 100	$+$
B_1	14.27	43 640	1 145	26	B	b	12	0.38	23 800	$\circ$
B_2	25.11	76 960	1 858	16	B	b	20	1.01	33 500	$\lozenge$
B_3	35.47	107 300	2 483	12	B	b	26	1.85	35 500	$+$
C_1	6.56	20 360	585	51	C	s	16	$0.15^{(*)}$	16 400	$\triangledown$
C_2	11.46	34 890	937	32	C	b	25	$0.39^{(*)}$	19 100	$\circ$
C_3	13.08	41 150	1 077	29	C	s	29	$0.50^{(*)}$	21 800	$\square$
C_4	23.56	72 440	1 749	17	C	b	47	$1.35^{(*)}$	31 400	$\lozenge$
C_5	31.72	95 910	2 251	13	C	b	60	$2.28^{(*)}$	31 700	$+$
D_1	15.06	45 740	1 174	26	D	b	59	0.41	25 100	$\circ$
D_2	25.65	77 970	1 872	16	D	b	94	1.04	34 200	$\lozenge$
D_3	35.25	104 981	2 420	12	D	b	121	1.78	35 300	$+$

TABLE 4.1. Experimental parameters for present hot-wire experiments. Explanation of column headings and abbreviations is given in §4.1.
$^{(*)}$ sampling frequency limited by the dynamic response of the hot-wire probe and not by the setting of the data-acquisition system; in these cases the frequency response was estimated with the square-wave test on the probe.

4.2. Temperature compensation

When the bigger fan (indicated with *b* in Tab. 4.1) was used to drive the flow through the pipe, the temperature reached in the centerline values of even 12 K above the room temperature. Since the diabatic surface of the pipe adjust its

temperature depending on the temperature difference between centerline and external ambient, a temperature profile generates inside the pipe, in order to respect the boundary conditions on temperature and heat flux at the wall. Hot-wire data need to be compensated for temperature effects (see §3.2.2b), we must hence know or estimate with sufficient accuracy the local temperature during the experiments. The temperature profile inside the pipe were measured with probe D operated as a cold-wire for $R^+ = 1167$, $R^+ = 1821$, $R^+ = 2453$, and in all the experiments the room and centerline temperature were measured with thermistor thermocouple before and after each measurement. The temperature proved do be steady during the time necessary for a whole profile acquisition, with a maximum variation $\Delta T_{before-after} < 0.3$K, moreover the difference in temperature between the centerline and the room temperature depended with good approximation just on flow velocity. It was then decided that to estimate the temperature profile inside the pipe, it was sufficient to shift the measured temperature at approximately the same R^+ in order to match the measured centerline temperature. If this method seems too approximate, one should consider that the aim is not to have an accurate temperature profile for all the experiments, but to correct the hot-wire signal. For this task an accuracy on the local temperature of ±0.5K is sufficient, consider $T - T_{ref} = 0.5$ in eq. (3.15) with an overheat ratio $a_R = 1.1$ lead to a correction of less than 1/1000 of the hot-wire signal, which can be safely considered negligible. Moreover the sensibility of the correction to en error in the value of the temperature decreases with increasing $T - T_{ref}$. When the smaller fan (indicated with s in Tab. 4.1) was used, the centerline temperature proved to be always less then 0.2 K higher than the wall temperature: to correct the hot-wire signal a simple average between the two values was used.

4.3. Heat transfer toward the wall and data selection criteria

Hot-wire data in the region very close to the wall proved to be not accurate: when the thermal conductivity of the wall is much higher than the one of the fluid, the wall extracts heat from the fluid heated by the wire, changing the temperature distribution around the wire and leading to an additional heat transfer from it. If the hot-wire (as often happens), has been calibrated in a free stream, this additional heat loss is read as an additional velocity of the flow. Since this effect increases rapidly approaching the wall, the measured mean velocity seems to increase instead of decrease approaching the wall. A general description of the problem is provided by Bruun (1995), a literature survey about the experimental data and theoretical knowledge of the problem can be found in Bhatia *et al.* (1982), while more recent publications are discussed by Lange *et al.* (1999) and Zanoun *et al.* (2009). Most of the studies agree that for measurements closer than $y^+ \lesssim 5-6$ the heat transfer toward the wall is not negligible and affects heavily the acquired data.

The effect of the additional heat transfer on the velocity variance is not straightforward and an analysis of its influence on the velocity probability density function, or equivalently on the cumulative distribution function (CDF), is required. In the near-wall region Alfredsson *et al.* (2011*a*) established the self-similarity of the CDF in the viscous sublayer. Starting from this consideration, they found that "the turbulent signal is mainly affected by heat transfer to the wall during periods of low streamwise velocity and not necessarily for periods of high velocity". The unsymmetrical behaviour of the measured CDF is evident from the Figure 4.1, where the cumulative distribution function contours in the near-wall region for the measurement case C_2 are shown, and is in contrast with the expected self-similarity of the CDF in the viscous sublayer. This

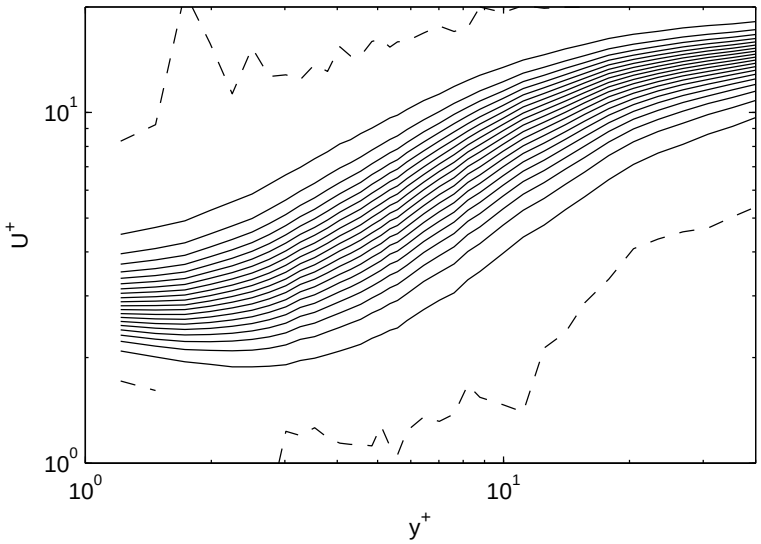

FIGURE 4.1. Velocity CDF contour for case C_2. *Dashed line*: limit of the CDF (i.e. $F(u) = 0$ and $F(u) = 1$); *solid line*: CDF contour for $F(u) = [0.025; 0.975]$ with step of 0.05.

asymmetry lead to a damping of the streamwise velocity variance, which appears to decrease faster than in reality. Following what proposed by Alfredsson *et al.* (2011*a*), Figure 4.1 can also be used to evidence the heat conduction effects: because of the self-similarity of the CDF in the viscous sublayer, the CDF contour lines are expected to be parallel in a log-log plot. The departure from parallelism that can be noticed in the near-wall region is due to the heat conduction effect.

Since the heat loss toward the wall lead to an increase in the measured mean velocity and a decrease in the measured streamwise velocity variance, a good

indicator of the effects of the heat conduction toward the wall on the measurement is thus the local streamwise turbulence intensity (u_{rms}/U). Close to the wall U^+ and $\overline{u'}+$ can be written as a Taylor expansion, obtaining for a pipe flow:

$$U^+ = y^+ - \frac{1}{R^+} y^{+\,2} + o(y^{+\,2}) \tag{4.1}$$

and

$$\overline{u'}^+ = a_1 y^+ + a_2 y^{+\,2} + o(y^{+\,2}) \,, \tag{4.2}$$

from which is possible to obtain

$$\frac{\overline{u'}}{U} = a_1 + (a_2 + \frac{a_1}{R^+}) y^+ + o(y^{+\,2}) \,. \tag{4.3}$$

The coefficient a_1 is positive while a_2 is negative, but $(a_2 + \frac{a_1}{R^+})$ is negative (R^+ has of course a lower bound, because the flow has to be turbulent in order to define R^+). We can thus conclude that the local turbulence intensity in the proximity of the wall is monotonically increasing toward a certain value. As shown by Alfredsson *et al.* (1988), the asymptotic behaviour of the local turbulence intensity is related to the streamwise fluctuating skin friction component:

$$a_1 = \frac{\overline{u'}}{u_\tau} = \frac{\overline{\tau'_x}}{\tau} \,. \tag{4.4}$$

The results of recent direct numerical simulations has shown a Reynolds number dependence of a_1, as clearly shown in Figure 4.2. In the measured data, instead, u_{rms}/U reaches a maximum and then start to decrease because of the additional heat transfer to the wall. For all the current experiments, all the point with $y^+ < 6$ or closer than $1\,\ell_*$ to the measured peak in the streamwise turbulent intensity are considered affected by additional heat loss toward the wall and are gray shaded in all the following images. Figure 4.3 shows the streamwise turbulent intensity vs. y^+ for all the current measurements plotted together with DNS data from Wu & Moin (2008).

4.4. Wall position and friction velocity determination

Since the inner region of wall bounded flows scales on y^+, one should not just measured accurately the flow-field, but should also obtain reliable values of the friction velocity and absolute position. A review of the common measurement technique to obtain an absolute wall position measurement can be found in Örlü *et al.* (2010), but there is also stated that the accuracy of the measurement techniques available at present time is not sufficient when compared to

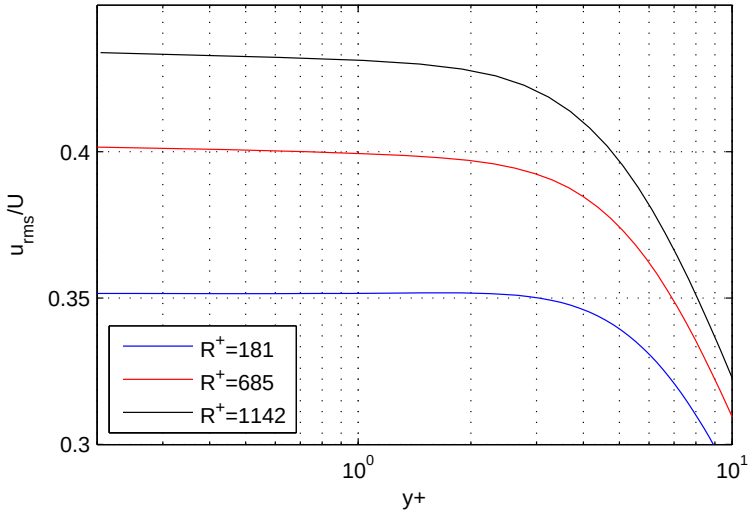

FIGURE 4.2. Details of the near-wall region of streamwise turbulence intensity vs. y^+ at different R^+. Data from DNS by Wu & Moin (2008).

the size of the viscous scale ℓ_* of moderately high Reynolds number flows. Considering now u_τ, a direct measurement of the wall shear stress should always be performed when the interest is to enforce the validity of a scaling behaviour or to determine the log-law constants κ and B (Nagib *et al.* 2004), but, since a direct measurement of the wall shear stress was not available in the current experimental setup, a fitting algorithm was used to determine both the shear stress and the absolute position. Aware of the shortcomings of this approach the data will not be used to enforce any analytical description of the mean velocity profile.

To determine y_w and u_τ, the data considered unaffected by additive heat loss to the wall (see §4.3) were fit on the composite velocity profile proposed by Nagib & Chauhan (2008) (see eq. 2.67), with parameter $\kappa = 0.384$ and $a = -10.43$ when $R^+ > 900$, and $\kappa = 0.384$ $a = -10.68$ when $R^+ \approx 550$: $\kappa = 0.384$ is the value found for pipe flow in experiments by Monty (2005) and simulation by Wu & Moin (2008), while the value for a were obtained by a comparison of the composite profile with in-house DNS data. The fitting procedure was not performed on the whole profile, but just in its inner part, i.e. for $y^+ < 85$ when $R^+ > 900$ and for $y^+ < 40$ when $R^+ \approx 550$, in order to consider just the near-wall points, where the composite fit is more accurate.

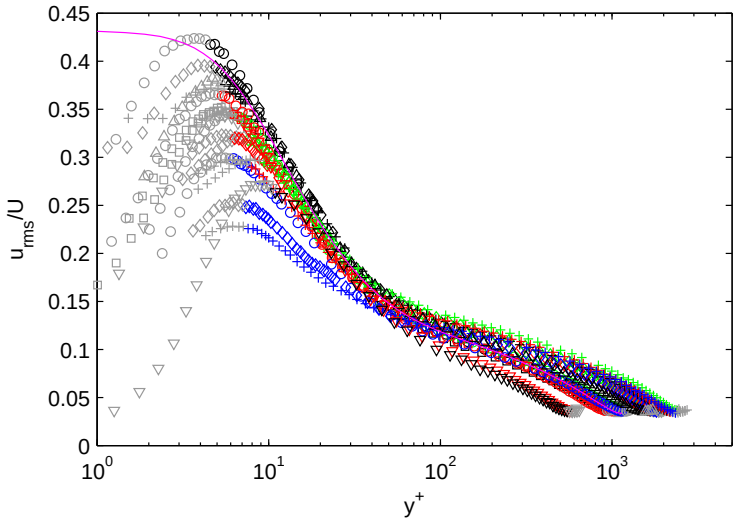

FIGURE 4.3. Streamwise turbulence intensity vs. y^+ for all the current measurements (see Tab. 4.1 for symbols explanation), plotted together with DNS data (*magenta line*) from Wu & Moin (2008) (R^+ = 1142). Gray shaded points are the one identified as affected by additional heat loss or with $y > R$.

4.5. Convergence proof

Figures from 4.4 to 4.7 show the statistics calculated for different sampling time for the case with the lowest sampling time in outer scaling (Case A_1). We can state that for this case, and thus also for all the other cases, the measurements' sampling time was sufficient to have converged statistics for all the statistical moments considered in the analysis.

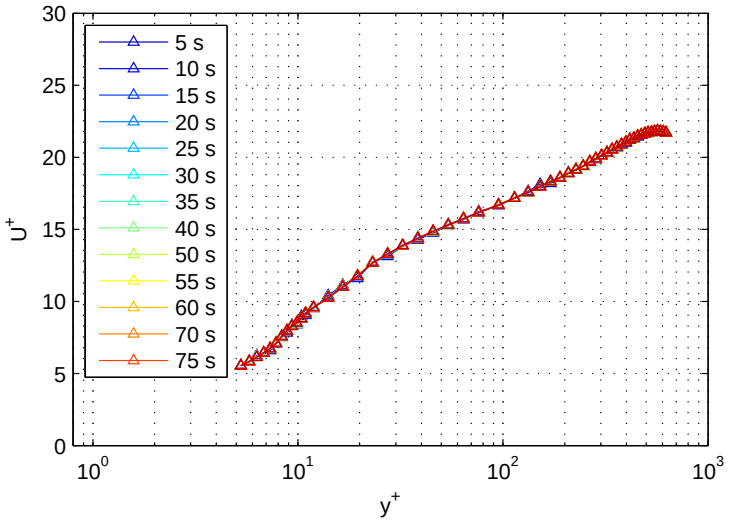

FIGURE 4.4. Convergence proof of the mean velocity for case A_1

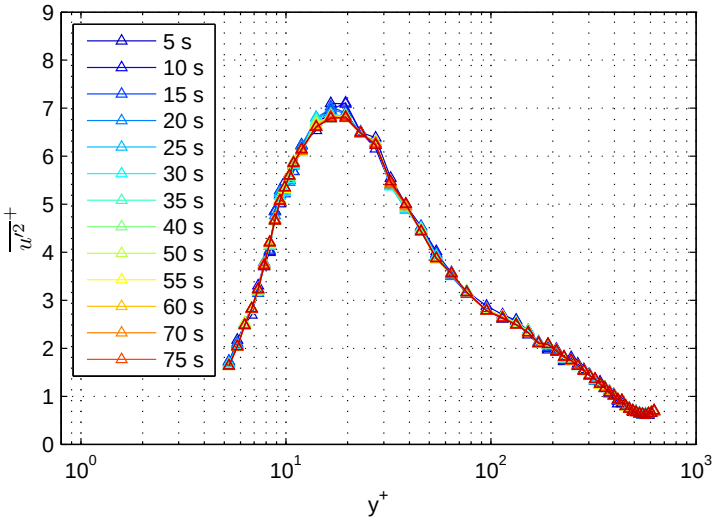

FIGURE 4.5. Convergence proof of the velocity variance for case A_1

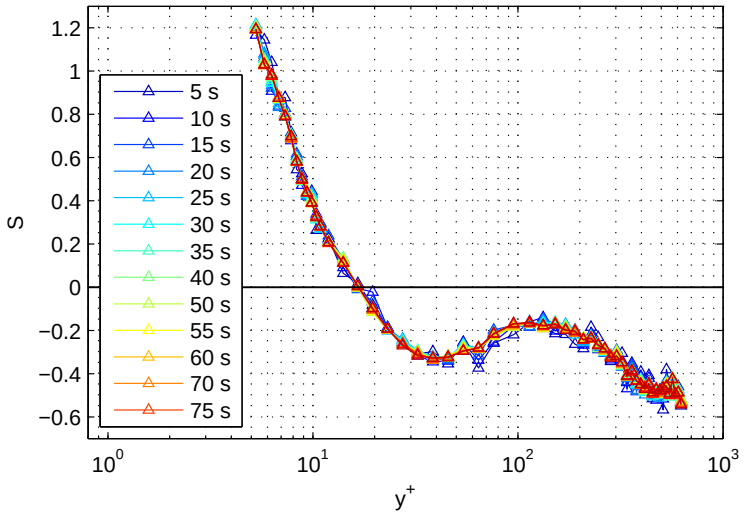

FIGURE 4.6. Convergence proof of the velocity skewness for case A_1

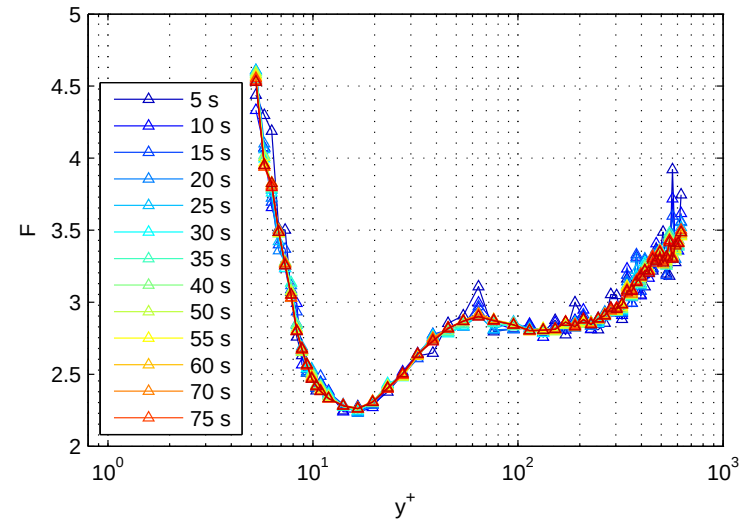

FIGURE 4.7. Convergence proof of the velocity flatness for case A_1

CHAPTER 5

Results and Discussion

In this section the results of the velocity measurements are presented in viscous scaling. After the discussion of the first four statistical moments, autocorrelation spectra and probability density function will be presented. In the last part of this section the results of the temperature measurement performed with the cold-wire will be shown.

5.1. Global quantities

In Figure 5.1 $R^+ = R/\ell_*$, where ℓ_* was calculated from the u_τ obtained from the fitting on the composite profile, is plotted against the Reynolds number Re_D for all current measurements, together with the linear fit of the data $R^+ = 2.16 \cdot 10^{-2}\, Re_D + 178.0$. In Figure 5.1 the ratio between the centerline and the bulk velocity is plotted against the R^+.

5.2. Mean velocity profiles

Figure 5.3 shows the mean velocity for all the seventeen experiments, while from Figure 5.4 to 5.7, measurements with approximately the same R^+ but different L^+ are compared: we notice that no spatial resolution effect are visible on the mean velocity. Figure 5.8 shows the Reynolds number effect on the mean profile: it appears clearly that the range of the overlap region, where the log-law is expected to hold, extends with the Reynolds number. Its lower bound is indeed expressed in viscous scale and is thus dependent on the viscous length ℓ_*, while its higher limit is classically expressed in outer scaling, i.e. is Reynolds number independent for a pipe flow. As already stated in §2.2.2, the log-law region's bounds are debated, with some authors proposing a lower bound of the order of hundreds inner units. In this perspective we should not expect a fully logarithmic behaviour in none of the current experiments, but a trend in the velocity profile reaching an almost-logarithmic behaviour can be observed at least in the highest Reynolds cases (Fig. 5.7).

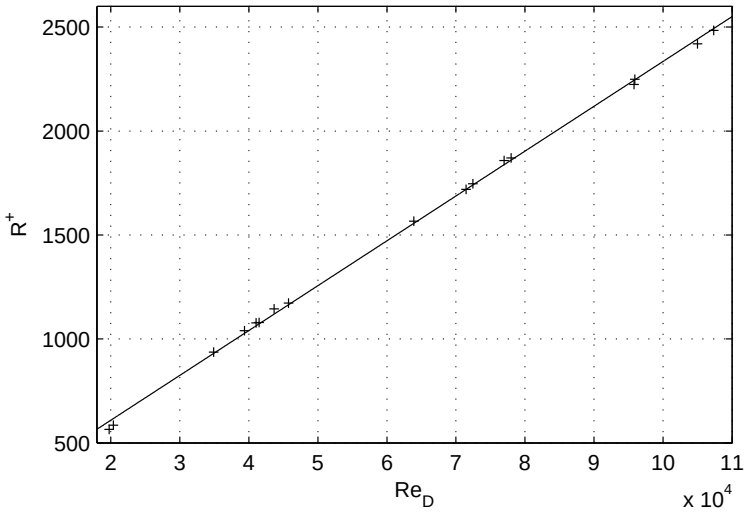

FIGURE 5.1. *Plus*: R^+ obtained with the fitting procedure vs. Re_D for all current measurements; *solid line*: linear fit of the data, $R^+ = 2.16 \cdot 10^{-2}\, Re_D + 178.0$.

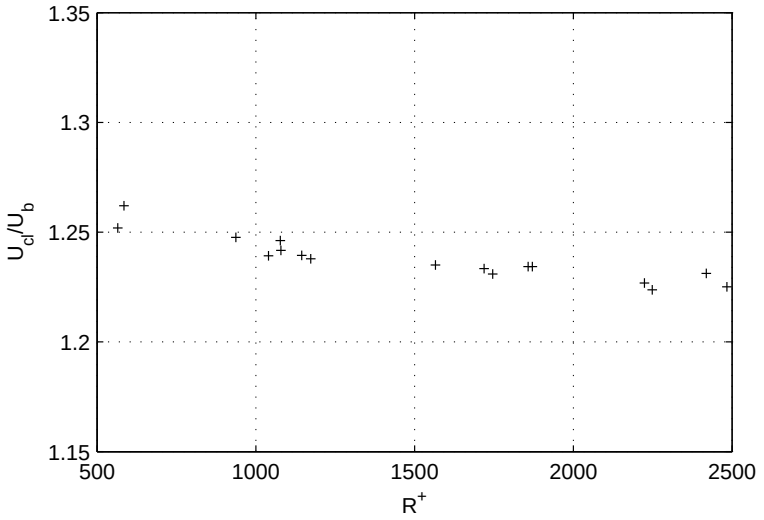

FIGURE 5.2. Ratio between centerline and bulk velocity vs. R^+ for all current measurements.

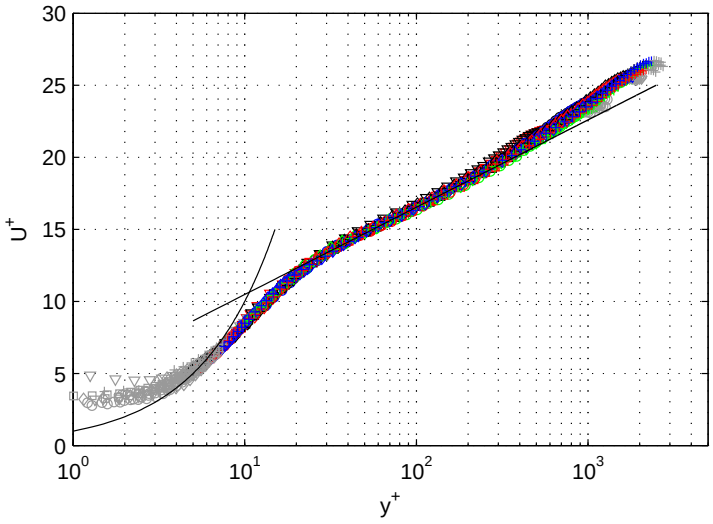

FIGURE 5.3. Mean velocity profile in viscous scaling for all the experiments. Symbols as in Tab. 4.1, *black lines* are the linear profile $U^+ = y^+$ and the log-law with $\kappa = 0.38$, $B = 4.4$. Gray shaded points are the one identified as affected by additional heat loss or with $y > R$.

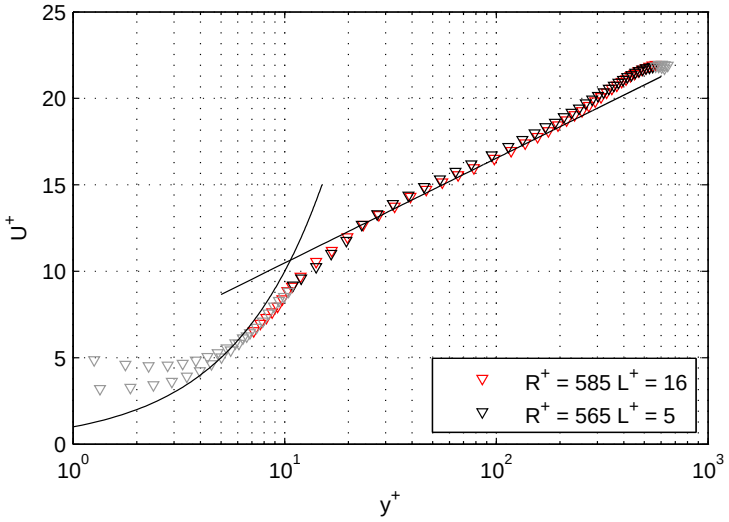

FIGURE 5.4. Mean velocity for $R^+ \approx 550$.

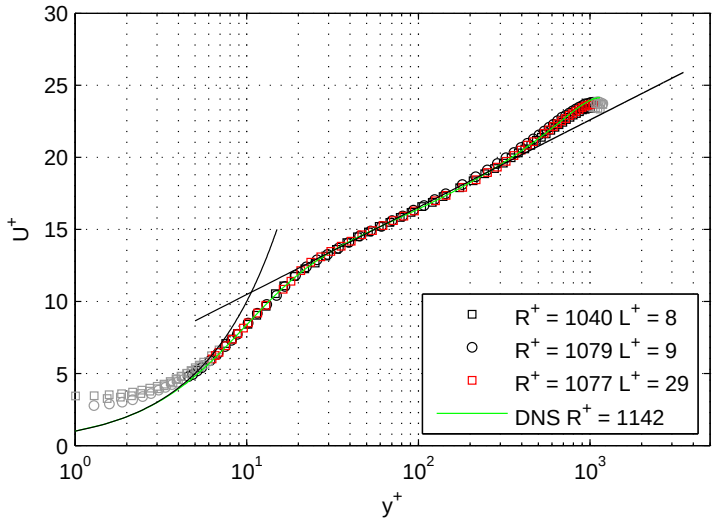

FIGURE 5.5. Mean velocity for $R^+ \approx 1000$. *Green line*: DNS data from Wu & Moin (2008).

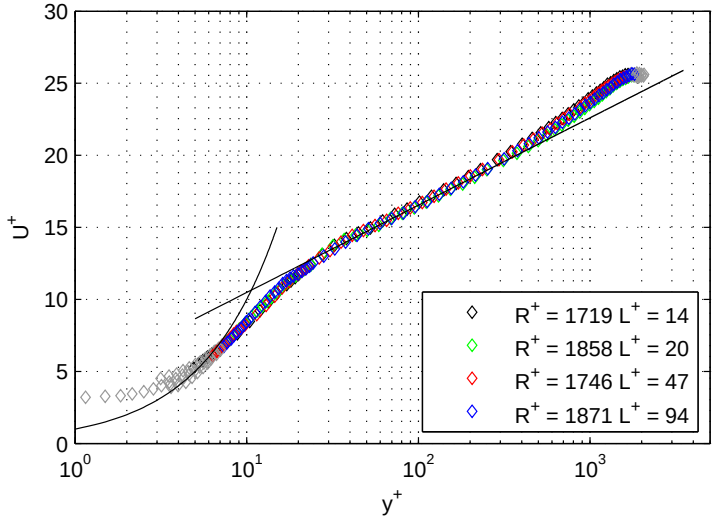

FIGURE 5.6. Mean velocity for $R^+ \approx 1700$.

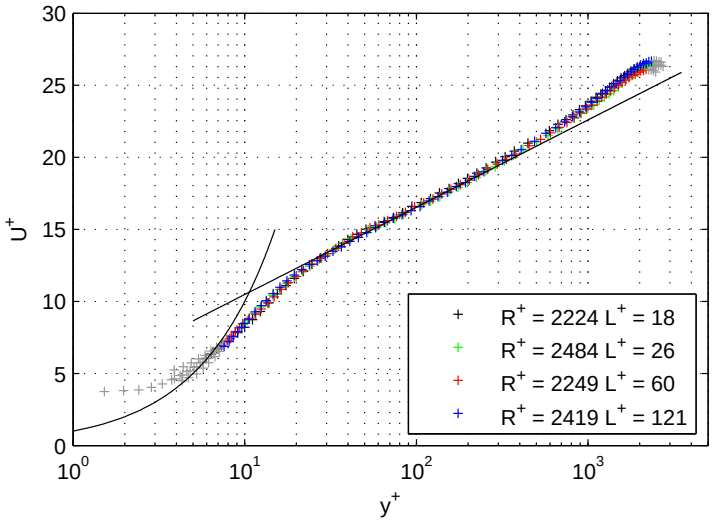

FIGURE 5.7. Mean velocity for $R^+ \approx 2400$.

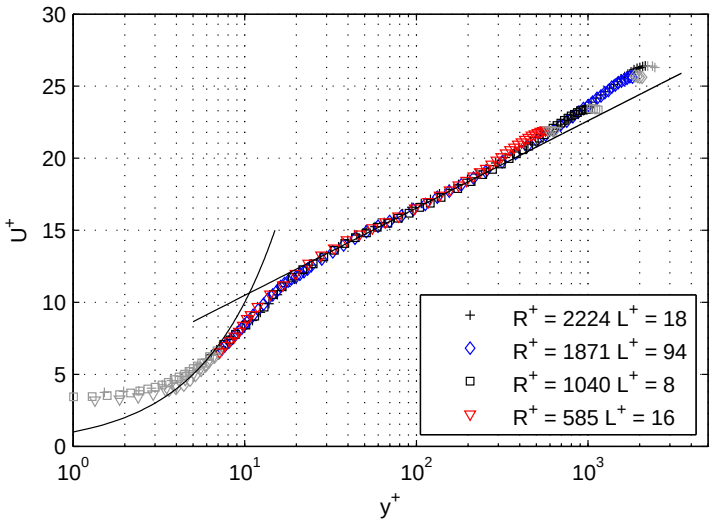

FIGURE 5.8. Mean velocity profiles for different R^+.

5.3. Streamwise velocity variance

Figures from 5.9 to 5.11 show the measured streamwise velocity variance profiles grouped with the Reynolds number. Spatial filtering effects are evident, with a strong attenuation of the measured variance for higher values of L^+, especially apparent in the near-wall region but still active up to $y^+ \approx 200$ as found by Lingrani & Bradshaw (1987*a*). The series of data with green symbols in Figure from 5.9 to 5.11 are obtained with the probe B, which has $L/d = 128$, so we might expect an attenuation of the velocity variance due to the heat loss towards the prongs (see §3.2.3): in the following the data taken with that probe will be neglected.
Figure 5.12 shows instead profiles at different Reynolds number but almost constant L^+, in order to evidence the Reynolds number effect on the velocity variance profiles without the masking due to spatial filtering. The value of the peak in the turbulence intensity grows with the Reynolds number, with a total rise in $\overline{u'^2}^+|_m$ of approximately 15%, which exceed the expected experimental uncertainty. Not only the peak value increase, but the velocity variance increase throughout the logarithmic region. The growth of $\overline{u'^2}^+|_m$ with Reynolds number is consistent with experimental data for pipe and channel by Ng *et al.* (2011), for boundary layers by DeGraaff & Eaton (2000) and Metzger & Klewicki (2001) and in channel flow DNS by Jimnez & Hoyas (2008), but is in contrast with the experimental data by Hultmark *et al.* (2010) obtained in the Superpipe facility at Princeton University.
Ng *et al.* (2011) explained the growth in the peak of velocity variance as the effect of the increasing contribution with Reynolds number of large scales motion on u spectra, in analogy with what done by Marusic *et al.* (2010*a*) for boundary layer data.

5.3.1. *Correction schemes for spatial resolution effects.*

In the following two different corrections schemes for spatial resolution effects will be applied on the data, and their results will be compared.
From an analytical point of view, it is possible to reach, with some assumptions, an expression of the attenuation factor of the measured streamwise velocity variance due to spatial resolution effects. This was first performed by Dryden *et al.* (1937) and extended to consider also misalignment of the probe by Segalini *et al.* (2011*a*). Neglecting the typical non-linearity of of the hot-wire probe response, considering a probe perpendicular to the main velocity component u and a negligible normal component (assumption valid in wall-bounded flow, especially close to the wall where the filtering effect is stronger), we can write the measured velocity u_m as an integral average of the velocity along the wire:

$$u_m = \frac{1}{L}\int_{-L/2}^{L/2} u(\eta, t)\,\mathrm{d}\eta\,. \tag{5.1}$$

With the assumption of homogeneous flow along the wire, the last expression can be written with the use of two point correlation ρ_{11} leading to

$$F_2 = \frac{\overline{u_m'^2}}{\overline{u'^2}} = \frac{2}{L^2}\int_0^L (L-r)\rho_{11}(r)\,\mathrm{d}r\,, \tag{5.2}$$

where F_2 is the attenuation due to the spatial resolution effect while r is the spanwise separation distance between the two points. Segalini *et al.* (2011*a*) expressed the eq. (5.2) as a Taylor expansion in all the even derivatives of the two-point correlation function as

$$F_2 = 1 - \sum_{i=1}^{N} \frac{2L^{2i}}{(2i+2)!}\frac{\mathrm{d}^{2i}\rho_{11}}{\mathrm{d}r^{2i}}\,. \tag{5.3}$$

Considering just the second derivatives of ρ_{11}, which is related to the Taylor microscale λ_g as

$$\rho_{11}''(0) = -\frac{2}{\lambda_g}\,, \tag{5.4}$$

we have

$$F_2 = 1 - \frac{L^2}{6\lambda_g^2}\,. \tag{5.5}$$

To use this correction directly, λ_g has to be measured or estimated. Segalini *et al.* (2011*b*) proposed a method to obtain an estimate both of $\overline{u_m'^2}$ and λ_g, given that two measurements with the same flow condition are performed with (at least) two probes with different wire length. The method is applied on the data obtained from the current experiments and leads to the result showed in Figures from 5.13 to 5.15.

Lately, a semi-empirical correction scheme has been proposed by Smits *et al.* (2011*b*). It is based on the fact that the filtering effect is related to the ratio of the wire length on the local size of the eddies contributing to the turbulence intensity. In the near-wall region the small-scales eddies are the ones which contribute mostly to the local turbulence intensity: since they scale with the Kolmogorov length-scale η, the ratio L/η should be the parameter to use when the filtering effect of the probe needs to be accounted. Since η^+ is approximately constant close to the wall, also L^+ can be used to describe the filtering

effect in this region. According to the attached eddies hypothesis by Townsend (1976), further from the wall the energy-containing eddies scale with the distance from the wall, so an attenuation of the kind

$$\Delta\overline{u'^2} = \overline{u'^2} - \overline{u_m'^2} = f(L/y) \tag{5.6}$$

should be expected.
Considering the whole velocity profile, Smits *et al.* (2011*b*) proposed the expression

$$\frac{\overline{u_m'^2}}{\overline{u'^2}} = [1 + M(L^+)f(y^+)]^{-1} \, . \tag{5.7}$$

In the last expression

$$M(L^+) = \frac{A\tanh(\alpha L^+)\tanh(\beta L^+ - E)}{\overline{u_m'^2}|_{z^+=15}} \tag{5.8}$$

is a correlation for the filtered velocity variance at the location of the inner peak found by Chin *et al.* (2009) ($\alpha = 5.6\cdot10^{-2}$, $\beta = 8.6\cdot10^{-3}$, $A = 6.13$ and $E = -1.26\cdot10^{-2}$ are fitting parameters with no particular physical meaning) and

$$f(y^+) = \frac{15 + \ln(2)}{y^+ + \ln[e^{15-y^+} + 1]} \tag{5.9}$$

takes into account what said before about the local size of the smallest eddies contributing to the turbulence intensity, being almost constant in the viscous layer and then approaching the hyperbole k/y^+.
The results of this correction scheme on the current experimental data are shown in Figures from 5.16 to 5.18.

In Figure 5.19 the results of the two correction schemes presented above are compared. We notice an almost complete accordance at the lowest Reynolds number, but discrepancies appear for the higher Reynolds cases in the value of the peak of streamwise velocity variance, with the correction proposed by Smits *et al.* (2011*b*) leading to a higher value than the one by Segalini *et al.* (2011*b*). Both the corrections show the Reynolds number dependence both of the peak in the streamwise velocity variance and of the profile inside the logarithmic region already found in Figure 5.12.
Figure 5.20 show the value of the measured peak in the streamwise velocity versus R^+ for the current experiments, the experiments from Sattarzadeh (2011) and various DNS data. Figure 5.21 is the same of 5.20 but with the experimental data corrected with the scheme proposed by Smits *et al.* (2011*b*). Figure 5.22 and 5.23 show respectively the uncorrected and corrected local

turbulence intensity at $y^+ = 15$ for the same set data of Figure 5.20: a clear Reynolds number dependence can be notice for the spatial resolution corrected data. Figure 5.24 and 5.25 illustrate instead the maximum for the local turbulence intensity for uncorrected and corrected data respectively. The Reynolds number dependence here is not as clear as before, because this quantity reaches its maximum for a wall distance where the experimental results are already affected by the heat conduction towards the wall, which influence different probes in a different way.

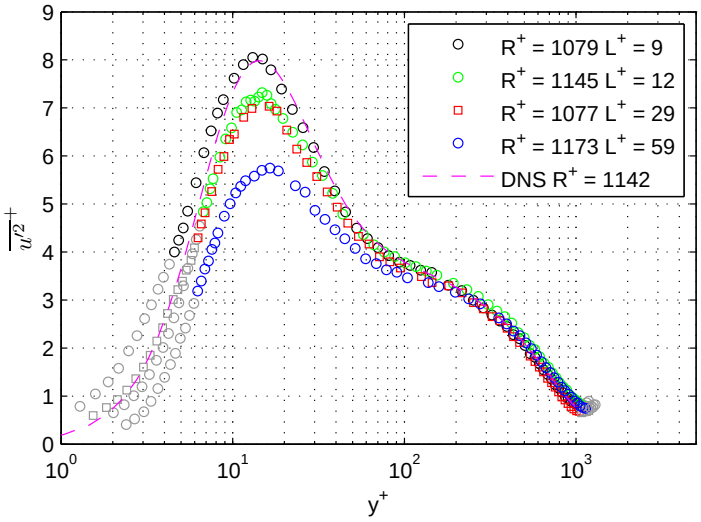

FIGURE 5.9. Streamwise velocity variance profiles for $R^+ \approx 1000$. *Magenta dashed line*: DNS data from Wu & Moin (2008).

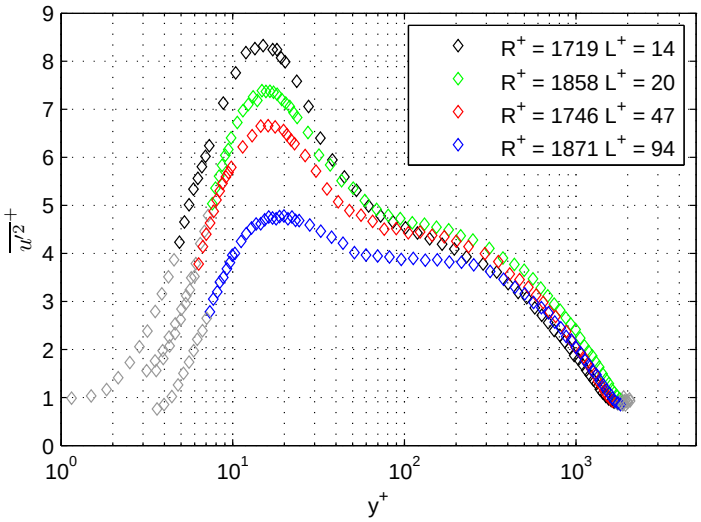

FIGURE 5.10. Streamwise velocity variance profiles for $R^+ \approx 1700$.

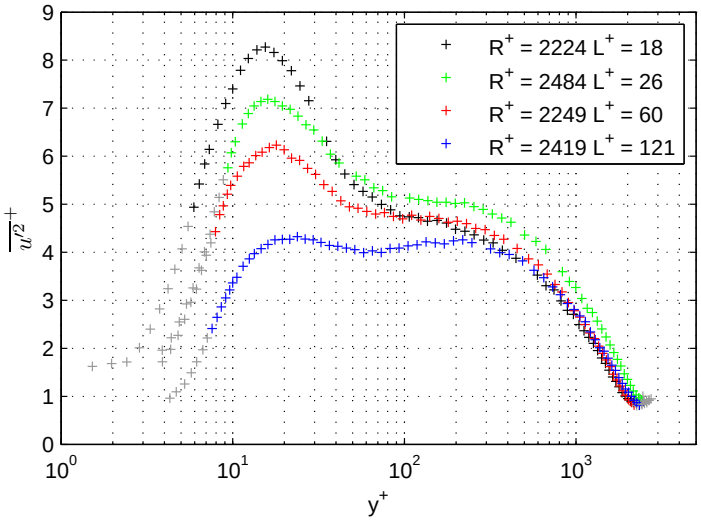

FIGURE 5.11. Streamwise velocity variance profiles for $R^+ \approx 2400$.

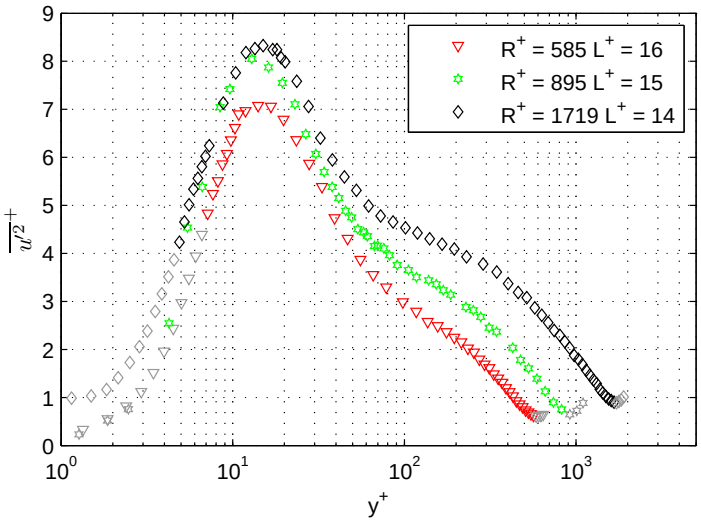

FIGURE 5.12. Streamwise velocity variance profiles for different R^+ and $L^+ \approx$ const. *Green hexagram*: experimental data from Sattarzadeh (2011); all other symbols: current measurements.

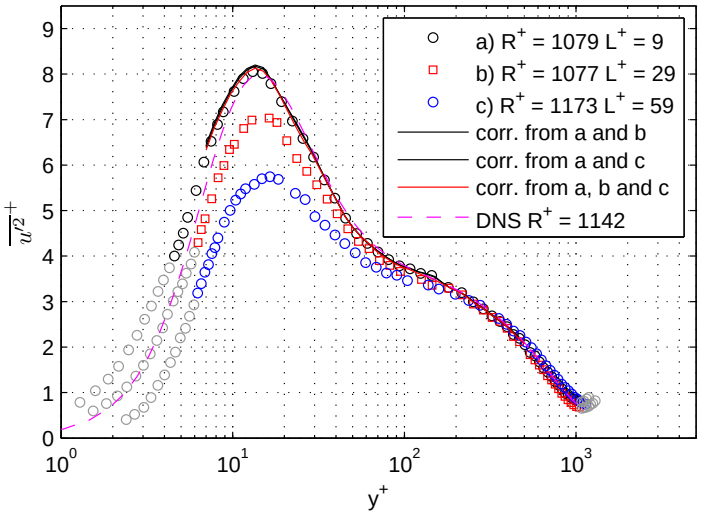

FIGURE 5.13. Streamwise velocity variance profiles for different $R^+ \approx 1000$ corrected as proposed by Segalini *et al.* (2011*b*).

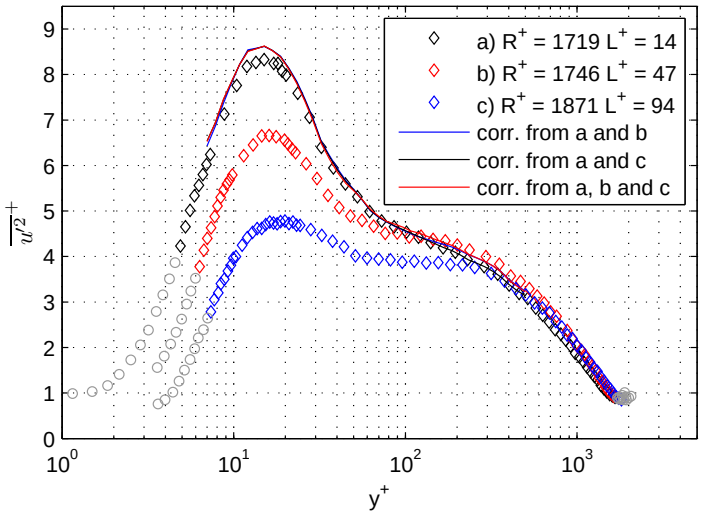

FIGURE 5.14. Streamwise velocity variance profiles for different $R^+ \approx 1700$ corrected as proposed by Segalini *et al.* (2011*b*).

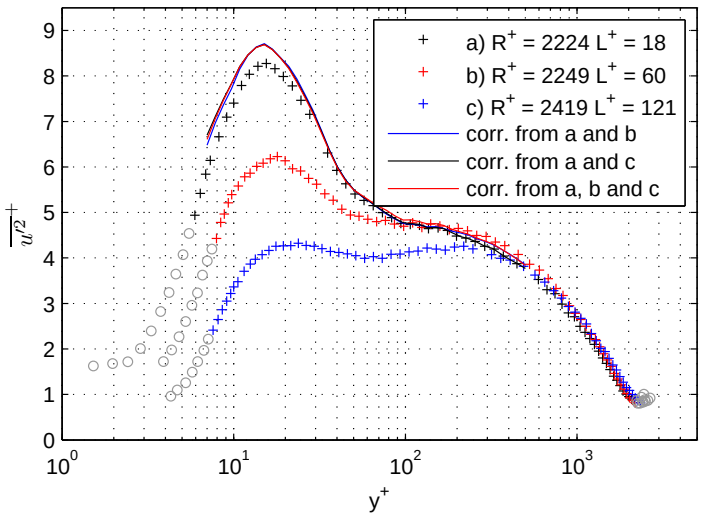

FIGURE 5.15. Streamwise velocity variance profiles for different $R^+ \approx 2400$ corrected as proposed by Segalini *et al.* (2011*b*).

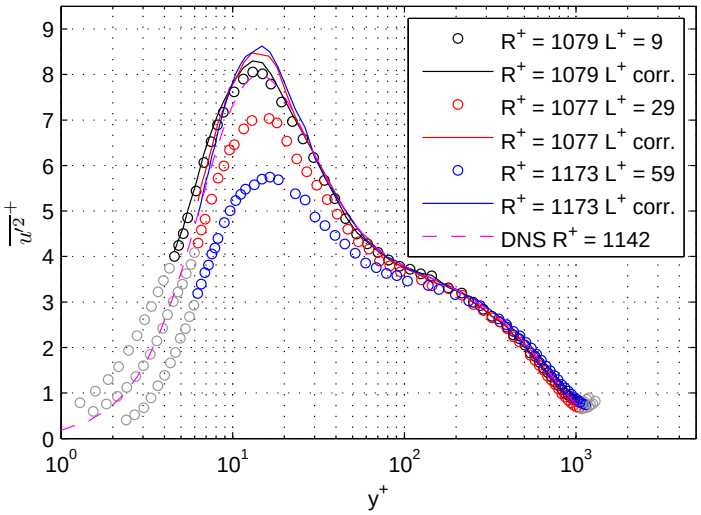

FIGURE 5.16. Streamwise velocity variance profiles for different $R^+ \approx 1000$ corrected as proposed by Smits *et al.* (2011*b*).

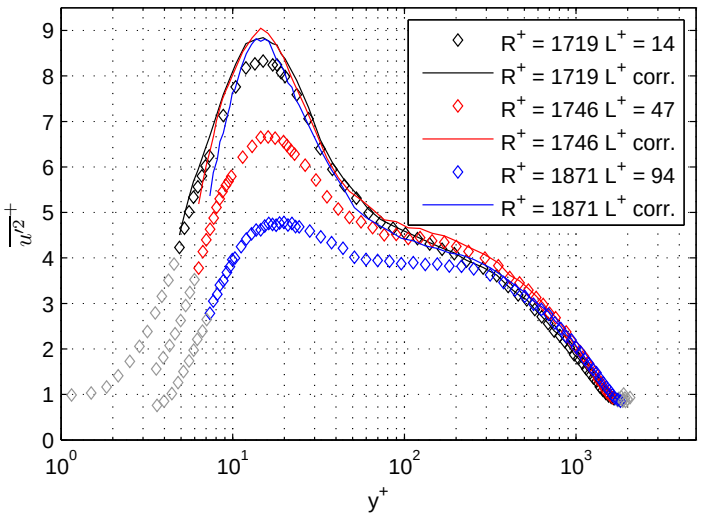

FIGURE 5.17. Streamwise velocity variance profiles for different $R^+ \approx 1700$ corrected as proposed by Smits *et al.* (2011*b*).

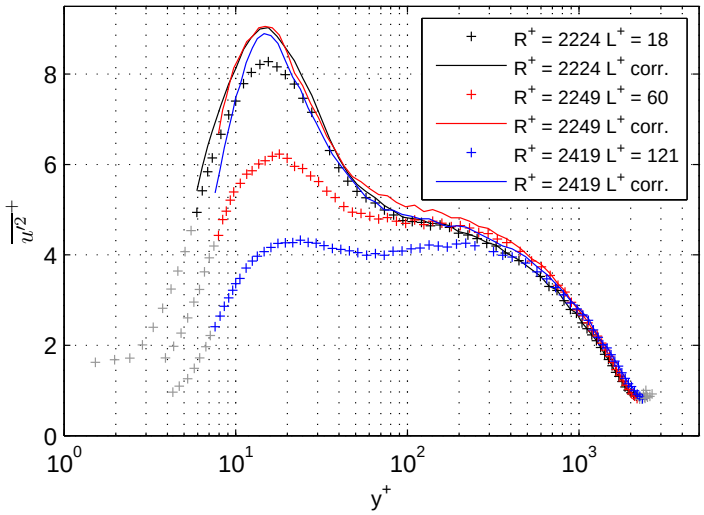

FIGURE 5.18. Streamwise velocity variance profiles for different $R^+ \approx 2400$ corrected as proposed by Smits *et al.* (2011*b*).

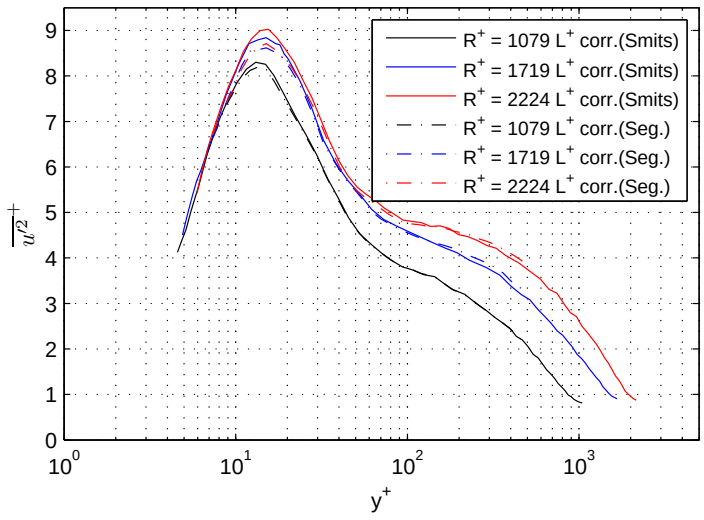

FIGURE 5.19. Comparison of the correction proposed by Smits *et al.* (2011*b*) (*solid lines*) and Segalini *et al.* (2011*b*) (*dashed lines*) for different R^+.

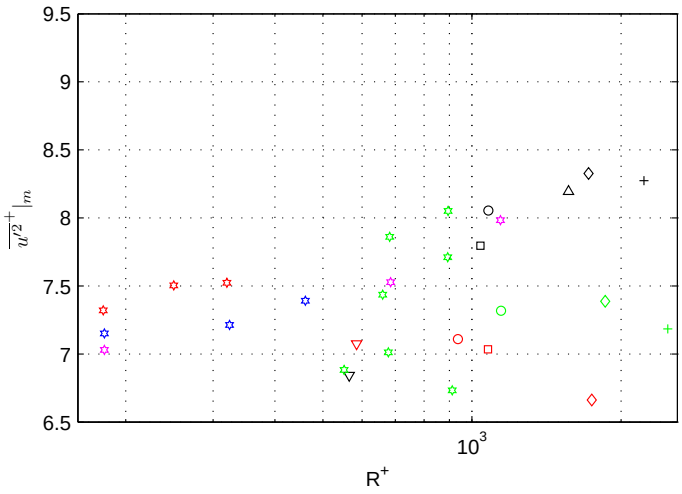

FIGURE 5.20. Peak of the Streamwise velocity variance profiles vs. R^+. *green hexagram*: uncorrected data from Sattarzadeh (2011); *blue hexagram*: DNS data from Veenman (2004); *red hexagram*: DNS data from Wagner *et al.* (2001); *magenta hexagram*: DNS data from Wu & Moin (2008); all the other symbols: current experiments (see Tab. 4.1).

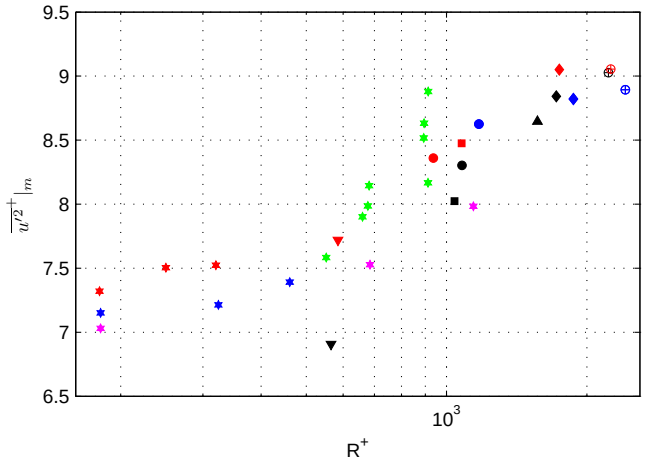

FIGURE 5.21. Peak of the Streamwise velocity variance profiles vs. R^+. Symbols as in Fig. 5.20. but with experimental data corrected as proposed by Smits *et al.* (2011*b*).

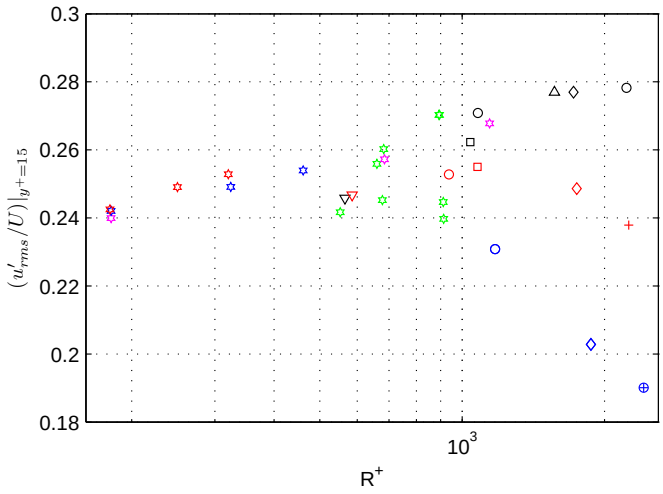

FIGURE 5.22. Local turbulence intensity for $y^+ = 15$ vs. R^+ for experimental and simulation data. Symbols as in Fig. 5.20.

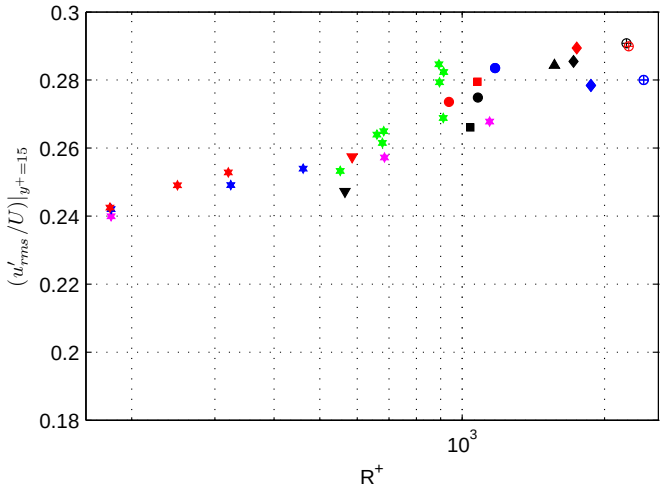

FIGURE 5.23. Local turbulence intensity for $y^+ = 15$ vs. R^+ for experimental and simulation data. Experimental data are corrected as proposed by Smits *et al.* (2011*b*), symbols as in Fig. 5.20.

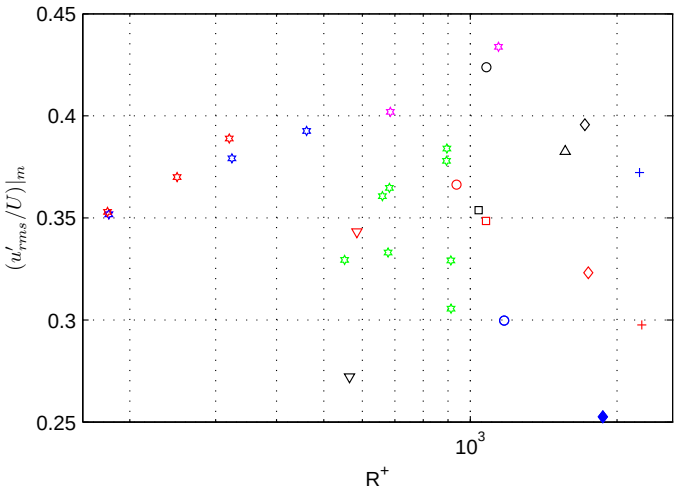

FIGURE 5.24. Maximum value of the local turbulence intensity vs. R^+ for experimental and simulation data. Symbols as in Fig. 5.20.

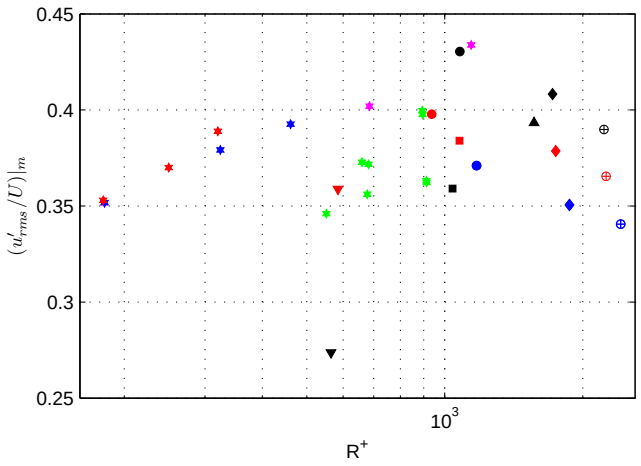

FIGURE 5.25. Maximum value of the local turbulence intensity vs. R^+ for experimental and simulation data. Experimental data are corrected as proposed by Smits *et al.* (2011*b*), symbols as in Fig. 5.20.

5.4. Turbulence intensity - Diagnostic plots

In Figure 5.26 the turbulence intensity profiles for the current experiments are shown in viscous unit. Figure 5.27 illustrates the diagnostic plot as introduced by Afredsson & Örlü (2010) for the current measurements and DNS data. Since in this way of representing the data neither the friction velocity nor the absolute position appear, the already cited difficulties in the determination of these two quantity can be neglected, leading to a rapresentation dependent just on the actual velocities measured. We notice how in the outer region all the data collapse on the same trend for all the Reynolds numbers, in accordance with to what stated in Afredsson & Örlü (2010). In order to observe the Reynolds number effect on the diagnostic plot not masked by spatial resolution issues, data taken at constant L^+ are shown in Figure 5.28.
In Figure 5.29 the turbulence intensity u_{rms}/U is plot against the mean velocity normalised with the centerline velocity U/U_{cl}, together with the linear fit for the outer region proposed in Alfredsson *et al.* (2012). The Reynolds number effect on this representation is more clear in Figure 5.30, where data with constant L^+ are considered. It appears clearly (even if higher Reynolds number separation would be useful), that for higher Reynolds number the data remain on the straight line until lower values of U/U_{cl}. In Alfredsson *et al.* (2011*b*) this behaviour was used to infer the existence of an "outer" (compared to $y^+ = 15$, but still in the logarithmic region) maximum of $\overline{u'^2}$.

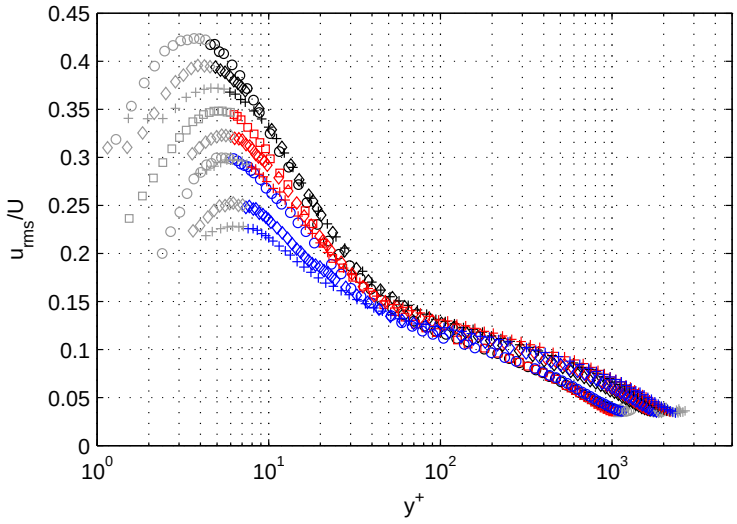

FIGURE 5.26. Turbulence intensity profiles for current experiments, data obtained with probe having $L/d < 160$ has been neglected. Symbols according to Tab. 4.1.

5.5. Higher order statistical moments

From Figure 5.4 to 5.7 the skewness profiles for measurements with approximately the same R^+ but different L^+ are compared: the spatial filtering effects are evident and can lead to an incorrect sign of the quantity and to mask the local minimum located around $y^+ \approx 30$. Profiles with same L^+ but different R^+ are shown in Figure 5.34.
The flatness profiles are shown in Figures from 5.35 to 5.37, grouped with the Reynolds number. Also in this case spatial resolution is critical for the correct individuation of the minimum of the flatness profiles. In Figure 5.38 profiles obtained with the same L^+ but different R^+ are compared.

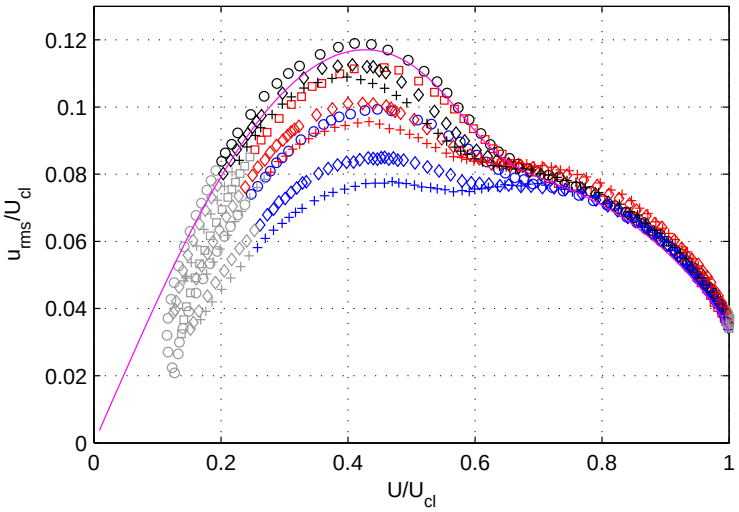

FIGURE 5.27. Diagnostic plot for the current measurements and DNS data. *Magenta line*: DNS data from Wu & Moin (2008); all other symbols: see Tab. 4.1.

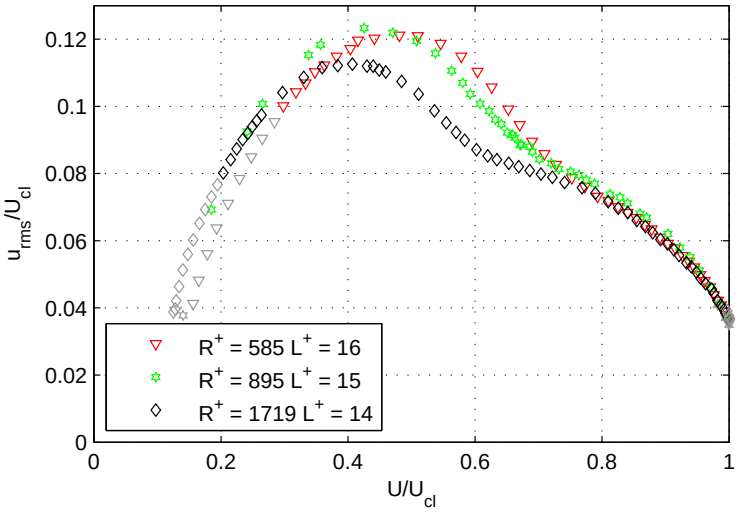

FIGURE 5.28. Diagnostic plot for measurements with $L^+ \approx$ const *Green hexagram*: experimental data Sattarzadeh (2011); all other symbols: current measurements.

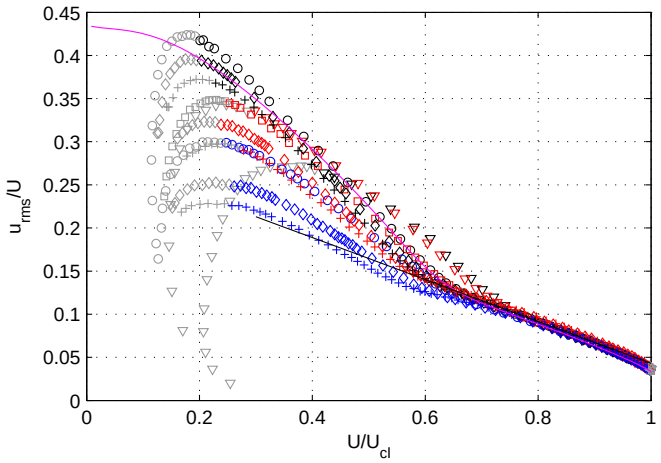

FIGURE 5.29. Diagnostic plot for the current measurements and DNS data. *Magenta line*: DNS data from Wu & Moin (2008); all other symbols: see Tab. 4.1; *Black line*: linear regression $\frac{u'}{U} = 0.286 - 0.243\frac{U}{U_{cl}}$.

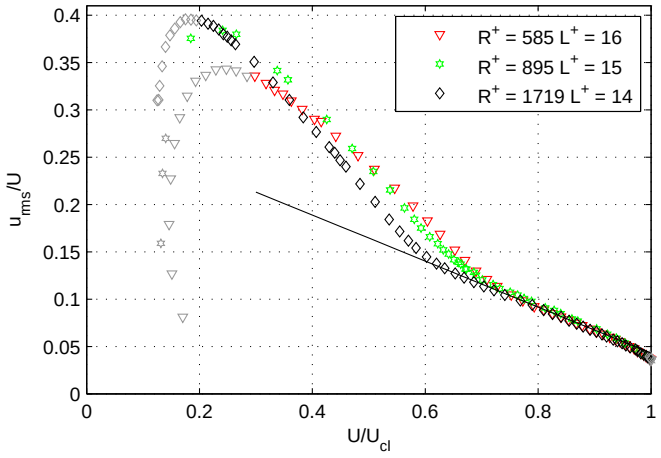

FIGURE 5.30. Modified diagnostic plot for measurements with $L^+ \approx$ const *Green hexagram*: experimental data Sattarzadeh (2011); all other symbols: current measurements; *Black line*: linear regression $\frac{u'}{U} = 0.286 - 0.243\frac{U}{U_{cl}}$.

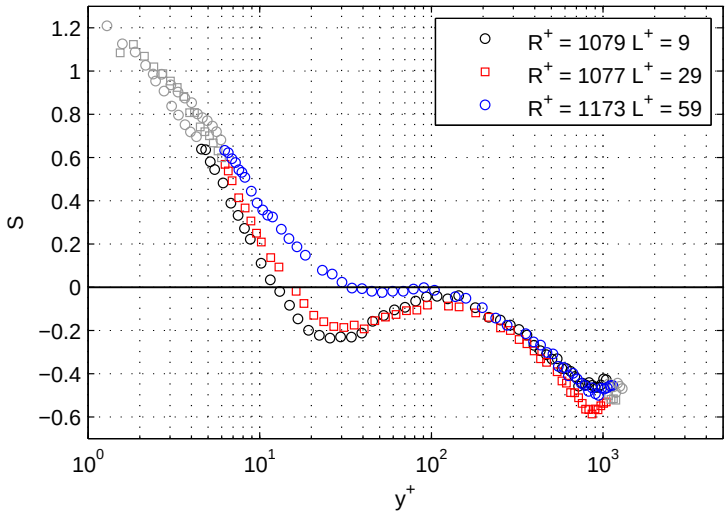

FIGURE 5.31. Velocity skewness profiles for $R^+ \approx 1000$.

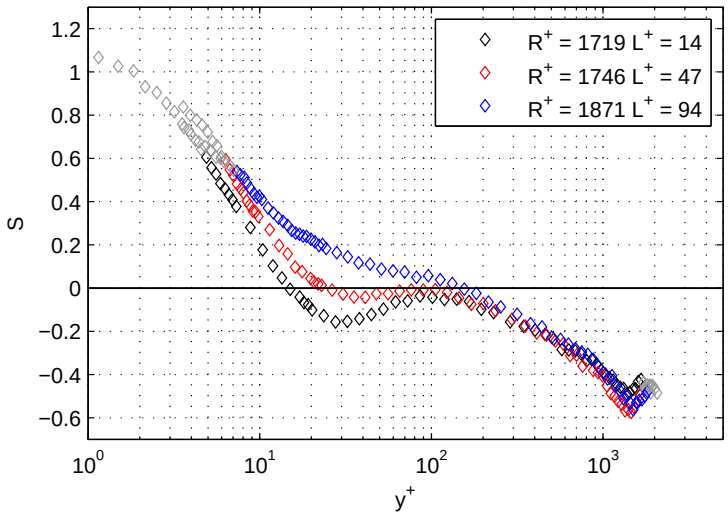

FIGURE 5.32. Velocity skewness profiles for $R^+ \approx 1700$.

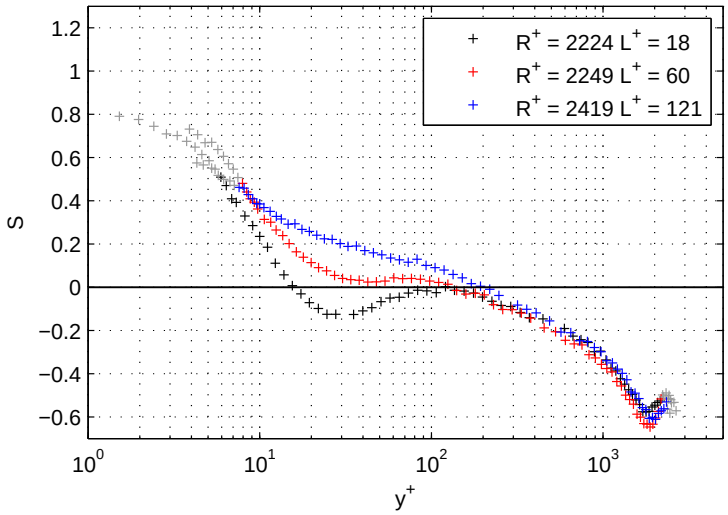

FIGURE 5.33. Velocity skewness profiles for $R^+ \approx 2400$.

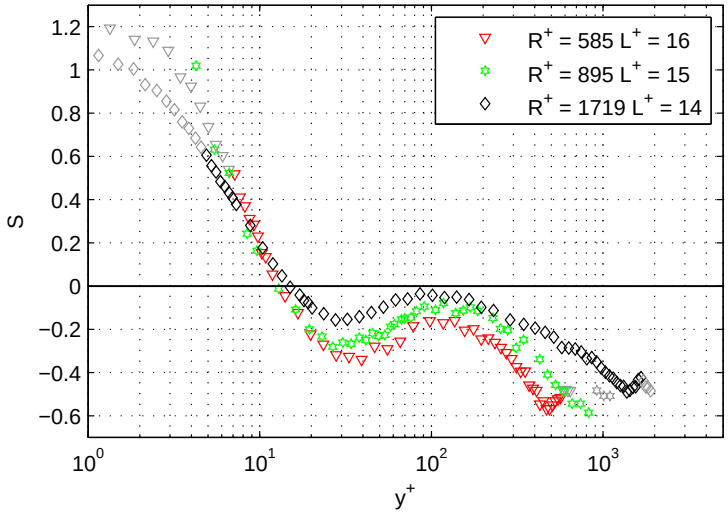

FIGURE 5.34. Velocity skewness profiles for different R^+ and $L^+ \approx$ const. *Green hexagram*: experimental data from Sattarzadeh (2011); all other symbols: current measurements.

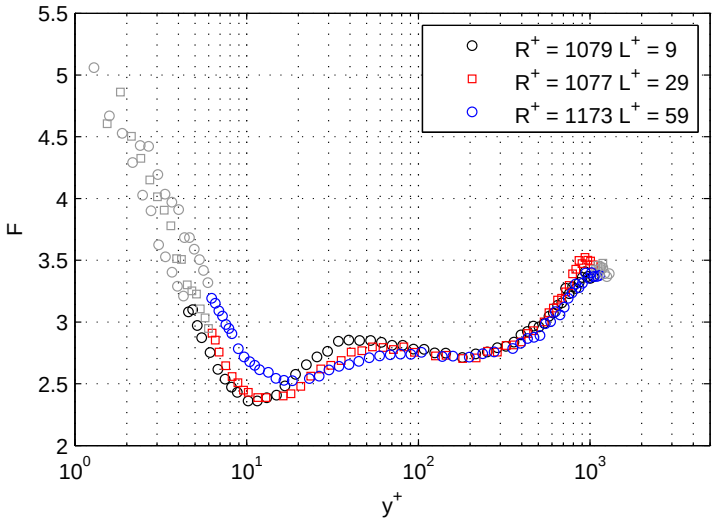

FIGURE 5.35. Velocity flatness profiles for $R^+ \approx 1000$.

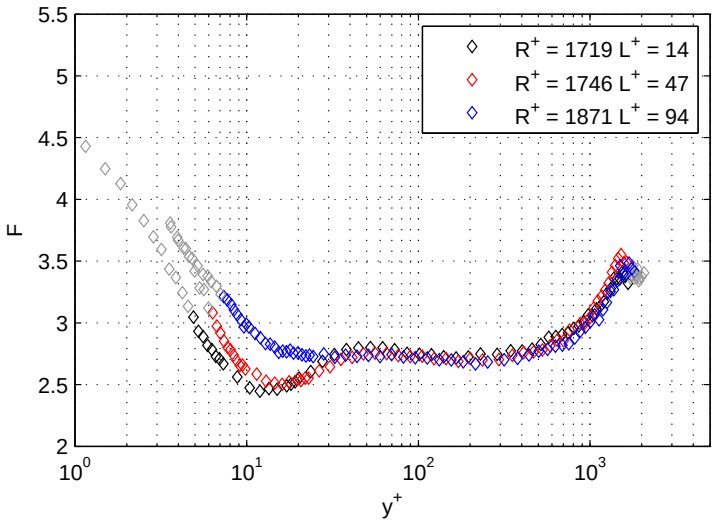

FIGURE 5.36. Velocity flatness profiles for $R^+ \approx 1700$.

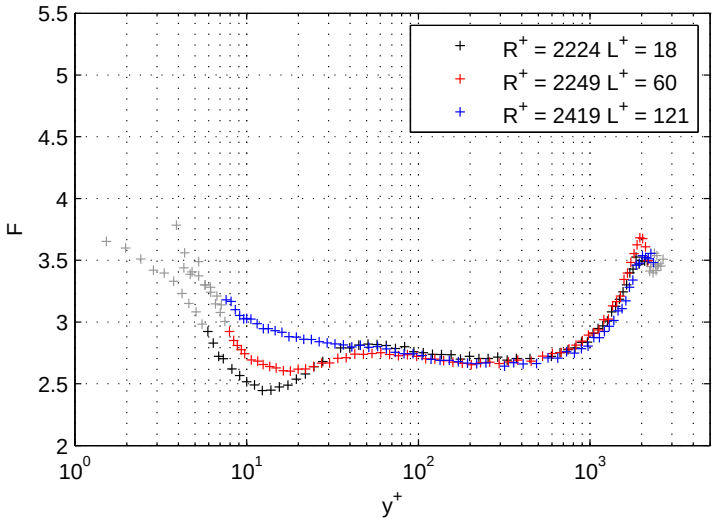

FIGURE 5.37. Velocity flatness profiles for $R^+ \approx 2400$.

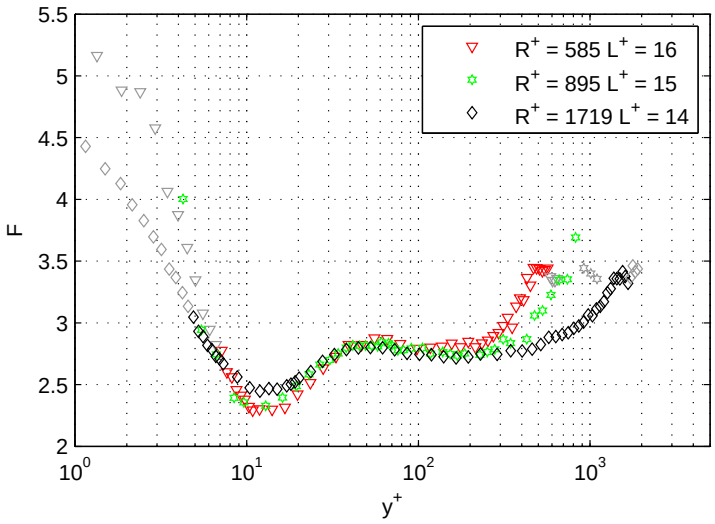

FIGURE 5.38. Velocity flatness profiles for different R^+ and $L^+ \approx$ const. *Green hexagram*: experimental data from Sattarzadeh (2011); all other symbols: current measurements.

5.6. Power spectra of streamwise velocity

In Figure 5.39 the one-dimensional pre-multiplied power spectral density map ($f^+P_{u^+u^+}$) of streamwise normalized velocity u^+ as a function of streamwise wavelenght (λ_x^+) and wall-normal position y^+ is presented for case A_6. The streamwise wavelengths were inferred from the time-series of velocity using the Taylor hypothesis (Taylor 1938) and the local mean velocity as the convective velocity of the waves. This representation is very common in literature, but the applicability of Taylor hypothesis to wall-bounded turbulence has been recently debated by Del Álamo & Jimnez (2009), who showed from simulation results that close to the wall the long wavelengths does not travel with the local mean velocity but with the bulk velocity; the scale separation of convection velocity was also observed by Chung & McKeon (2010). For this reason, in the figures following Figure 5.39 the spectra will be presented as a function of the normalized frequency f^+, which is related to what effectively measured using a fixed hot-wire probe. The results of Figure 5.39 are consistent with what commonly reported in literature for the same range of Reynolds number, with the main energy mode located at $y^+ \approx 15$ and $\lambda^+ \approx 1000$. This energy mode, clearly related to the inner peak in the velocity variance (cfr. Fig. 5.11), represents the energy contribution of the near-wall counter-rotating and elongated vortical structures first observed by Kline *et al.* (1967).
Figure 5.40 and 5.41 show the spatial resolution effect on the spectra: as for the streamwise velocity variance (cfr. Fig. 5.9) the attenuation is evident mainly in the near-wall region and lead to an underestimation of the inner peak intensity. Figure 5.42 show instead the Reynold number dependence of the spectra, showing cases with L^+ approximately constant, in order to minimize the influence of spatial resolution issues. A substantial similarity can be noticed in the near-wall region, but a higher intensity of the low-frequency energy modes can be noticed in the overlap region in the higher Reynolds number cases, with traces of an outer peak in Figure 5.42c. This outer peak is most likely related to the energy contribution of the Very Large Scale Motion (VLSM), first identified in pipe flow by Kim & Adrian (1999) and further investigated both for pipe and channel flow by Monty *et al.* (2007). The spectral peak separation is expected to appear for $R^+ \gtrsim 1700$ (see Hutchins & Marusic 2007), but a higher R^+ is required to distinguish properly the outer peak. Its location has been found by Mathis *et al.* (2009) to correspond well with the geometric centre of the logarithmic region (in the log-plot), they hence proposed $y^+ = 3.9\sqrt{R^+}$ as the outer peak's position. Figure 5.43 show premultiplied power spectra at selected y^+ position for the same cases showed in Figure 5.42. Wall normal position of $y^+ \approx 15$, 50, $3.9\sqrt{R^+}$ were chosen because they are respectively the location of the inner peak, of the conventional start of the outer layer and of the outer peak. In order to maintain the uniformity in the figure the position $y^+ = 3.9\sqrt{R^+}$ was chosen even when data obtained at $R^+ = 585$ were concerned, even if in this case the definition of a log-region, and hence of its geometric

midpoint, can be objected because of the low Reynolds number. We can notice how the energy content of the low frequency modes increase at all the wall-normal positions with the increase of the Reynolds number, while the value of the peak of the premultiplied spectra is constant with the Reynolds number, in accordance with the experiments by Ng *et al.* (2011). For $R^+ = 585$ (Fig. 5.43a), the energy signature of the near wall cycle dominates at all the location plotted, while in $R^+ = 2224$ (Fig. 5.43c) the maximum of the energy spectra at $y^+ = 3.9\sqrt{R^+}$ is reached for a low-frequency mode. This peak is located at $f^+ \approx 10^{-3}$, and is likely related to the VLSM: since in literature VLSM are reported to scale in outer variables, it is better to express this value as $fR/U_{cl} \approx 0.027$.

With the aid of the premultiplied power spectra it is possible to explain the velocity variance growth with the Reynolds number at the inner peak location and in the logarithmic region (cfr. Fig. 5.12, 5.19 and 5.21). In fact, from eq. (2.27) we have:

$$\int_0^{+\infty} P_{uu}(f)\,\mathrm{d}f = \overline{u'^2}\,, \tag{5.10}$$

which can be written as

$$\int_0^{+\infty} P_{u^+u^+}\nu\,\mathrm{d}\left(\frac{f^+u_\tau^2}{\nu}\right) = \overline{u'^2} \tag{5.11}$$

and finally

$$\ln 10 \int_0^{+\infty} f^+ P_{u^+u^+}\,\mathrm{d}(\log f^+) = \frac{\overline{u'^2}}{u_\tau^2} = \overline{u'^2}^+\,. \tag{5.12}$$

The area under the premultiplied u spectra is hence proportional to the streamwise velocity variance. From Figure 5.43 appears clearly that the increase of the energy content of the low-frequency modes is responsible of the increase of the peak in the streamwise velocity variance and throughout the logarithmic region.

Figure 5.44 presents the velocity power-spectra in log-log style for the same cases and wall-normal position of Figure 5.43.

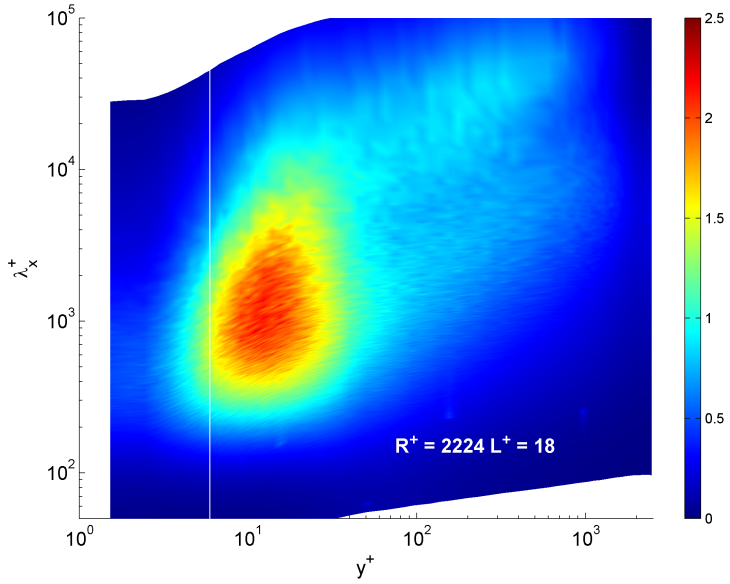

FIGURE 5.39. Premultiplied u power-spectra map vs. streamwise wavelength λ^+ estimated using the mean velocity. The data at the left of the white solid line were considered affected by additional heat transfer.

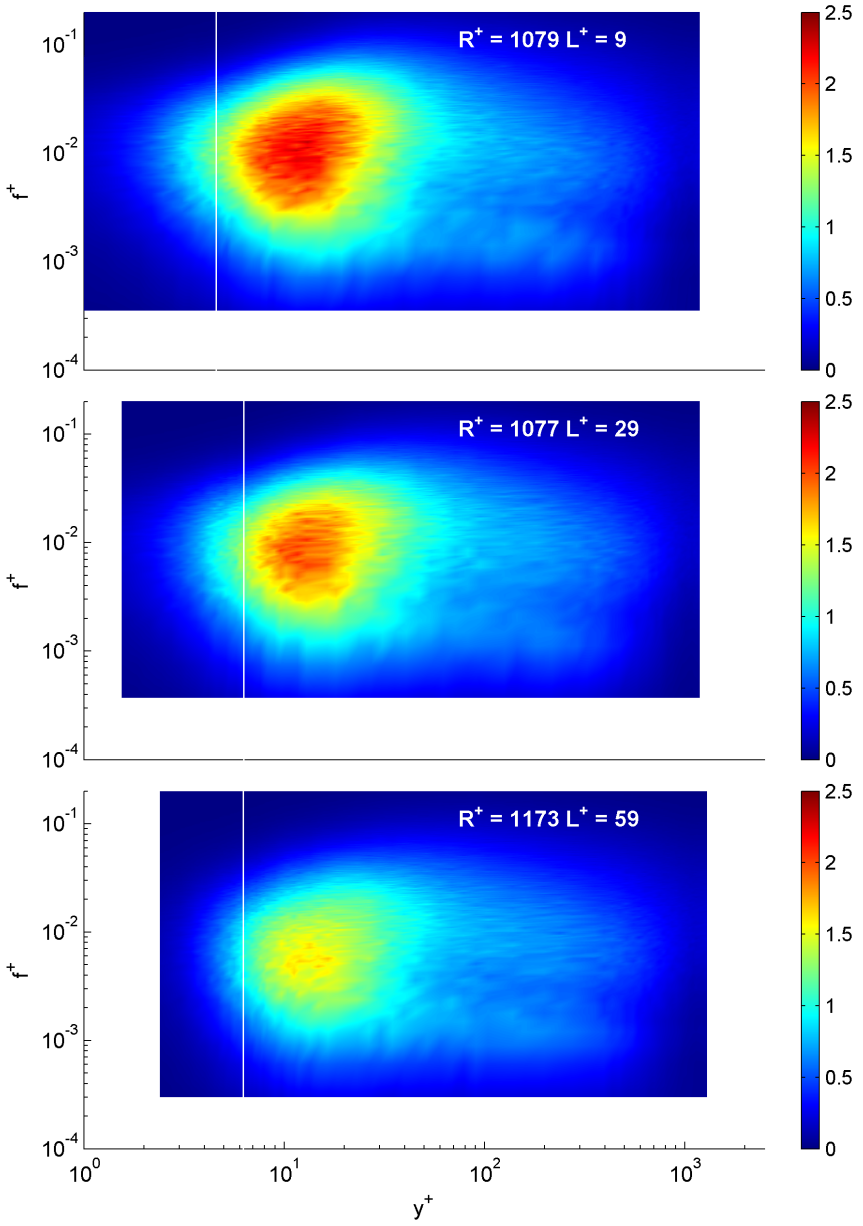

FIGURE 5.40. Premultiplied u power-spectra map for $R^+ \approx 1000$ but different L^+. The data at the left of the white solid line were considered affected by additional heat transfer.

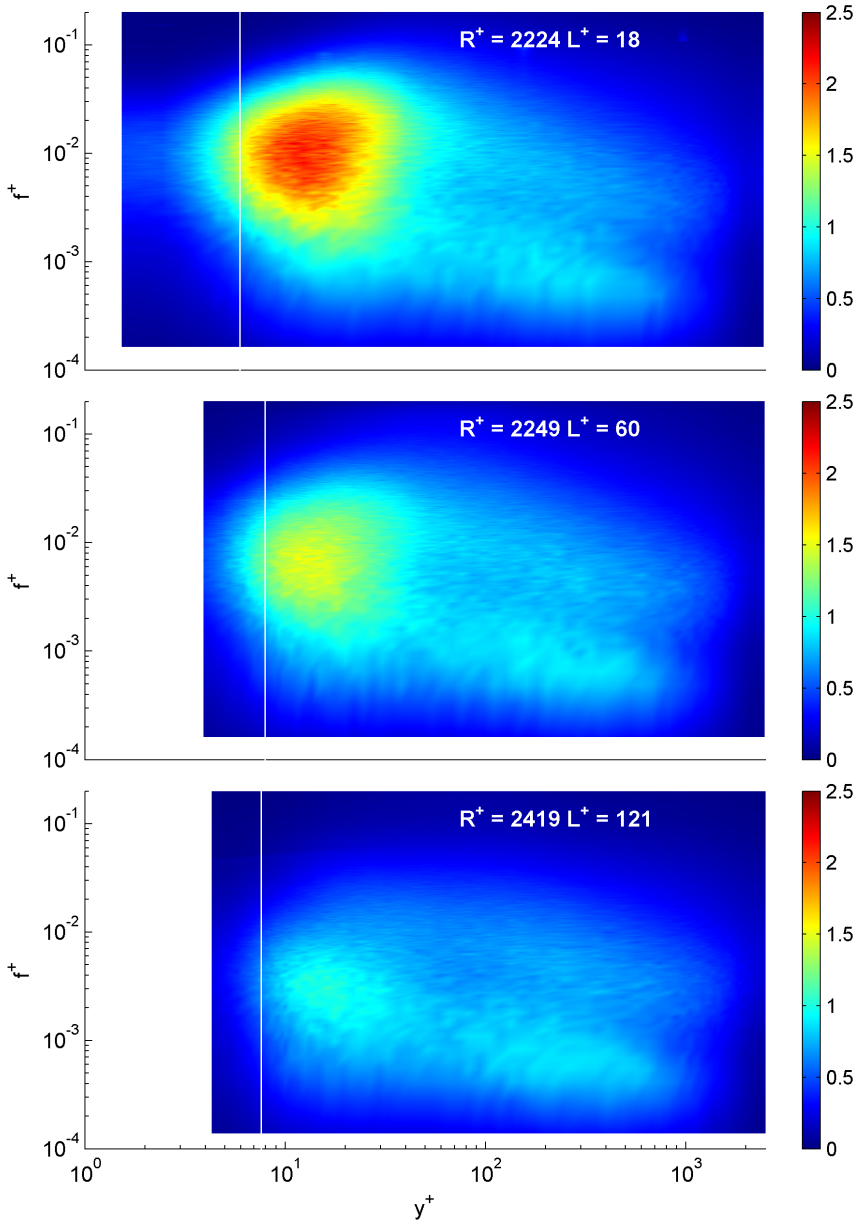

FIGURE 5.41. Premultiplied u power-spectra map for $R^+ \approx 2400$ but different L^+. The data at the left of the white solid line were considered affected by additional heat transfer.

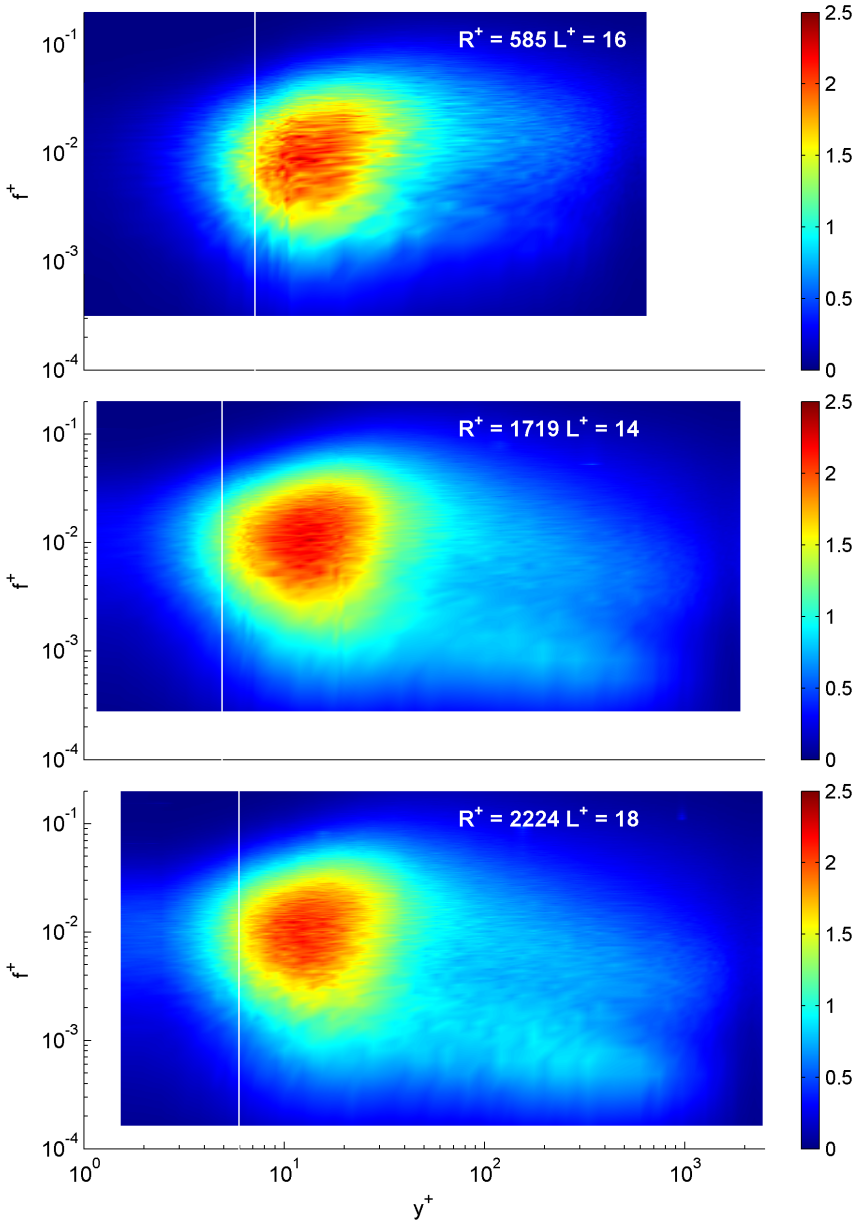

FIGURE 5.42. Premultiplied u power-spectra map for different R^+ and $L^* \approx$ const. The data at the left of the white solid line were considered affected by additional heat transfer.

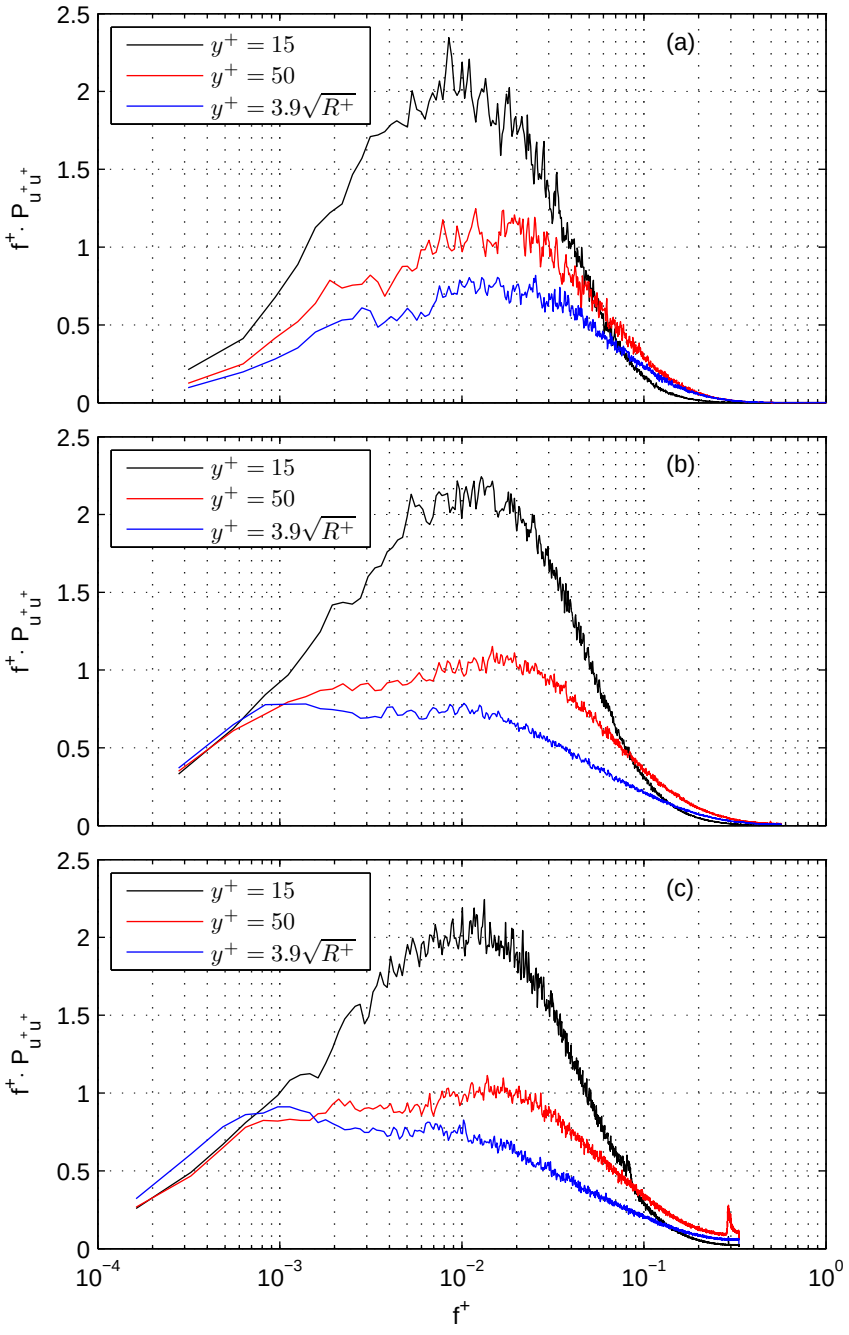

FIGURE 5.43. Line plots of premultiplied u power-spectra at different wall normal locations. **a**: $R^+ = 585$ $L^+ = 16$; **b**: $R^+ = 1719$ $L^+ = 14$; **c**: $R^+ = 2224$ $L^+ = 18$;

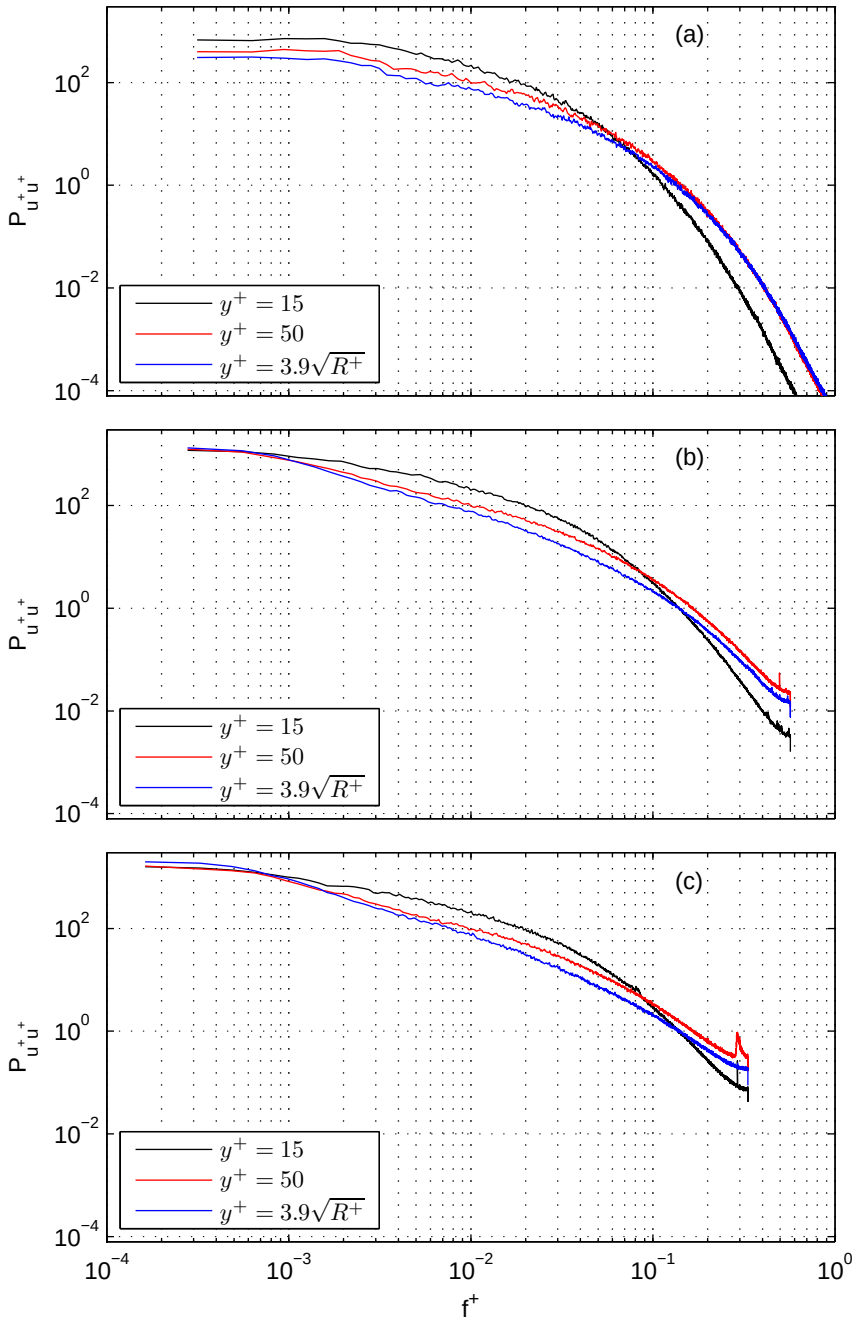

FIGURE 5.44. Line plots of u power-spectra at different wall normal locations. **a**: R^+ = 585 L^+ = 16; **b**: R^+ = 1719 L^+ = 14; **c**: R^+ = 2224 L^+ = 18;

5.7. Cumulative distribution function (CDF)

In Figure 5.45 and 5.46 the CDF contour of streamwise velocity u are shown for measurements with approximately the same R^+, but different L^+. We notice that for higher L^+ the CDF contour are more narrow and this is especially evident in the extrema of the PDF. Figure 5.47 illustrates instead the R^+ dependence of the CDF contour for measurements with approximately the same L^+.

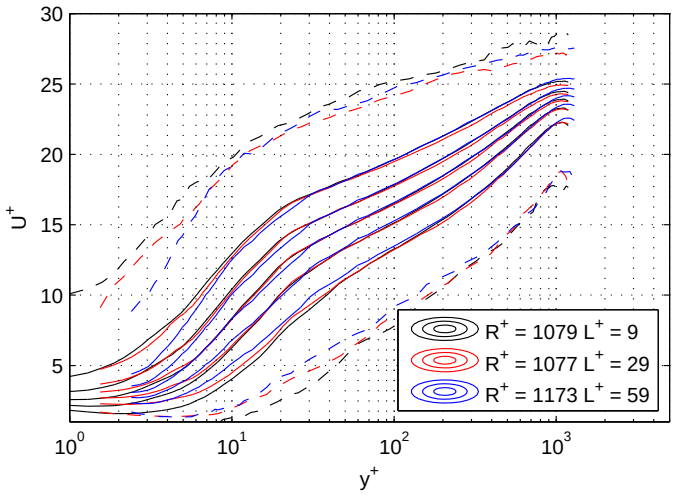

FIGURE 5.45. CDF contour for $R^+ \approx 1000$ and different L^+. *Dashed line*: extrema of the CDF (i.e. maximum and minimum of $u(t)$); *solid line*: CDF contour for $F(u) = [0.05\,;0.25\,;0.5\,;0.75\,;0.95]$

5.8. Integral timescale profiles

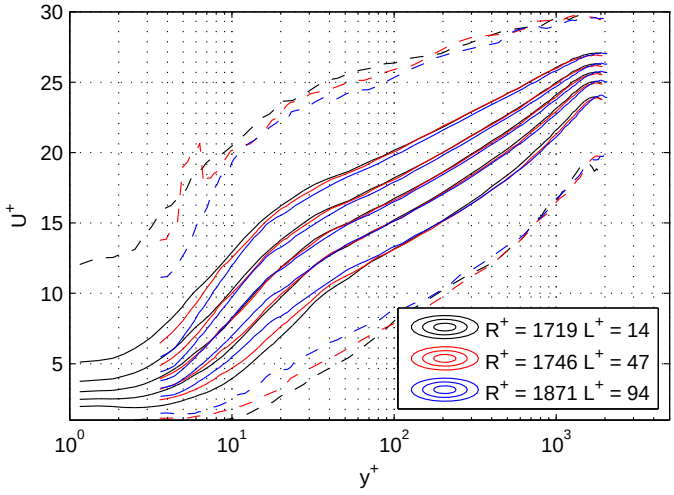

FIGURE 5.46. CDF contour for $R^+ \approx 1700$ and different L^+. *Dashed line*: extrema of the CDF (i.e. maximum and minimum of $u(t)$); *solid line*: CDF contour for $F(u) = [0.05\,;0.25\,;0.5\,;0.75\,;0.95]$

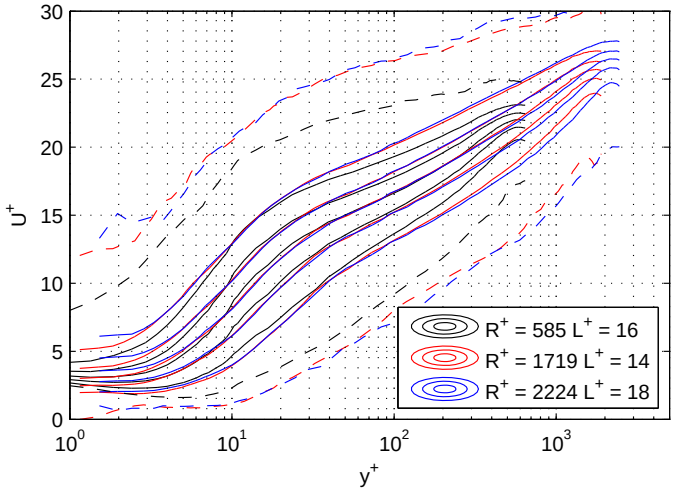

FIGURE 5.47. CDF contour for different R^+ and $L^+ \approx const.$ *Dashed line*: extrema of the CDF (i.e. maximum and minimum of $u(t)$); *solid line*: CDF contour for $F(u) = [0.05\,;0.25\,;0.5\,;0.75\,;0.95]$

5.9. Temperature profiles

The temperature profiles at three different R^+ were acquired with a cold-wire probe, with the main purpose of providing the data necessary to correct the hot-wire signal (see §4.2). For each temperature measurements, the centerline velocity was also measured with a hot-wire probe, in order to obtain R^+ (and thus ℓ_*) from a linear fit similar to the one showed in Figure 5.1, but with a Reynolds number based on the centerline velocity instead of the bulk velocity. The experimental condition are reported in Table 5.1, where the notations are the same used in Table 4.1.

Case	U_{cl} (m/s)	R^+	ℓ_* (μm)	probe	fan	L^+	$\Delta t^{+\,(*)}$	TU_{cl}/R
T_1	15.16	1 167	26	D	b	58	12	15 200
T_2	25.17	1 821	16	D	b	91	31	25 200
T_3	35.64	2 453	12	D	b	123	56	35 600

TABLE 5.1. Experimental parameters for present cold-wire experiments. Same notations of Tab. 4.1.
$^{(*)}$ The sampling period is based on the actual sampling frequency f = 2kHz, but a low-pass filter set at f = 1kHz was used.

Figure 5.48 illustrates the profile of the dimensionless temperature Θ, defined as

$$\Theta = \frac{\overline{T} - T_{min}}{\overline{T_{cl}} - T_{min}} \,, \tag{5.13}$$

where T_{min} is the lowest temperature measured with the cold-wire probe (approximately equal to the wall temperature). In Figure 5.49 the dimensionless temperature variance

$$\overline{\Theta'^2} = \frac{\overline{T'^2}}{(\overline{T_{cl}} - T_{min})^2} \tag{5.14}$$

is plotted against y^+. In the Figure L^+ and R^+ effects coexist, but the spatial resolution effects is much more evident, as can be deduced from the reduction of the temperature variance.

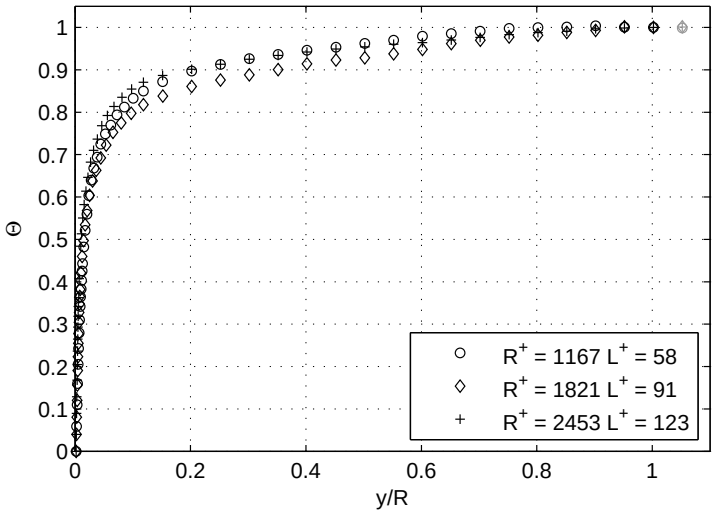

FIGURE 5.48. Distribution of Θ vs. y/R.

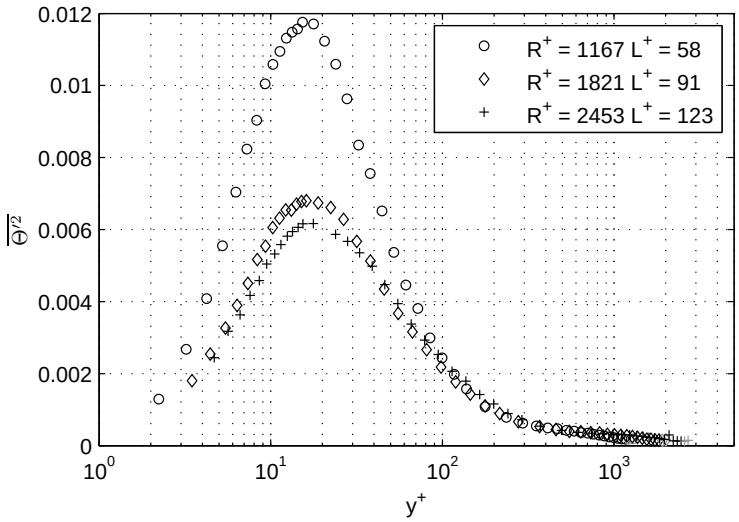

FIGURE 5.49. Distribution of Θ' vs. y^+.

CHAPTER 6

Summary and Conclusions

References

Afredsson, P. H. & Örlü, R. 2010 The diagnostic plot - a litmus test for wall bounded turbulence data. *Eur. J. Mech. B-Fluid* **29**, 403–406.

Alfredsson, P. H., Johansson, A. V., Haritonidis, J. H. & Eckelmann, H. 1988 The fluctuating wall-shear stress and the velocity field in the viscous sublayer. *Phys. Fluids* **31**, 1026–1033.

Alfredsson, P. H., Örlü, R. & Schlatter, P. 2011*a* The viscous sublayer revisitedexploiting self-similarity to determine the wall position and friction velocity. *Exp. Fluids* **51**, 271–280.

Alfredsson, P. H., Örlü, R. & Segalini, A. 2012 A new formulation for the streamwise turbulence intensity distribution in wall-bounded turbulent flows. *Eur. J. Mech. B-Fluid* **In Press**, doi:10.1016/j.euromechflu.2012.03.015.

Alfredsson, P. H., Segalini, A. & Örlü, R. 2011*b* A new scaling for the streamwise turbulence intensity in wall-bounded turbulent flows and what it tells us about the outer peak. *Phys. Fluids* **23**, 041702.

Alfredsson, P. H. & Tillmark, N. 2005 A beginners guide to fluid mechanics measurements. Book manuscript.

Bhatia, J. C., Durst, F. & Jovanovic, J. 1982 Corrections of hot-wire anemometer measurements near walls. *J. Fluid Mech.* **122**, 411–431.

Blackwelder, R. F. & Haritonidis, J. H. 1983 Scaling of the bursting frequency in turbulent boundary layers. *J. Fluid Mech.* **132**, 87–103.

Bradbury, L. J. S. & Castro, I. 1972 Some comments on heat-transfer laws for fine wires. *J. Fluid Mech.* **51**, 487–495.

Bruun, H. H. 1995 *Hot-Wire Anemometry: Principles and Signal Analysis*. Oxford University Press.

Chin, C. C., Hutchins, N., Ooi, A. S. & Marusic, I. 2009 Use of direct numerical simulation (dns) data to investigate spatial resolution issues in measurements of wall-bounded turbulence. *Meas. Sci. Technol.* **20**, 115401.

Chung, D. & McKeon, B. 2010 Large-eddy simulation of large-scale structures in long channel flow. *J. Fluid Mech.* **661**, 341–364.

Colebrook, C. F. 1939 Turbulent flow in pipes, with particular reference to the transition region between smooth and rough pipe laws. *Journ. ICE* **11**, 133–156.

Coles, D. 1956 The law of the wake in the turbulent boundary layer. *J. Fluid Mech.* **1**, 191–226.

DeGraaff, D. B. & Eaton, J. K. 2000 Reynolds-number scaling of the flat-plate turbulent boundary layer. *J. Fluid Mech.* **422**, 319–346.

Del Álamo, J. & Jimnez, J. 2009 Estimation of turbulent convection velocities and corrections to taylors approximation. *J. Fluid Mech.* **640**, 5–26.

Dénos, R. & Sieverding, C. H. 1997 Assessment of the cold-wire resistance thermometer for high-speed turbomachinery applications. *J. Turbomach.* **119**, 140–148.

van Dijk, A. & Nieuwstadt, F. T. M. 2004 The calibration of (multi-) hot-wire probes. 1. temperature calibration. *Exp. Fluids* **36**, 540–549.

Doherty, J., Ngan, P., Monty, J. P. & Chong, M. S. 2007 Proceedings of the 16th australasian fluid mechanics conference.

Dryden, H. L., Shubauer, G. B., C:, M. W. & Skramstad, H. K. 1937 Report n 581 - measurements of intensity and scale of wind-tunnel turbulence and their relation to the critical reynolds number of spheres. *Tech. Rep.*. NACA.

Facciolo, L. 2006 A study on axially rotating pipe and swirling jet flows. PhD thesis, KTH Mechanics, Stockholm, Sweden, TRITA-MEK Tech. Rep. 2006:02.

Fingerson, L. & Freymuth, P. 1996 *Fluid Mechanics Measurements, 2nd ed., Goldstein, R. J. (Ed.)*, chap. Thermal anemometer., pp. 115–173. Taylor & Francis.

George, W. K., Beuther, P. D. & A., S. 1989 Polynomial calibrations for hot wires in thermally varying flows. *Exp. Therm. Fluid. Sci.* **2**, 230–235.

van der Hegge Zijnen, B. G. 1951 On the construction of hot-wire anemometers for the investigation of turbulence. *Appl. Sci. Res.* **2**, 351–363.

Hultmark, M., Ashok, A. & Smits, A. J. 2011 A new criterion for end-conduction effects in hot-wire anemometry. *Meas. Sci. Technol.* **22**, 055401.

Hultmark, M., Bailey, S. C. C. & Smits, A. J. 2010 Scaling of near-wall turbulence intensity. *J. Fluid Mech.* **649**, 103–113.

Hutchins, N. & Marusic, I. 2007 Large-scale influences in near-wall turbulence. *Phil. Trans. R. Soc. A* **365**, 647–664.

Jimnez, J. & Hoyas, S. 2008 Turbulent fluctuations above the buffer layer of wall-bounded turbulence. *J. Fluid Mech.* **635**, 103–136.

Johansson, A. V. & Alfredsson, P. H. 1982 On the structure of turbulent channel flow. *J. Fluid Mech.* **122**, 295–314.

von Kármán, T. 1930 Mechanische Ähnlichkeit und turbulenz. In *Proc. Third Int. Congr. Applied Mechanics, Stockholm, pp. 85-105*.

Kim, K. & Adrian, R. 1999 Very large-scale motion in the outer layer. *Phys. Fluids* **11**, 417–422.

King, L. V. 1914 On the convection of heat from small cylinders in a stream of fluid: Determination of the convection constants of small platinum wires, with applications to hot-wire anemometry. *Proc. R. Soc. A* **90**, 563–570.

Klewicki, J. C. & Falco, R. E. 1990 On accurately measuring statistics assciated with small-scale structure in turbulent boundary layers using hot-wire probes. *J. Fluid Mech.* **219**, 119–142.

Kline, S., Reynolds, W., Shrub, F. & Rundstadler, P. 1967 The structure of turbulent boundary layers. *J. Fluid Mech.* **30**, 741–773.

Kolmogorov, A. N. 1941 The local structure of turbulence in incompressible viscous fluid for very large reynolds numers. (eng. trans. in proc. r. soc. a 434, 9-13). *Dokl. Akad. Nauk SSSR [in Russian].* **32**, 19–21.

Kundu, P. K. & Cohen, I. M. 2007 *Fluid Mechanics, Fourth Edition*. Academic Press.

Künn, W. & Dressler, B. 1985 Experimental investigations on the dynamic behaviour of hot-wire probes. *J. Phys.: E Sci. Instrum.* **18**, 614–622.

Lange, C. F., Durst, F. & Breuer, M. 1999 Wall effects on heat losses from hot-wires. *Int J Heat Fluid Fl* **20**, 34–47.

Lingrani, P. M. & Bradshaw, P. 1987*a* Spatial resolution and measurement of turbulence in the viscous sublayer using subminiature hot-wire probes. *Exp. Fluids* **5**, 407–417.

Lingrani, P. M. & Bradshaw, P. 1987*b* Subminiature hot-wire sensors: development and use. *J. Phys. E Sci. Instrum.* **20**, 323–332.

Lomas, C. G. 1985 *Fundamentals of Hot Wire Anemometry*. Cambridge University Press.

Lord, R. G. 1981 The dynamic behaviour of hot-wire anemometers with conduction end losses. *J. Phys.: E Sci. Instrum.* **14**, 573–578.

Marusic, I., Mathis, R. & Hutchins, N. 2010*a* High reynolds number effects in wall turbulence. *Int J Heat Fluid Fl.* **31**, 418–428.

Marusic, I., McKeon, B., Monkewitz, P. A., Nagib, H. & Smits, A. J. 2010*b* Wall-bounded turbulent flows at high reynolds numbers: recent advances and key issues. *Phys. Fluids* **22**, 065103.

Mathis, R., Hutchins, N. & Marusic, I. 2009 Large-scale amplitude modulation of the small-scale structures in turbulent boundary layers. *J. Fluid Mech.* **628**, 311–337.

McKeon, B., Li, J. D., Jiang, W., Morrison, J. F. & Smits, A. J. 2004 Further observations on the mean velocity distribution in fully developed pipe flow. *J. Fluid Mech.* **501**, 135–147.

Metzger, M. M. & Klewicki, J. C. 2001 A comparative study of near-wall turbulence in high and low reynolds number boundary layers. *Phys. Fluids* **13**, 692–701.

Millikan, C. B. 1938 A critical discussion of turbulent flows in channels and circular tubes. In *Proc. 5th Int. Congr. Applied Mechanics, New York, pp.386-392*.

Millon, F., Parantheon, P. & Trinite, M. 1978 Influence des eschanges thermiques entre le capteur et ses supports sur le mesure des fluctuations de temperature dans un ecoulement turbulent. *Int J Heat Mass Transfer.* **21**, 1–6.

Monty, J. P. 2005 Developments in smooth wall turbulent duct flows. PhD thesis, University of Melbourne, Australia.

Monty, J. P., Stewart, J. A., C., W. R. & Chong, M. S. 2007 Large-scale features in turbulent pipe and channel flows. *J. Fluid Mech.* **589**, 147–156.

Moody, L. F. 1944 Friction factors for pipe flow. *Trans. ASME* **66**, 671–684.

Musker, A. J. 1979 Explicit expression for the smooth wall velocity distribution in a turbulent boundary layer. *AIAA J.* **17**, 655–657.

Nagib, H. M. & Chauhan, K. A. 2008 Variations of von kármán coefficient in canonical flows. *Phys. Fluids* **20**, 101518.

Nagib, H. M., Chauhan, K. A. & Monkewitz, P. A. 2007 Approach to an asymptotic state for zero pressure gradient turbulent boundary layers. *Phil. Trans. R. Soc. A* **365**, 755–770.

Nagib, H. M., Christophorou, C., Rüedi, J.-D., Monkewitz, P. A. & Österlund, J. M. 2004 Can we ever rely on results from wall-bounded turbulent flows without direct measurements of wall shear stress? In *AIAA 2004-2392*.

Ng, H. C. H., Monty, J., Hutchins, N., Chong, M. S. & Marusic, I. 2011 Comparison of turbulent channel and pipe flows with varying reynolds number. *Exp. Fluids* **51**, 1261–1281.

Nikuradse, J. 1933 Strömungsgesetze in rauhen rohren. (eng. trans. in: Laws of flow in rough pipes, naca tm-1292 [1950]). *VDI-Forschungsheft* **361**.

Örlü, R. 2009 Experimental studies in jet flows and zero pressure-gradient turbulent boundary layers. PhD thesis, KTH Mechanics, Stockholm, Sweden.

Örlü, R., Fransson, J. H. M. & Alfredsson, P. H. 2010 On near wall measurements of wall bounded flows - the necessity of an accurate determination of the wall position. *Prog. Aerosp. Sci.* **46**, 353–387.

Österlund, J. M. 1999 Experimental studies of zero pressure-gradient turbulent boundary layer flow. PhD thesis, KTH Mechanics, Stockholm, Sweden.

Österlund, J. M., Johansson, A. V., Nagib, H. M. & Hites, M. H. 2000 A note on the overlap region in turbulent boundary layers. *Phys. Fluids* **12**, 1–4.

Parantheon, P., Petit, C. & Lecordier, J. C. 1982 The effect of the thermal prong-wire interaction on the response of a cold wire in gaseous flows (air, argon and helium). *J. Fluid Mech.* **124**, 457–473.

Perry, A. 1982 *Hot-wire anemometry*. Clarendon Press, Oxford, UK.

Pope, S. B. 2000 *Turbulent flows*. Cambridge University Press, Cambridge, UK.

Prandtl, L. 1925 Bericht fiber untersuchungen zur ausgebildeten turbulent. (eng. trans. in "report on investigation on developed turbulence", naca-tm 1231). *Zeitschrift für angewandte Mathematik und Mechanik.* **5**.

Reynolds, O. 1883 An experimental investigation of the circumstances which determine whether the motion of water shall be direct or sinnons, and of the law of resistance in parallel channels. *Proc. R. Soc.* **35**, 84–99.

Reynolds, O. 1895 On the dynamical theory of incompressible viscous fluids and the determination of the criterion. *Phil. Trans. R. Soc. A* **186**, 123–164.

Richardson, L. F. 1922 *Weather Prediction by Numerical Process*. Cambridge University Press; (2nd edition 2007).

Richter, I. A. 1883 *The notebooks of Leonardo da Vinci*. Oxford University Press, USA [ed. 1999].

Sandborn, V. A. 1972 Resistance temperature transducers. *Metrology Press.* .

Sattarzadeh, S. S. 2011 Experimental study of complex pipe flows. Master's thesis, KTH Mechanics, Stockholm, Sweden.

Segalini, A., Cimarelli, A., J-D., R., De Angelis, E. & Talamelli, A. 2011*a*

Effect of the spatial filtering and alignment error of hot-wire probes in a wall-bounded turbulent flow. *Meas. Sci. Technol.* **22**, 105408.

Segalini, A., Örlü, R., Schlatter, P., Alfredsson, P. H., Rüedi, J.-D. & Talamelli, A. 2011*b* A method to estimate turbulence intensity and transverse taylor microscale in turbulent flows from spatially averaged hot-wire data. *Exp. Fluids* **51**, 693–700.

Smits, A. J., McKeon, B. & Marusic, I. 2011*a* High-reynolds number wall turbulence. *Annu. Rev. Fluid Mech.* **43**, 353–375.

Smits, A. J., Monty, J., Hultmark, M., Bailey, S. C. C., Hutchins, N. & Marusic, I. 2011*b* Spatial resolution correction for wall-bounded turbulence measurements. *J. Fluid Mech.* **676**, 41–53.

Taylor, G. I. 1935 Statistical theory of turbulence: Parts i-iii. *Proc. R. Soc. A* **151**, 421–464.

Taylor, G. I. 1938 The spectrum of turbulence. *Proc. R. Soc. A* **164**, 476–490.

Townsend, A. A. 1976 *The Structure of Turbulent Shear Flow*. Cambridge University Press.

Tropea, C., Yarin, A. L. & (Eds.), F. J. F. 2007 *Springer Handbook of Experimental Fluid Mechanichs*. Springer.

Tsuji, T., Nagano, Y. & Tagawa, M. 1992 Frequency response and instantaneous temperature profile of cold-wire sensors for fluid temperature fluctuation measurements. *Exp. Fluids* **13**, 171–178.

Veenman, M. P. B. 2004 Statistical anlysis of turbulent pipe flow: a numerical approach. PhD thesis, Technische Universiteit Eindhoven.

Wagner, C., Huttl, T. J. & Friedrich, R. 2001 Low-reynolds-number effects derived from direct numerical simulations of turbulent pipe flow. *Comput. Fluids* **30**, 581–590.

Welch, P. D. 1967 The use of fast fourier transform for the estimation of power spectra: A method based on time averaging over short, modified periodograms. *IEEE T. Audio Electroacoust.* **AU-15**, 70–73.

Willmarth, W. W. & Sharma, L. K. 1984 Study of turbulent structures with hot wires smaller than the viscous length. *J. Fluid Mech.* **142**, 121–149.

Wilson, H. A. 1904 On convection of heat. *Proc. Cambridge Philos. Soc.* **12**, 406–423.

Wu, X. & Moin, P. 2008 A direct numerical simulation study on the mean velocity characteristics in turbulent pipe flow. *J. Fluid Mech.* **608**, 81–112.

Zanoun, E.-S., Durst, F. & Shi, J.-M. 2009 The physics of heat transfer from hot wires in the proximity of walls of different materials. *Int. J. Heat Mass Tran.* **52**, 3693–3705.